NEW SYSTEM ARCHITECTURE FOR NEXT-GENERATION WIDEBAND ULTRA-RELIABLE LOW-LATENCY COMMUNICATIONS AND NETWORKS

A Dissertation
Presented to
The Academic Faculty

by

Min-Yu Huang

In Partial Fulfillment
of the Requirements for the Degree
Doctor of Philosophy in the
School of Electrical and Computer Engineering

Georgia Institute of Technology
December 2019

NEW SYSTEM ARCHITECTURE FOR NEXT-GENERATION WIDEBAND ULTRA-RELIABLE LOW-LATENCY COMMUNICATIONS AND NETWORKS

Approved by:

Dr. Hua Wang, Advisor
School of Electrical and Computer Engineering
Georgia Institute of Technology

Dr. John Cressler
School of Electrical and Computer Engineering
Georgia Institute of Technology

Dr. Madhavan Swaminathan
School of Electrical and Computer Engineering
Georgia Institute of Technology

Dr. Vigor Yang
School of Aerospace Engineering
Georgia Institute of Technology

Dr. Gee-Kung Chang
School of Electrical and Computer Engineering
Georgia Institute of Technology

Date Approved: September 17, 2019

To My Family

ACKNOWLEDGEMENTS

I vividly remember my first day at Georgia Tech as if it just were yesterday and cannot imagine that time flies so fast. During the past five years, I am extremely grateful that Georgia Tech provided me an enjoyable, creative, and highly engaging environment to become a self-driven research scientist and enthusiastic team leader. With the generous support and insightful guidance from the Georgia Tech community, I was able to accomplish a fulfilling PhD career and make many achievements to advance the Millimeter-Wave field.

First and foremost, I am extremely fortunate to have Prof. Hua Wang as my doctoral thesis advisor and I would like to express sincere gratitude to him. Through his many stimulus discussions, he inspires me to explore important knowledge, which enables me to become a creative, passionate, and independent scientist for thesis research. Of his many words of wisdom, one that will always stick to me is when he told me to "be a wise person instead of only be a smart person", which encouraged me to take everything into careful considerations and focus on the "big picture". At the initial stage of my Ph.D., he provided a plethora of technical resources while giving me significant freedom to build my own original research direction and theme. "Never try, never know" is his favorite catch phrase to always remind me to be flexible in my research yet cautious on proving ideas with solid theory derivations and experimental verifications.

Besides my advisor, I would like to thank the rest of my thesis committees: Dr. Swaminathan Madhavan, Dr. Gee-Kung Chang, Prof. John Cressler, and Prof. Vigor Yang. I am thankful for being involved in several collaborative projects with Prof. Madhavan on

ultra-compact concurrent multi-directional beamforming receiving network for high-efficiency wireless power transfer. I also want to express my upmost gratitude towards Prof. Chang for our multiple next-generation fiber-wireless communication network discussions and projects, which expanded my vision and helped me explore different disciplines. Finally, I want to thank Prof. Cressler and Prof. Yang to serve as my thesis committee members for their valuable feedbacks, guidance, and comments.

In addition to my wonderful advisor and committee members, I am fortunate to work with many talented colleagues through the intense brain-storming discussions, countless nights working together before deadlines, and most importantly, the enlightenment and fun excitement we experienced during my Ph.D. journey. I would like to thank three Ph.D. students who have graduated from our group, Dr. Taiyun Chi, Dr. Jong Seok Park, and Dr. Song Hu, for their assistance and care for my life at the early stage of my Ph.D. study. I have been collaborating with Taiyun Chi in multiple projects and I sincerely appreciate him for his selfless knowledge sharing and helpful technical discussions. I am grateful for Jong Seok Park for his kindness with multiple assistances on both technical and nontechnical topics and thank Song Hu for his instructions and teachings. Furthermore, I would like to acknowledge my project partners Fei Wang, Tso-Wei Li, Sensen Li, Doohwan Jung, Tzu-Yuan Huang, and Amr Ahmed for their precious time, full support, and overnight tapeouts and measurements. I really enjoyed my time with them. I'm also very blessed to have multiple junior students and previous members in our group as good friends, and I want to thank, Edgar Garay, Adam Wang, Sanghoon Lee, David Munzer, Naga Sasikanth Mannem, Jeongseok Lee, Sagar Kumashi, Gregory Villiam

Junek, Christopher Snyder, and Bert Zhu for their support, and wish the best for them in the future.

I would also like to express my sincere gratitude to many other important friends at Georgia Tech, especially Meng-Hsiu Tsai, Chia-Lin Cheng, Hao-Lin Hu, Chieh-feng Cheng, Chang-Shun Liu, Lijun Zhu, May Li, Shu-han Hsu, Ying-Yuan Huang, Fu-Jen Chu, Yunyi Gong, who helped me during my Ph.D. life.

My Ph.D. research has been supported by the Defense Advanced Research Projects Agency (DARPA), Army Research Office (ARO), Georgia Tech Power Delivery for Electronic Systems (PDES) center, and Fiber-Wireless Integration and Networking (FiWIN) center and would like to express my sincerest gratitude towards them. I also want to acknowledge GlobalFoundries and IBM for fabrication donation and Keysight equipment support.

Finally, I would like to express my sincere gratitude to my family and wife for their unconditional love and support through my entire life. My parents have taught me to be a kind, reasonable, humble, and gentle person with their vision, passion, enthusiasm, and work ethic. I really appreciate them as they always support me on everything I do. As for my wife, Ms. Tsai, who have been the soul mate with me from my undergraduate, I am so fortunate to marry her at the conclusion of my Ph.D. She has always been so helpful, supportive and considerate with my life as she means the world to me. With the accompany and support from my family and wife, my Ph.D. research and dissertation became successful, enlightening, fulfilling, and most importantly enjoyable.

TABLE OF CONTENTS

LIST OF TABLES

LIST OF FIGURES

LIST OF SYMBOLS AND ABBREVIATIONS

ASF	Autonomous Spatial Filters
BF	Beamforming
CG	Conversion Gain
CPL	Coupled
CPLLs	Coupled Phased-Lock Loops
CW	Continuous-Wave
DFB	Direct Modulation Distributed Feedback
DLL	Delay-Locked-Loop
DR	Dynamic Range
DSP	Digital Signal Process
DU	Distributed Unit
FoV	Field-of-View
ILCOAs	Injection-Locked Coupled Oscillator Arrays
ILOAs	Injection-Locked Oscillator Arrays
IN	Input
IR	Image Rejection
IRR	Image Rejection Ratio
ISO	Isolation
LG	Loop Gain
LNA	Low Noise Amplifiers
LO	Local Oscillator
MIMO	Multiple-Input-Multiple-Output

Mm-Wave	Millimeter-Wave
NF	Noise Figure
NR	New Radio
OFDM	Orthogonal Frequency Division Multiplexing
PD	Phase Detector
PS	Phase Shifter
PPF	Poly-Phase Filters
RAN	Radio Access Network
RoF	Radio over Fiber
RRU	Remote Radio Units
RTS	Real-Time Oscilloscope
RX	Receiver
SNR	Signal-to-Noise Ratio
SPI	Serial-to-Parallel-Interface
SSA-BF	Self-Steering Array Beamforming
THU	Through
TX	Transmitter
UE	User Equipment
VGA	Variable Gain Amplifiers

SUMMARY

Millimeter-Wave (mm-Wave) links serve as the enabling technology for a plethora of commercial and defense applications for next-generation (5G/6G beyond) networks. To support future mm-Wave wireless systems, the next-generation system necessitates extreme mobile broadband data throughput, energy-efficient massive machine-type communication, and ultra-reliable low-latency network. My research focuses on innovative system architectures that combine mathematical, physical and IC engineering approaches to overcome many inherent challenges for future communications and achieve state-of-the-art performance for emerging wideband and low-latency applications. The proposed research is conducted in multiple disciplines, i.e., solid-state circuit, microwave theory and technique, and optical communication. They will potentially revolutionize next-generation mm-Wave communication, sensing, and optical-fiber wireless network for 5G, as well as future 6G beyond. The autonomous beamforming and low-latency aspects of my work will be also an enabling technology for the 'Tactile Internet' that can remotely access, perceive, manipulate, or control real or virtual objects in real time. In this thesis summary, several system solutions are proposed to address multiple major challenges in the next-generation communication.

First, phased-array architectures are extensively employed in communication and radar systems; however, if any beam misalignment exists, the receiver SNR improvement and the link performance will be degraded substantially. This is particularly problematic for large-scaled arrays with narrow beam-widths. Moreover, aligning array beams by digital back-ends often causes a substantial delay in the system response time. Therefore,

accurate, agile, and autonomous beamforming at the RF front-end become essential for high-performance phased arrays. An all-passive negative feedback network is proposed for a broadband and wide Field-of-View (FoV) self-steering beamforming (BF) with zero DC power consumption. Unlike existing active self-steering BFs, the all-passive nature of the proposed design ensures its zero DC operation power, which is critical for large-scaled and/or energy-constrained phased-arrays. It is the world-first system to demonstrate the autonomous signal operation on sensing, tracking, and beamforming over full FoV coverage without any external controls and consuming any DC power.

Secondly, to support future wireless communication systems (5G new radio), such as orthogonal frequency division multiplexing (OFDM) using radio over fiber (RoF) technique in radio access network (RAN) is adopted and standardized because its manageable signal processing resources simplifies the remote radio units (RRU) architecture and enable flexible software defined RF operations. Meanwhile, future communication network requires smart RRUs to substantially locate and sense signals with reliable fast switching and response time. We proposed self-steering array beamforming (SSA-BF) achieving the state-of-the-art autonomous beamforming for 6Gb/s 64-QAM signal over 50-cm wireless distance with a substantial array factor improvement and no any external tuning controls, which is the first high-speed switching SSA-BF receiver in a fiber-wireless integrated radio access for mm-Wave mobile fronthaul applications.

Thirdly, mm-Wave massive MIMOs leverage large array size to enhance the link budget and spatial selectivity. However, transmitter-receiver (TX-RX) alignment becomes difficult due to their resulting narrow beamwidth. Unlike most existing “static” applications (e.g., mm-Wave HDTV transmission), many future mm-Wave links will

operate in highly “dynamic” environments, such as wireless AR/VR and vehicle-/drone-/machine-based links, necessitating rapid and precise beam-forming/-tracking for high link reliability and low latency. We demonstrate an 8-element MIMO receiver array that is the first of its kind to support hybrid beamforming: autonomous mm-Wave/RF front-end beamforming + digital baseband beamforming. This is the first mm-wave MIMO receiver array that achieves autonomous and dynamic rejection of unknown blockers and beamforming on unknown desired signals. “Unknown blockers” or “unknown desired signals” mean that their carrier frequency (as long as in-band), angle-of-arrival (AoA), and modulation scheme are not known a priori.

Next, to preserve full field-of-view (FoV) and multi-beam/MIMO operations, digital arrays often skip FoV-limited front-end beamforming and rely on digital backends for spatial filtering. However, the RXs and ADCs need high dynamic range (DR) to handle all the aperture information and avoid array saturation by strong signals/blockers that may hinder digital beamforming. Therefore, to aid digital arrays and reduce RX/ADC DR, there is a critical need for agile spectral-spatial front-end filtering for instinctual blocker suppression and “power-equalizing” of desired signals. We present a wideband 27-41GHz RX array for N-input-N-output MIMO systems. It employs scalable cascadable array-based high-order Autonomous Spatial Filters (ASFs) with high spatial selectivity as a “smart” spatial filter bank for instinctual multi-blocker/signal management to assist digital BF. It is the first demonstration of N-input-N-output MIMO RX array with autonomous and instinctual full-FoV multi-blocker rejection/-signal BF management.

Finally, 5G MIMO systems are expected to concurrently handle multiple modulated signals (64-/256-QAM) at Giga-bits/s, which necessitates wideband >30dB SNR to

demodulate multiple signals simultaneously and demands instantaneously wideband image rejection ratio (IRR). Additionally, for concurrent signal receiving, intermodulation distortions are significant, and thus high-linearity tunable-gain RX is highly desired to avoid decorrelations among the array elements during beamforming. The last part of this dissertation presents the first CMOS receiver frontend that covers 24.5-43.5GHz mm-Wave 5G bands and supports instantaneous full-band image rejection, rejecting wideband images and receiving desired signals of multi-Gb/s 64-/256-QAM with no calibration, switching/tuning elements, or external controls, enabling future wideband low-latency 5G MIMOs.

CHAPTER 1. INTRODUCTION

The best way to get people to think outside the box is not to create the box in the first place.

– Martin Cooper

Mm-Wave is the key enabler for future imaging, sensing, and next-generation (5G/6G beyond) high-speed communications/networks. Due to the large signal loss, beamforming, a signal processing technique for directional signal transmission or reception, is required to employ future mm-Wave links and extensively employed in multiple modern commercial and defense applications. For an N-element uniform transceiver array, if the beam is perfectly aligned with the receiving/transmitting wave, the signal-to-noise ratio (SNR) of the transceiver array is improved by 10logN. To support mm-Wave wireless systems, massive multiple-input-multiple-output (MIMO)/ phased array transceiver leverages large array size to substantially enhance the mm-Wave link budget and sharpened spatial selectivity, but their resulting narrow beamwidth drastically complicates the transmitter-receiver (TX-RX) alignment. For example, the half-power beamwidth of a 1-element $\lambda/2$ dipole decreases drastically from 78˚ to 2˚ if it forms a 10-element $\lambda/2$ dipole array. Therefore, precise and accurate signal alignment is necessitated for the future versatile mm-Wave applications. Moreover, rapidly growing deployment of mm-wave links in commercial (e.g., 5G/automotive) and defense (e.g., fast-moving drones) applications often exposes the transceiver frontends in complex EM environments with multiple fast-changing yet unknown blockers (Angle-of-Arrival AoA/frequency/modulation). To preserve full field-of-view (FoV) and multi-beam/MIMO operations, digital arrays often skip FoV-limited front-end beamforming and rely on digital

backends for spatial filtering. However, the RXs and ADCs need high dynamic range (DR) to handle all the aperture information and avoid array saturation by strong signals/blockers that may hinder digital beamforming. Therefore, to aid digital arrays and reduce RX/ADC DR, there is a critical need for agile spectral-spatial front-end filtering for instinctual blocker suppression and "power-equalizing" of desired signals. Wideband high-capacity wireless access nodes are also essential for next-generation networks. For example, future 5G user equipment (UE) favors multi-band operation (especially at 24.5/28/37/39/43 GHz) to support multi-standard communication and international roaming. However, a large fractional bandwidth (BW) (>50%) poses challenges for frontend hardware, and image jamming often becomes a major issue in extreme spectral planning.

During my past five-year Ph.D. study at Georgia Tech GEMS Lab, the major research theme of my Ph.D. consists of new system/network architectures and innovative circuit techniques to achieve state-of-the-art performance for various emerging wideband, energy-efficient, and ultra-reliable low-latency applications at mm-Wave. They are especially focusing on dynamic beam-steering and tracking for unknown desired signals, rapid spatial notching for multiple unknown blockers, full-field of view (FoV) coverage, broadband operation, extreme data rates, instantaneous wideband image rejection, and rapid response time – simultaneously. Several important contributions of this Ph.D. thesis are highlighted below.

1. A nonlinear feedback loop for the proposed self-steering BF is achieved via processing the signals in two different domains, i.e., the phase and voltage domains. The nonlinear conversions between the two domains are fully exploited in our design to provide a large loop gain over full FoV, although the entire loop

is fully passive with zero DC power consumption. To the best of our knowledge, this is the first demonstration of an all-passive network for front-end self-steering BF with zero DC power, supporting large scaled energy-efficient phased arrays.

2. Based on the proposed zero-DC self-steering BF, we combined with our proposed broadband wide-FoV mm-Wave antenna arrays and optical fiber link to achieve the first demonstration of a high-speed switching SSA-BF receiver in a fiber-wireless integrated radio access. The SSA-BF for mm-Wave fiber-wireless network supports 10 Gb/s carrier aggregation of 20 x100-MHz OFDM signals and demonstrates the state-of-the-art full-FoV autonomous beamforming for 6Gb/s 64-QAM signal over 50-cm wireless distance, enabling dynamic 5G mobile fronthaul applications.
3. We present an 8-element mm-Wave scalable full-FoV MIMO RX array with hybrid BF by using closed-loop multi-stage cascadable DSP-free mm-wave/RF BFs and digital BF. The closed-loop beamformers autonomously create spatial notches on multiple in-band blockers and perform BF on the desired signals with world-record <1μs dynamic response time, enabling future next-generation (5G/6G beyond) ultra-low latency communication even under complex/ congested EM environment. The array is the world-first MIMO to successfully rejects wideband in-band blocker and receives desired signal with 6Gb/s 64QAM and 1.6Gb/s 256QAM over full FoV with autonomous operations.
4. A wideband mm-Wave N-input-N-output MIMO systems is proposed to support future high-capacity spatial multi-stream receiving. Unlike any existing design, it is the first demonstration of N-input-N-output MIMO RX array with

autonomous and instinctual full-FoV multi-blocker/signal management. The array autonomously rejects multiple wideband modulated in-band blockers and receives desired signal with multi-Gb/s 64/256QAM over full FoV.

5. We demonstrate a mm-Wave compact RX frontend achieving full-frequency instantaneously wideband image rejection. After image rejection, the wideband desired RX signal is successfully demodulated with 12Gb/s 64-QAM and 8Gb/s 256-QAM under 10dB larger wideband modulated image signal with the same modulation scheme and data rate. This is the first demonstration RF frontend to support instantaneously wideband GHz image rejection with no calibration, switching/tuning elements, or external controls, enabling instantaneously wideband low-latency 5G MIMOs in complex EM environments.

The remainder of this dissertation is organized as follows.

Chapter 2 introduces an all-passive negative feedback network to perform autonomous RF front-end BF towards the direction of the incident RF beam. The beam-forming front-end block consists of a passive network for RF signal processing, voltage rectifiers, and voltage-controlled phase shifters, all of which are passive components and consume zero DC power. The measurements demonstrate that a high-quality 4-element array factor is successfully synthesized for the input progressive phase shift from -180° to +180 in the closed-loop operation, out-performing reported active self-steering beam-formers. To the best of our knowledge, this is the first demonstration of an all-passive network for front-end self-steering BF with zero DC power.

Chapter 3 shows a broadband scalable full-FoV self-steering array beamformer (SSA-BF) mm-Wave fiber-wireless integrated network over 25 km fiber link. A home-designed antenna array is designed to achieve a state-of-the-art mm-Wave antenna with a wide broadside 3-dB beamwidth= ± 80° and broadband 17-36GHz for the proposed SSA-BF receiver for a 5G fiber-wireless access. The SSA-BF achieves calibration- and digital signal process (DSP)-free beamforming with passive delay-locked-loop (DLL) phase domain negative feedback loops to operate wideband modulation. Without any prior information (angle-of-arrival AoA), a proof-of-concept mm-Wave fiber-wireless SSA-BF demonstrates that it can rapidly yet accurately align the desired signals with low-latency < 3ms beam-tracking and exhibits long-term system stability. The SSA-BF achieves the state-of-the-art autonomous BF for enhanced mobile data-rate up to 10 Gb/s and 7.8 Gb/s with 20x100MHz carrier aggregation OFDM in back-to-back and over 25-km fiber transmission over full-FoV.

Chapter 4 presents a hybrid beam-forming MIMO receiver array including an on-chip 2-stage closed-loop mm-wave/RF front-end beamformers and off-chip baseband digital BF. The 2-stage closed-loop mm-wave/RF front-end beam-formers alone support a variety of operation modes: (mode-I) autonomous beam-forming/tracking for an unknown in-band desired signal, (mode-II) autonomous rejection of one unknown in-band/co-channel blocker + autonomous beam-forming/tracking for an unknown in-band desired signal, (mode III-A) autonomous rejection of one unknown in-band/co-channel blocker with one deep spatial notch (54dB rejection), and (mode III-B) autonomous rejection of two unknown in-band/co-channel blockers with two notches (30~40dB rejection). The closed-loop DSP-free mm-wave/RF frontend beamformer achieves rapid response time of

<1μs per beam-former stage, which enables rapid beam-forming/-tracking in dynamic environment or low-latency MIMO applications and is 100× ~ 1000× faster than the state-of-the-art mm-wave/analog/digital beamformers using baseband DSP signal processing for beam-finding/-locating.

Chapter 5 reports a MIMO RX with N-Input-N-Output using scalable cascadable autonomous array-based high-order spatial filters for instinctual full-FoV multi-blocker/signal Management. The RX is designed with cascaded 3-stage ASFs for different receiving cases. It shows a state-of-the-art maximum 62dB cancellation for autonomous multi-blocker suppression over full FoV. This is the first RX which can autonomously support N wideband modulated blocker suppression and desired signal beamforming simultaneously without any digital beamforming aid and the autonomous array-based high-order spatial filters provide sharpened spatial selectivity, enabling multi-beam high-capacity massive MIMO. The N-input-N-output MIMO RX array covers an extremely broadband frequency range (27-41GHz) and the entire spatial range (full-FoV) to address various unmet challenges in low-latency MIMO systems.

In Chapter 6, the first mm-wave extreme wideband 5G RX frontend (24-43GHz) is demonstrated for supporting a state-of-the-art 12Gb/s 64-QAM and 8Gb/s 256-QAM wideband image rejection even when the image signal is 10dB larger than the desired signal and they are exactly overlapped after down-conversion. The RX 3-dB bandwidth is from 24.5 to 43.5GHz, which can cover major mm-Wave 5G bands at 24.5/28/37/39/43 GHz and support multi-standard communication and international roaming. The transformer-based IQ network for broadband image rejecting is able to accommodate large load impedance transformation (500Ω) with robust I/Q generation, which provides impedance

up-scaling and passive voltage amplification to boost the LO swing. It achieves a low-loss mm-Wave I/Q LO generation with a compact size ($0.14mm^2$) and state-of-the-art instantaneously wide bandwidth 25-50GHz.

In the end, this dissertation is summarized in Chapter 7.

CHAPTER 2. AN ALL-PASSIVE NEGATIVE FEEDBACK NETWORK FOR BROADBAND AND WIDE FIELD-OF-VIEW SELF-STEERING BF WITH ZERO DC POWER CONSUMPTION

This Chapter presents an all-passive negative feedback network that performs autonomous RF front-end beam-forming and dynamic beam-tracking towards the direction of the incident RF signal. The proposed feedback network consists of a passive RF signal processing network, voltage rectifiers, and voltage-controlled delay-line phased shifters, all of which are passive-only circuits. The negative feedback loop is realized by passive phase detection, phase-to-voltage conversion, and voltage-controlled phase shifting, achieving a large loop-gain and autonomous operation with zero DC power consumption. The nonlinear behavior of the loop is exploited to substantially expand the array Field-of-View (FoV). A proof-of-concept broadband 4-element all-passive self-steering beam-former at 5GHz with a wide FoV is implemented in a standard 130nm CMOS process. A high-quality 4-element synthesized array factor is measured for the input progressive phase shift ϕin from -180° to 180°. When the proposed negative feedback loop is enabled, the normalized array factor is -2.87dB/-2.8dB at ϕ_{in} = +90°/−90° with an input RF power Pin of -17dBm/element at 5GHz, achieving > 25dB array factor improvement over the open-loop operation. Moreover, the nonlinear feedback loop allows for significant array factor improvement even at ϕ_{in} = +180°/−180°. The proposed beamformer also achieves high-quality self-steering BF from 4GHz to 5.68GHz with 34.7% fractional bandwidth. Therefore, the proof-of-concept all-passive self-steering beam-former outperforms the state-of-the-art active designs in terms of beam-forming quality, FoV, and fractional

bandwidth. To the best of the authors' knowledge, this is the first demonstration of an all-passive negative feedback network for a broadband and wide FoV self-steering BF with zero DC power consumption.

2.1 Introduction

Phased-array receivers are extensively employed in modern communication and radar systems [1]-[3]. For an N-element uniform receiver array, if the beam is perfectly aligned with the incident wave, the signal-to-noise ratio (SNR) of the receiver array is improved by 10logN. However, any beam misalignment in practice will substantially degrade the array SNR and link performance; this is particularly problematic for large-scaled arrays due to their narrow beam-widths, e.g., in next-generation 5G links and advanced radars. Conventionally, back-end digital signal processing (DSP) is used to perform array beam forming and alignment at the expense of extra power consumption, slow response time, and system complexity [4].

Without back-end DSP or manual beam alignment, front-end self-steering beam-formers can automatically track the incident beam [5]-[7]. The self-steering beam-former can benefit numerous applications, such as energy-efficient large-scaled phased array [11], RFID [12], low power sensor network [13], and wireless energy harvesting [14][15]. A generic system of a self-steering beam-former without any external control is shown in Figure 2.1. θ is the incident angle from -90° to 90°. ϕ_{in} is the input progressive phase shift from -180° to 180° in a λ/2-spaced receiver array, given $\phi_{in} = (\pi/2)\times\sin\theta$. The self-steering beam-forming enables fast and accurate system response and reduces the overhead and complexity for generating external open-loop phase-shift controls.

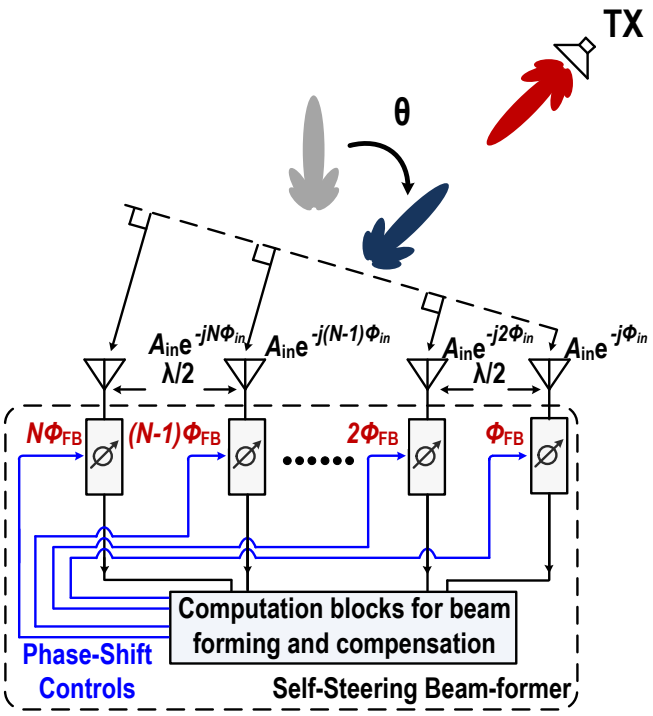

Figure 2.1 – Conceptual system schematic of a generic self-steering beam-former in a phased-array receiver system

Existing self-steering beam-formers are mostly based on active approaches and consume considerable DC power per array element [5]-[7]. For example, off-chip active phase detectors and active phased shifters are used in [5] to track and compensate the beam alignment with a total DC power of 430mW. In [6], active power detector and microcontrollers consume a DC power of around 560mW. Injection-locked oscillator arrays (ILOAs) [8][9] and injection-locked coupled oscillator arrays (ILCOAs) [10] are utilized to autonomously correct the beam misalignment. However, external injection signals and manual alignment are often needed to adjust the beam angle [8]-[10]. Moreover, these oscillator-based systems is often narrowband due to the injection locking nature [8]-[10]. Recently, coupled oscillator arrays (COAs) and coupled phased-lock loops (CPLLs) are used for automatic beam-forming and tracking [7]. Besides substantial DC power consumption and narrow-band operation, these architectures exhibit direct

degradation of system stability and FoV for large number of array elements, limiting their use in large-scaled array [7]. Therefore, there is an unmet need for accurate, autonomous and dynamic beam-forming architecture that can operate at the RF front-end and support low-power large-scaled phased-arrays.

To address these challenges, this Chapter proposes an all-passive self-steering beam-former using a passive network with negative feedback for automatic, broadband and wide-FoV beam-forming at the RF front-end [16]. Unlike existing active self-steering beam-formers, the all-passive nature of the proposed design ensures its zero DC operation power, which is critical for large-scaled and/or energy-constrained phased-arrays. In addition, compared with energy harvesting based systems [17]-[19], the proposed system does not require any energy storage/charging, and it responds instantaneously to the input RF beam and operates continuously without any duty cycle operation. Thus, the receiver can capture the incoming information with no down-time, and there is no need for energy storage element. Moreover, unlike the active approaches, e.g., COAs [7], the all-passive approach ensures no signal re-emission by the beamformer. This electromagnetically "quiet" nature is particularly useful for many military and high-security applications.

As a proof-of-concept demonstration, a broadband and wide FoV 4-element all-passive self-steering beam-former is implemented in a standard 130nm CMOS process. A high-performance array operation is achieved for the input progressive phase shift ϕ_{in} between -180° and +180° and over an operating frequency range from 4GHz to 5.68GHz. At P_{in} = -17dBm/element, the closed-loop normalized array factor at 5GHz is measured as -2.87dB/-2.8dB at ϕ_{in} of +90°/-90°, i.e., the array null point without self-steering operation, showing >25dB array factor improvement over the open-loop operation. The proposed all-

passive self-steering beam-former out-performs all the reported active designs for the operation bandwidth, FoV, and beam-forming quality.

This Chapter is organized as follows. Section 2.2 presents the system architecture and operation principle of the all-passive negative feedback network for self-steering BF. The details of a 5GHz 4-element beam-former prototype are discussed in Section 2.3. Section 2.4 shows the measurements and a performance comparison with reported active self-steering beam-formers.

2.2 An All-Passive Network with Negative Feedback for Self-Steering BF

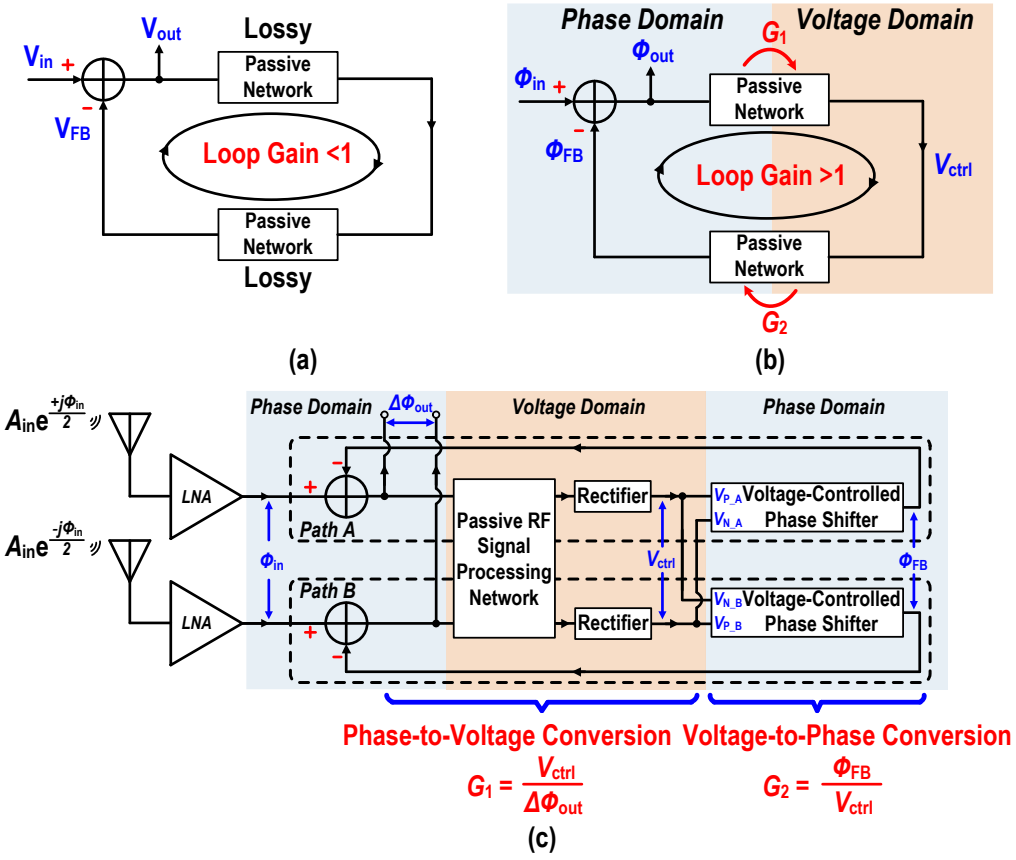

Figure 2.2 – (a) Conceptual block diagram of an all-passive negative feedback network operating in only one signal domain. (b) Conceptual block diagram of an all-passive negative feedback network operating in phase domain and voltage domain. (c) The simplified schematic of the all-passive negative feedback network for self-steering BF, shown in the phase and voltage signal domains.

A self-steering beam-former should respond autonomously and accurately to the input beam without any external control signal, which therefore requires some negative feedback mechanism in the beam-forming operation. Two conceptual diagrams that connect passive networks and form negative feedback configurations are shown in Figure 2.2a and 2.2b. Passive networks in practice only exhibit signal loss and cannot provide any power gain due to the conservation of energy. Therefore, if two passive networks are connected in a negative feedback loop and process signals in the same signal domain, e.g., RF power, the overall loop gain is always less than one, which is incapable of producing a desired compensation signal to track the input and reduce the error signal (Figure 2.2a). However, in the context of beam-forming/-tracking, the progressive and relative phase among the array elements is actually the signal-of-interest, and such phase information is not directly related with the energy of the RF signals being processed in the array. Moreover, if the forward and feedback passive networks can convert the signals between two signal domains, e.g., phase and voltage, the overall loop gain of such an all-passive negative-feedback networks can be potentially greater than one due to the inter-domain signal conversions (Figure 2.2b). This concept can be intuitively understood. For example, one can employ multiple voltage-controlled phase-shifters in cascade to process the received RF signal, and a small control voltage change can generate a large total phase-shift, i.e., achieving a large voltage-to-phase conversion gain, without any external power supply. The proposed all-passive negative feedback network for self-steering beam-forming follows this architecture concept (Figure 2.2c). It first detects the phase difference of the incident signal between two array elements by a passive phase detector, yielding a differential phase-dependent voltage output. To complete the negative feedback loop, this

voltage signal is then converted back to the phase domain as a differential compensation phase signal by voltage-controlled phase-shifters. Note that the passive detectors and the voltage-controlled phase-shifters are nonreciprocal networks used to facilitate the proposed negative feedback. The detailed operation principle is explained as follows.

Assume ϕ_{in} is the progressive phase shift of the RF inputs between two adjacent elements (path A and path B in Figure 2.2c). The negative feedback loop generates the phase compensation signal ϕ_{FB} to minimize the residual output phase difference $\Delta\phi_{out}$ and achieve automatic beam alignment of the path A and path B. First, the path A/path B residual phase difference $\Delta\phi$out is transformed to a differential DC voltage V_{ctrl} by a passive RF signal processing network and two rectifiers, which collectively function as a passive phase detector. The large-signal phase-to-voltage conversion gain $G_1 = V_{ctrl} / \Delta\phi_{out}$ can be derived based on the specific circuit implementation. Next, by applying Vctrl on the voltage-controlled phase shifters, the feedback compensation phase ϕ_{FB} is generated with a voltage-to-phase conversion gain $G_2 = \phi_{FB} / V_{ctrl}$. The differential V_{ctrl} polarities are selected to ensure an overall negative feedback in the phase domain. Thus, the loop gain is $G1G2$, and the resulting phase error $\Delta\phi$out as the residual output phase difference is

$$\Delta\phi_{out} = \phi_{in} - \phi_{FB} = \phi_{in} / (1 + G_1G_2). \quad (2.1)$$

To autonomously and accurately align the receiver beam with the incident signal over a wide FoV, the loop gain G_1G_2 should be maximized over a broad progressive phase shift range ϕin. This is accomplished by exploiting the nonlinear conversion between the phase and voltage domain and nonlinear operation of the feedback loop, while the entire loop is kept all-passive with zero DC power consumption. Moreover, unlike [7]-[10], the

proposed all-passive self-steering beam-former does not require to know the actual frequency of the incident signals a priori; this frequency agnostic nature ensures its broadband operation and utility in practical array applications.

2.3 Circuit Implementation

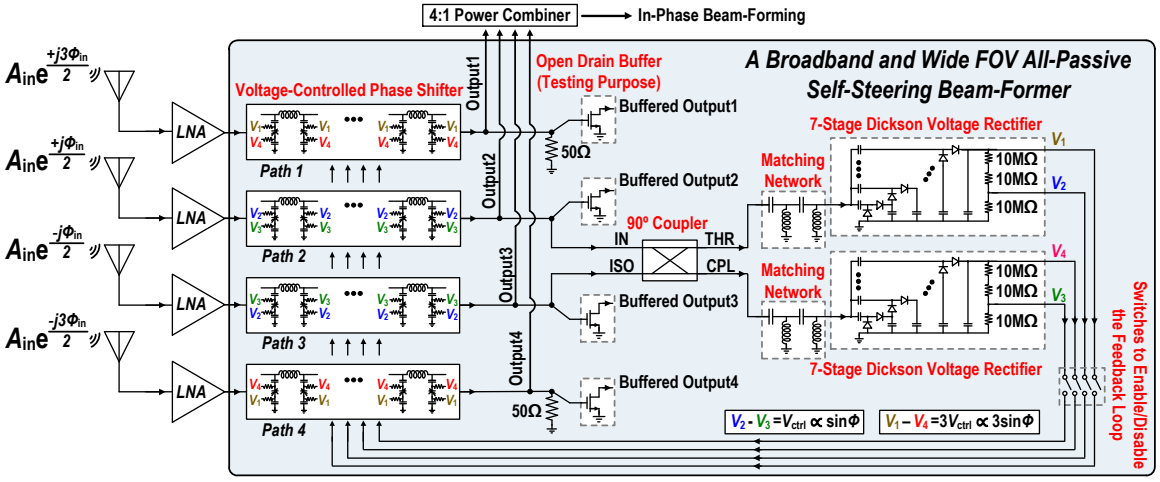

Figure 2.3 – Top-level circuit schematic of an all-passive broadband and wide FoV 4-element self-steering beam-former in a phased-array receiver. The LNAs and the 4:1 power combiner are not included in this design.

To demonstrate the proposed all-passive negative feedback network for self-steering BF, a 4-element proof-of-concept design at 5GHz is implemented [16] (Figure 2.3). The inner two signal paths (path 2 and path 3) are included in the negative feedback loop, while the outer two paths (path 1 and path 4) are controlled in an open-loop manner. This all-passive self-steering beam-former can be employed after front-end low noise amplifiers (LNAs) in an RF phased-array receiver; additional down-conversion mixers can be added before the beam-former for mm-Wave operations. Once the receiver is aligned with the incoming beam by the proposed beam-former, the four outputs can be in-phase combined for BF. Four open-drain buffers are used in this proof-of-concept design only to facilitate

the testing. Switches are added to enable or disable the feedback loop for open-loop or closed-loop measurements, respectively.

2.3.1 Passive Phase-to-Voltage Convertor Analysis

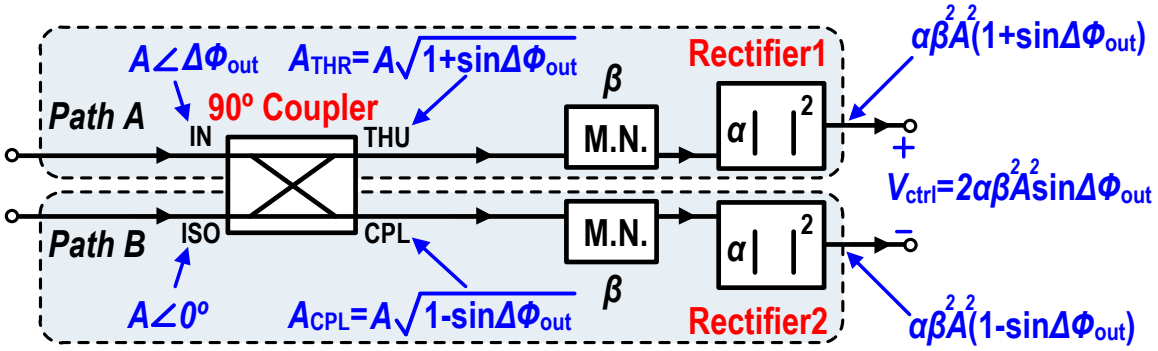

Figure 2.4 – The passive phase-to-voltage conversion circuit, i.e., a passive phase detector, using a 90° coupler, two matching networks, and two rectifiers.

The simplified passive phase-to-voltage convertor is shown in Figure 2.4. It consists of a 90° coupler as an RF signal processing network, two matching networks, and two 7-stage Dickson voltage rectifiers [20]. The 90° coupler utilizes an ultra-compact transformer-based topology [21][22] with a characteristic impedance of 50Ω. The two input signals in the path A and path B are concurrently fed to the *Input (IN)* and *Isolation (ISO)* ports of the 90° coupler. The two resulting outputs from the *Through (THU)* and *Coupled (CPL)* ports are fed to the Dickson voltage rectifiers. To maximize the driving voltage amplitude for the Dickson voltage rectifiers, 2-stage *LC* matching networks are used to down-transform the rectifier input impedance to 50Ω. The outputs of the rectifiers are then used as the differential control voltages V_{ctrl} to drive the passive voltage-controlled phase shifters to generate the compensation phase ϕ_{FB}. The large-signal behavior of the phase-to-voltage converter can be analyzed by applying two RF incident signals with the

same amplitude A but at a phase difference $\Delta\phi_{\text{out}}$ into the *IN* and *ISO* ports of the 90° coupler. The voltage amplitudes of the output RF signals at the *THR* and *CPL* ports are

$$A_{\text{THR}} = \left|\frac{A}{\sqrt{2}}(1 - je^{j\Delta\phi_{\text{out}}})\right| = A\sqrt{1 + \sin\Delta\phi_{\text{out}}}, \text{ and}$$

$$A_{\text{CPL}} = \left|\frac{A}{\sqrt{2}}(e^{j\Delta\phi_{\text{out}}} - j)\right| = A\sqrt{1 - \sin\Delta\phi_{\text{out}}}. \quad (2.2)$$

Thus, the 90° coupler transforms the phase difference of the two RF inputs to the voltage amplitude of the RF outputs, which are further converted to a differential DC voltage V_{ctrl} by the rectifiers. Assume that the matching networks increase the output RF voltage amplitude by a factor of β due to its impedance transformation, and assume that the two matched rectifiers are square-law devices with a conversion coefficient α. The DC output voltages of the two rectifiers are

$$V_{\text{out, rectifier1}} = \alpha\beta^2 {A_{\text{THR}}}^2 = \alpha\beta^2 A^2(1 + \sin\Delta\phi_{\text{out}}), \text{ and} \quad (2.3)$$

$$V_{\text{out, rectifier2}} = \alpha\beta^2 {A_{\text{CPL}}}^2 = \alpha\beta^2 A^2(1 - \sin\Delta\phi_{\text{out}}). \quad (2.4)$$

Thus, the differential feedback voltage signal V_{ctrl} is obtained as

$$V_{\text{ctrl}} = V_{\text{out, rectifier1}} - V_{\text{out, rectifier2}} = 2\alpha\beta^2 A^2 \sin\Delta\phi_{\text{out}}. \quad (2.5)$$

The large-signal open-loop phase-to-voltage conversion gain G_1 can be further calculated as

$$G_1 = V_{\text{ctrl}}/\Delta\phi_{\text{out}} = 2\alpha\beta^2 A^2 \sin\Delta\phi_{\text{out}}/\Delta\phi_{\text{out}}. \quad (2.6)$$

Figure 2.5 plots V_{ctrl} and G_1 versus the residual phase difference $\Delta\phi_{\text{out}}$, i.e., the phase difference between adjacent array elements after the self-steering compensation. G_1 is a

sinc function with its peak value at $\Delta\phi_{out} = 0°$. Its open-loop response gradually decreases to zero when $\Delta\phi_{out}$ approaches ±180°. Therefore, a positive conversion gain is maintained over the entire ±180° phase shift range.

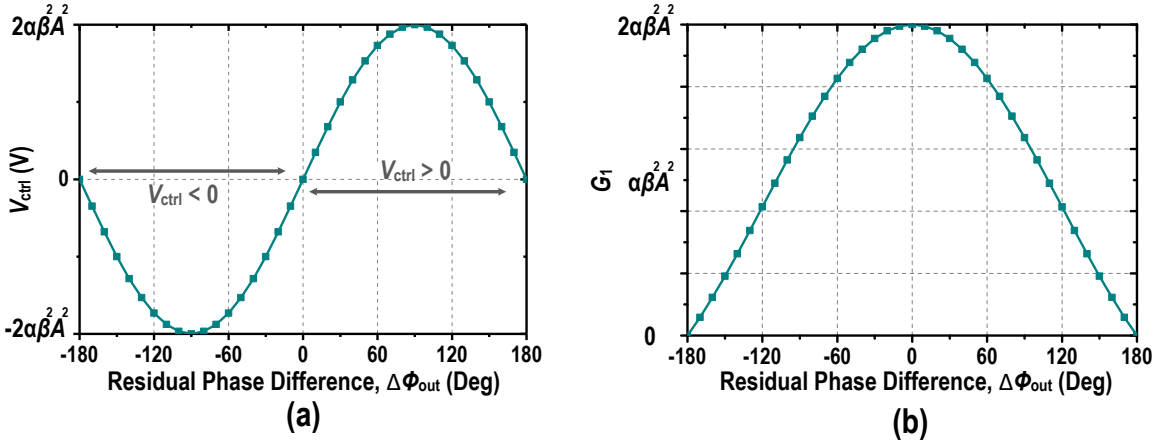

Figure 2.5 – (a) Differential feedback DC voltage V_{ctrl} versus the residual phase difference $\Delta\phi_{out}$. (b) The large-signal phase-to-voltage conversion gain G_1 versus the residual phase difference $\Delta\phi_{out}$.

To achieve a high conversion coefficient α and maximize the phase-to-voltage conversion gain G_1, 7-stage Dickson rectifiers are implemented using zero-threshold transistors (V_{th}~70mV). In addition, the matching networks scale the coupler's 50Ω outputs to high impedance values at the rectifiers' inputs, which passively amplifies the RF voltage swings at the rectifier inputs ($\beta > 1$) and further facilitates the rectification. By combining these techniques, the proposed rectification scheme can properly operate with μW-level RF inputs (-17dBm/path nominal) and provide a significant phase-to-voltage conversion gain G_1 over a wide FoV.

The proposed passive phase-to-voltage convertor serves as a wide-FoV passive phase detector. Unlike active analog multiplier based phase detector, it extracts the phase difference of two RF signal paths with no DC power consumption. Compared to comparator-based phase detectors, it operates with RF signals at a low detection sensitivity

(μW-level), which is verified by the measurements and includes circuit noise in practice. Although the phase-to-voltage conversion gain G_1 depends on the input RF amplitude, this does not affect the negative feedback operation for self-steering beam-forming, as long as the RF inputs are adequately strong to make the total loop gain G_1G_2 sufficiently larger than one. However, the loop gain gradually degrades at a lower input RF power, which sets the sensitivity limit of the beamformer. Furthermore, just like other self-steering beam-forming circuits, this beam-former should be used in conjunction with front-end blocker rejection circuits, which means that the self-steering beam-former only processes the desired signal. Therefore, the proposed system is considered to process one set of the input signals without considering the effect of blocker signals. The measured and simulated self-steering performance versus the input RF power will be presented and discussed in Section 2.4.

2.3.2 Passive Voltage-to-Phase Convertor Analysis

The passive voltage-to-phase convertor, i.e., a voltage controlled phase shifter, is implemented as a 7-stage L-C synthetic delay lines with varactors in this design (Figure 2.6a). The control voltages of the varactors V_2 and V_3 are generated from the two rectifiers. The differential voltage difference of V_2 and V_3 is V_{ctrl}. The simulated phase shift versus V_{ctrl} at 5GHz is shown in Figure 2.6b. The linear-region slope, i.e., the voltage-to-phase conversion gain, is 1.33 degree/mV at 5GHz.

The differential DC voltage V_{ctrl} are connected to the varactors in the path 2 and path 3 (inner two paths) with opposite polarities to achieve desired differential phase compensation and double the effective voltage-to-phase conversion gain (Figure 2.3). The simulated voltage-to-phase differential conversion gain G_2 is 2×1.33 degree/mV = 2.66 degree/mV at 5GHz. The averaged loss of the 7-stage L-C synthetic T-line is 8dB, which

can be compensated by the front-end LNAs. The phase shifter design can adopt wire-bonding inductors and off-chip varactors to further reduce the loss.

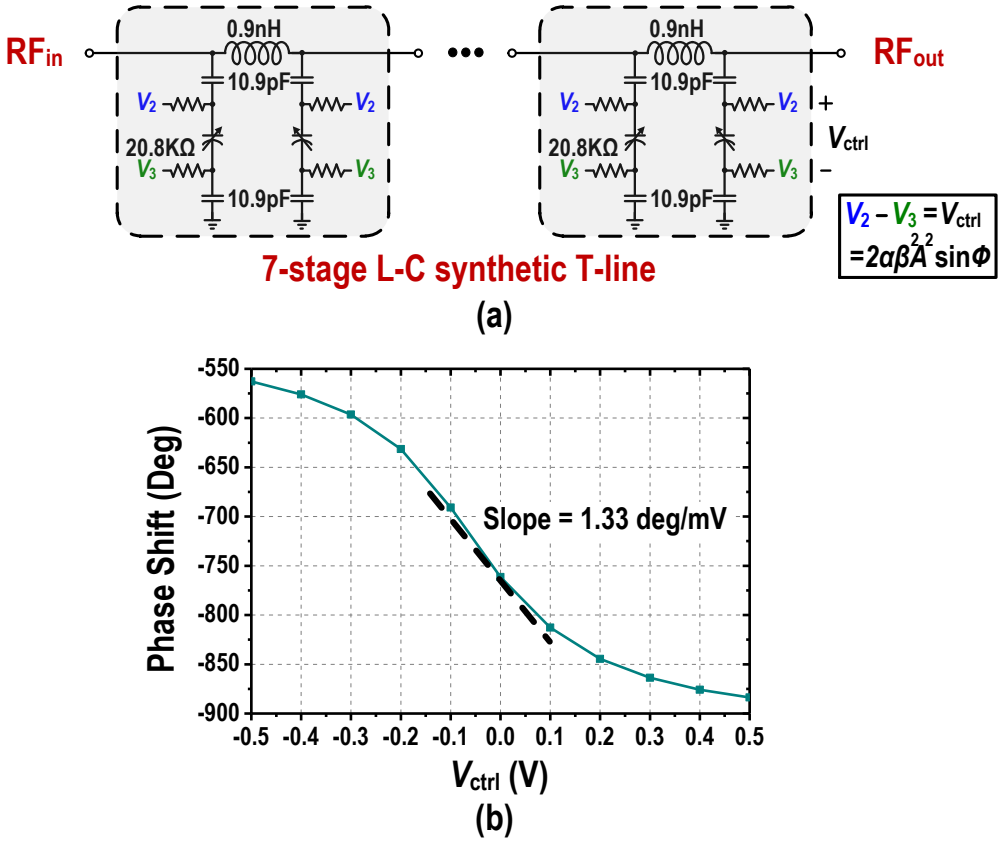

Figure 2.6 – (a) A 7-stage L-C synthetic delay line with varactors as the voltage controlled phase shifter. (b) The simulated phase shift versus differential control voltage V_{ctrl}.

2.3.3 Open-Loop Controls of the Outer Paths

In a uniform array, the input progressive phase shift of the path 1 and path 4 (outer two paths) is three times of the path 2 and path 3 (inner two paths) (Figure 2.7). Thus, the path 1 and path 4 require $3\phi_{FB}$ for phase compensation. If the same voltage-controlled phase shifters are used in path 1 and path 4, they require a control voltage of $3V_{ctrl}$, while V_{ctrl} is for the path 2 and path 3, assuming the phase shifters are in their linear regimes. A fully passive approach to generate $3V_{ctrl}$ for the path 1 (and 4) can be achieved by using

resistive loads with a 3:1 dividing ratio at the two rectifier outputs (Figure 2.8). If V_{ctrl} is generated and regulated to the appropriate value by the negative feedback loop in path 2 and path 3, a control voltage of $3V_{ctrl}$ will be automatically generated by the resistive divider and can be used to control the path 1 and path 4 (V_1 and V_4) in an open-loop manner.

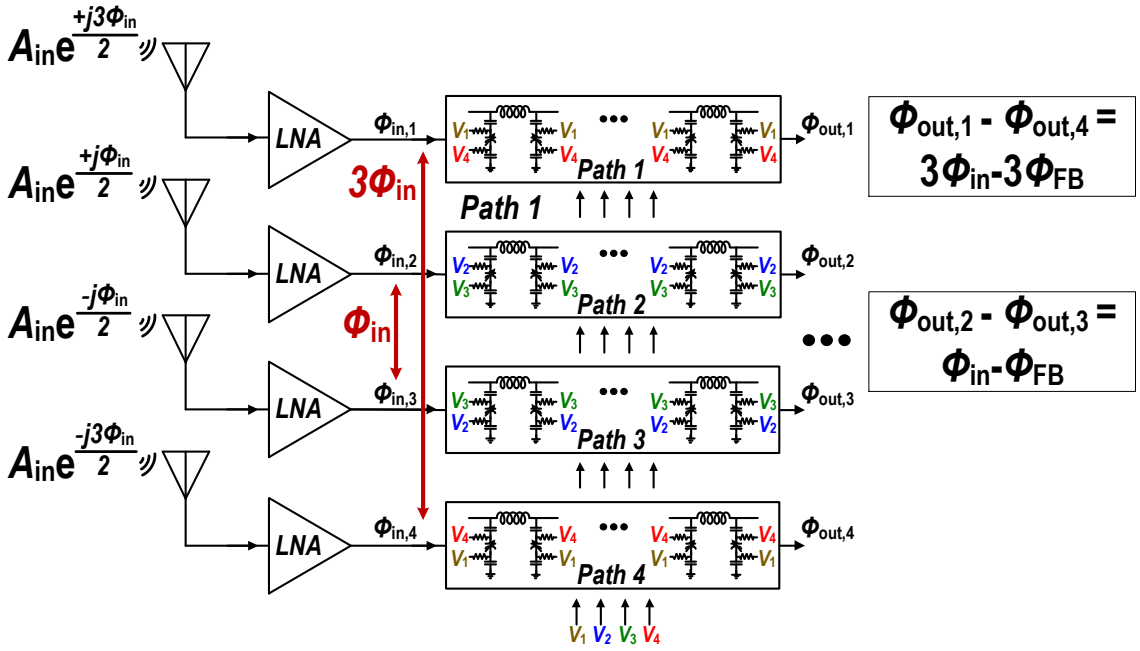

Figure 2.7 – The input progressive phase shift of the path 1 and path 4 (outer two paths) is three times larger than that of the path 2 and path 3 (inner two paths). Thus, the path 1 and path 4 require $3\phi_{FB}$ for phase compensation and thus $3V_{ctrl}$ as the control voltage.

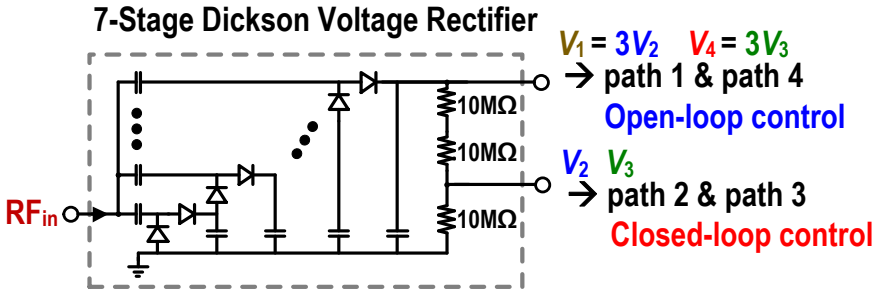

Figure 2.8 – A 7-stage Dickson voltage rectifier using a 3:1 resistor divider load to generate V_{ctrl} for the path 2 (and 3) and $3V_{ctrl}$ for the path 1 (and 4). V_2 and V_3 represent the voltages generated by the rectifiers with $V_{ctrl} = V_2$-V_3 (Figure 2.3). V_1 and V_4 are their 3× replica voltages with $3V_{ctrl} = V_1$-V_4.

2.3.4 *Closed-Loop Analysis of the Nonlinear Negative Feedback Network*

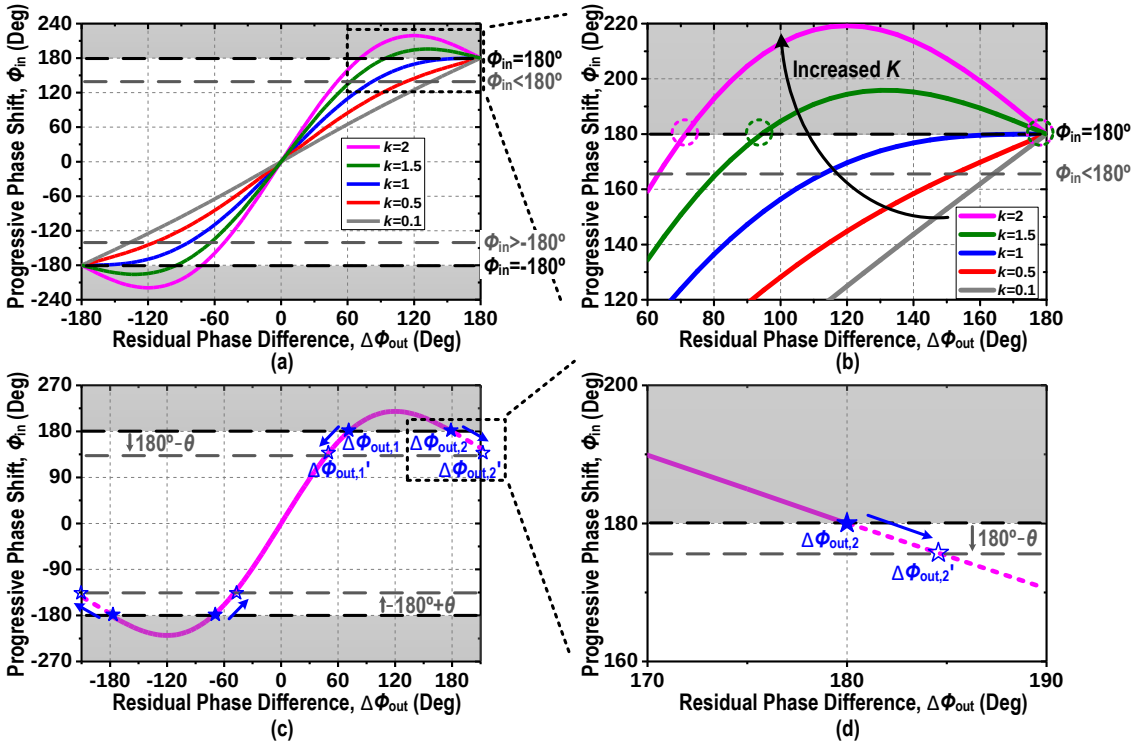

Figure 2.9 – (a) Progressive phase shift ϕ_{in} versus the residual phase difference $\Delta\phi_{out}$ at different k. (b) A zoom-in view of Figure 2.9a from the residual phase difference $\Delta\phi_{out}$ = 60° to 180°. (c) Perturbation analysis of the two possible solutions $\Delta\phi_{out,1}$ and $\Delta\phi_{out,2}$ at ϕ_{in} = ±180° for k = 2. (d) A zoom-in view of Fig. 9c around $\Delta\phi_{out}$ = 180° at k = 2, showing the unstable solution $\Delta\phi_{out,2}$.

The large-signal closed-loop performance and the normalized array factor of the 4-element beam-former is next analyzed. First, the residual output phase error $\Delta\phi_{out}$ can be expressed as

$$\Delta\phi_{out} = \phi_{in}/(1+G_1G_2) = \phi_{in}/[1+(2\alpha\beta^2A^2\sin\Delta\phi_{out}/\Delta\phi_{out})G_2]. \quad (2.7)$$

Note that G_1 is not a fixed value, and it varies with $\Delta\phi_{out}$, i.e., the residual error phase after the compensation. Thus, the negative feedback loop is a nonlinear loop, and (2.7) can be simplified as

$$\Delta\phi_{out} + k \sin \Delta\phi_{out} = \phi_{in}, \quad (8)$$

where $k = 2\alpha\beta^2 A^2 G_2$, which is the loop gain at $\phi_{in}=0^o$ when a boresight signal is received.

Since k is in a quadratic relationship with the input RF amplitude, this again indicates the loop response is a function of the input power. To examine this input-power-dependency and the nonlinear loop behavior, the solutions of $\Delta\phi_{out}$ in the transcendental equation (8) for a given ϕ_{in} are first analyzed. Figure 2.9a shows the input progressive phase shift ϕ_{in} computed using (8) versus the residual output phase $\Delta\phi_{out}$ at different k. In a λ/2-spaced phased array, ϕ_{in} is confined within ±180°, and $\Delta\phi_{out}$ is also within ±180° by the negative feedback operation. For - 180° < ϕ_{in} < 180°, $\Delta\phi_{out}$ has only one corresponding solution for each ϕ_{in} in (8) at any k values (Figure 2.9a and Figure 2.9b). For ϕ_{in} = ±180°, i.e., when an end-fire signal is received, (8) always has a trivial solution at $\Delta\phi_{out}$ = ±180° regardless of k, showing that the negative feedback loop gain is zero and the self-steering is not in operation. However, if k >1, equation (8) has one more non-trivial solution at $|\Delta\phi_{out}|$<180°, highlighted in Figure 2.9b; based on Figure 2.5b, this solution of $|\Delta\phi_{out}|$<180° means that the negative feedback loop gain is non-zero and the self-steering beam-forming is still in effect even for this end-fire signal incidence. This is because the value of $\Delta\phi_{out}$ + k sin $\Delta\phi_{out}$ goes beyond ±180° when k >1 and then falls back to ±180° at $\Delta\phi_{out}$ = ±180°. On the other hand, if $k \leq 1$, $\Delta\phi_{out}$ + k sin $\Delta\phi_{out}$ never exceeds ±180°, and there is only one solution of $\Delta\phi_{out}$ = ±180° for ϕ_{in} = ±180°, respectively.

A perturbation analysis is performed to analyze the stability of the two possible solutions $\Delta\phi_{out}$ for ϕ_{in} = ±180° when k > 1 (Figure 2.9c). For ϕ_{in} = 180°, assume a small perturbation θ (θ > 0) is applied on ϕ_{in}, i.e., ϕ_{in} = 180°−θ. The two possible solutions $\Delta\phi_{out,1}$ and $\Delta\phi_{out,2}$ are shown in Figure 2.9c for the case of k = 2. After the perturbation (ϕ_{in}

= 180°−θ), $\Delta\phi_{out,1}$ becomes smaller and moves to $\Delta\phi_{out,1}$'. Thus, this $\Delta\phi_{out,1}$ is a stable solution, since $\Delta\phi_{out}$ should be smaller than 180° when ϕ_{in} < 180° due to the negative feedback. However, the other solution $\Delta\phi_{out,2}$ = 180° moves to a larger $\Delta\phi_{out,2}$' that exceeds 180° when ϕ_{in} < 180° (Figure 2.9d); this $\Delta\phi_{out,2}$ is not a stable solution and conflicts with the negative feedback operation. This perturbation analysis can also be applied for ϕ_{in}= −180°, indicating $\Delta\phi_{out}$ = −180° is not a stable solution for k > 1. Therefore, when k > 1, there is only one stable solution $|\Delta\phi_{out}|$ < 180° for $|\phi_{in}|$ = 180°. This stable solution can be solved numerically based on (8) or graphically using Figure 2.9a. However, for $k \leq 1$, $\Delta\phi_{out}$ = ±180° is the only solution and also the stable solution for ϕ_{in}= ±180°, respectively.

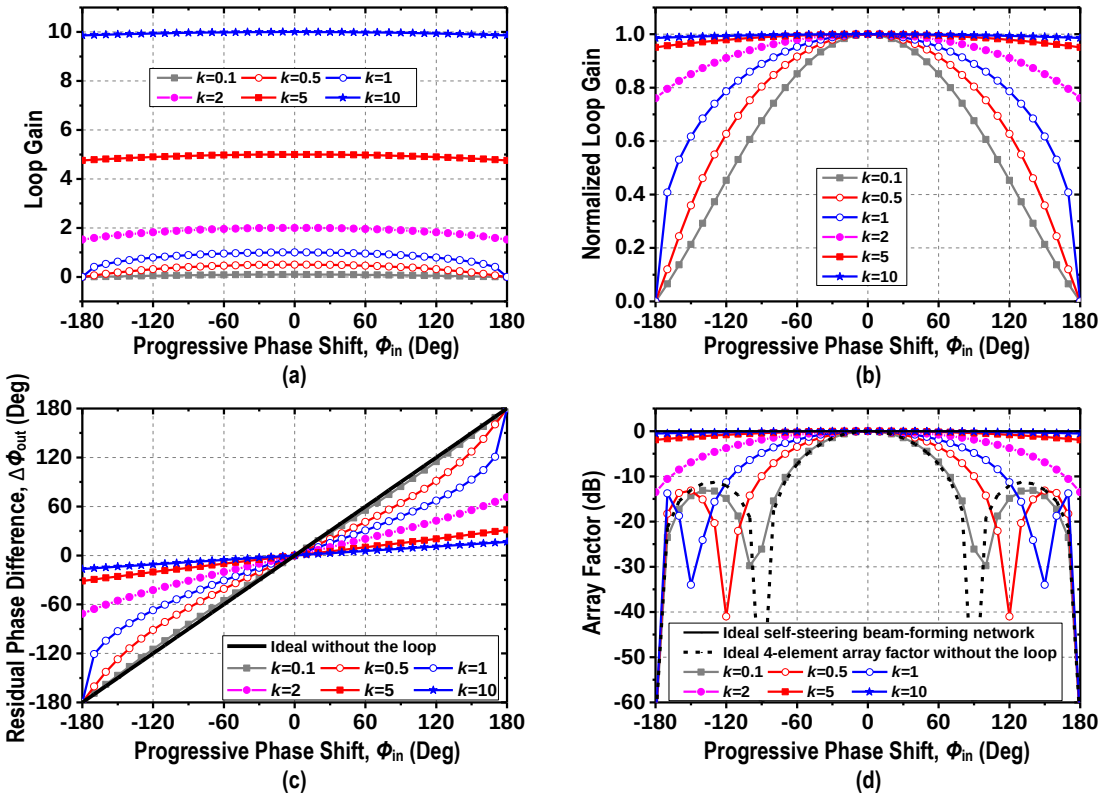

Figure 2.10 – (a) Simulated loop gain versus ϕ_{in} at different k. (b) Normalized loop gain versus ϕ_{in} at different k. (c) Simulated closed-loop $\Delta\phi_{out}$ between path 2 and path 3 versus ϕ_{in} at different k. (d) Simulated normalized array factor versus ϕ_{in} at different k.

The total large-signal loop gain and the normalized array factor are presented versus the input progressive phase difference ϕ_{in} at different k values (Figure 2.10). For a given progressive phase difference ϕ_{in} of the received RF input, the residual phase error $\Delta\phi_{out}$ is calculated using (2.8), and the total loop gain is obtained as $G_1G_2 = (2\alpha\beta^2A^2\sin\Delta\phi_{out}/\Delta\phi_{out})G_2$. The large-signal loop gain peaks at $\phi_{in} = 0°$ and gradually decreases when ϕ_{in} approaches ±180° (Figure 2.10a). The normalized loop gain, i.e., the loop gain at different ϕ_{in} divided by k, is shown in Figure 2.10b. A large k ($k > 1$) always maintains a large loop gain for a given ϕ_{in} within and even at ±180°, while the normalized loop gain drops rapidly when ϕ_{in} approaches ±180° for a smaller k ($k \leq 1$), e.g., for a small input RF amplitude. Such a bifurcation behavior can be observed in Figure 2.10b, and its theoretical basis is explained in the nonlinear feedback loop analysis (Figure 2.9). If $k \leq 1$, the only solution $\Delta\phi_{out}$ is ±180° for $\phi_{in} = ±180°$, and the resulting loop gain drops to zero based on (2.6) and (2.7). However, if $k > 1$, a non-trivial stable solution of $|\Delta\phi_{out}|<180°$ exists for $\phi_{in} = ±180°$, leading to a non-zero loop gain even at $\phi_{in} = ±180°$ based on (2.6) and (2.7) (Figure 2.5b). Figure 2.10c plots $\Delta\phi_{out}$ versus ϕ_{in} for different k values. As k becomes larger, the residual output phase error $\Delta\phi_{out}$ becomes closer to 0 for ϕ_{in} between ±180°, showing the desired phase suppression by the self-steering negative feedback loop. A smaller k ($k \leq 1$) loses the feedback control capability when ϕ_{in} approaches ±180° with the resulting $\Delta\phi_{out} \approx \phi_{in}$, while a larger k ($k > 1$) ensures a large phase suppression even at $\phi_{in} = ±180°$. This is also verified in the large-signal loop gain plots in Figure 2.10a and 10b.

Next, assuming the RF input signals for the four paths have the same amplitude, the normalized array factors can be simulated versus ϕ_{in} at different k values (Figure 2.10d). A significant array factor improvement is achieved when k is large due to the minimized residual phase difference of the four paths even at $\phi_{in} = ±180°$. On the other hand, when k

becomes smaller, array nulls will appear, and the array eventually degrades to a standard 4-element array without self-steering compensation.

The analyses and simulations above demonstrate that our proposed all-passive self-steering beam-former achieves autonomous and substantial array factor improvement with a wide FoV over a standard 4-element phased array. The nonlinear conversions between the voltage and phase signals are exploited to maximize the loop gain. *Most importantly, the proposed all-passive self-steering beam-former forms a nonlinear negative feedback that can provide a large loop-gain and support self-steering operation even when receiving an end-fire signal (ϕ_{in} = ±180°). This significantly expands the array FoV and cannot be realized using linear negative feedback loops.*

2.4 Experimental Results

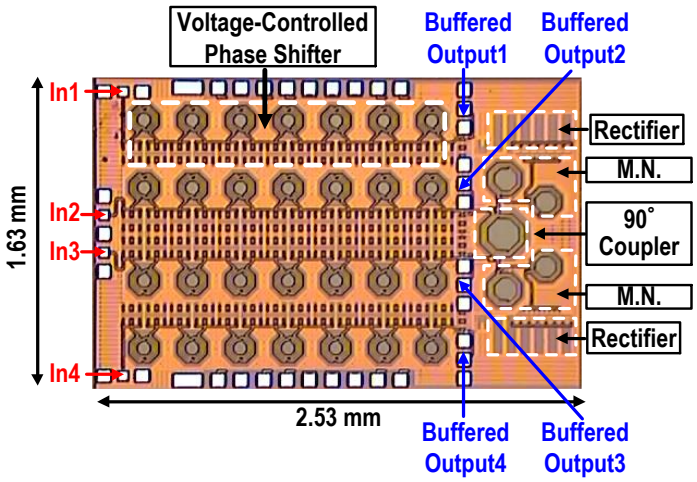

Figure 2.11 – Chip microphotograph.

The all-passive 4-element self-steering beam-former is implemented in a standard 130nm CMOS process with an area of 1.63mm×2.53mm (Figure 2.11). The array measurement setup is shown in Figure 2.12.

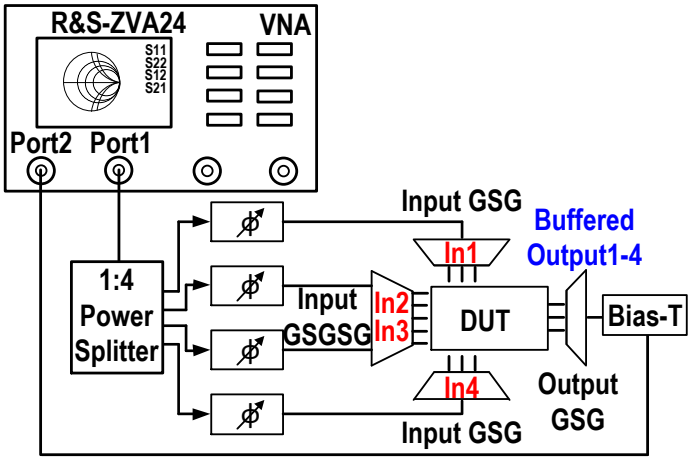

Figure 2.12 – Measurement setup for the closed-loop measurement.

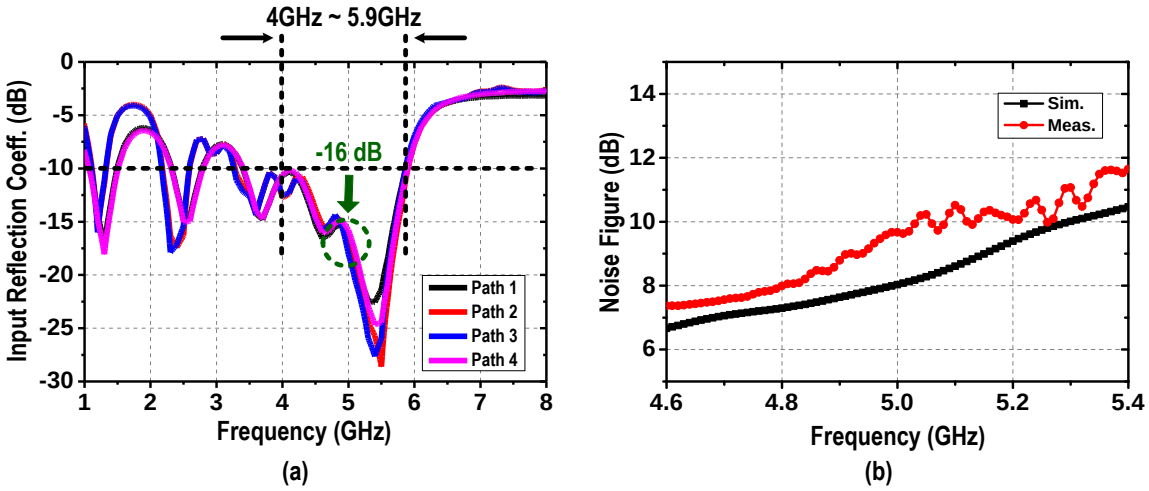

Figure 2.13 – (a) Measured input reflection coefficient of the paths 1-4 with *Pin* = -17dBm/element. (b) Simulated and measured noise figure of the proposed circuit.

A 1:4 power splitter and four phase shifters synthesize the four RF inputs to test the beam-former system. The four open-drain buffered RF outputs are sequentially probed, and the normalized array factor is calculated based on the measured amplitudes and phases of the four buffered RF outputs. The four feedback control voltagesV1 to V4 are also monitored. The input reflection coefficients and the noise figure are first measured by direct probing. A good input matching of the 4 paths is achieved from 4GHz to 5.8GHz

with an RF input power of Pin = -17dBm/element (Figure 2.13a). The measured 4-path input reflection coefficients are similar at different Pin (Figure 2.14). The averaged noise figure of the proposed circuit is measured as 9.5dB (Figure 2.13b), which can be compensated by the front-end LNAs.

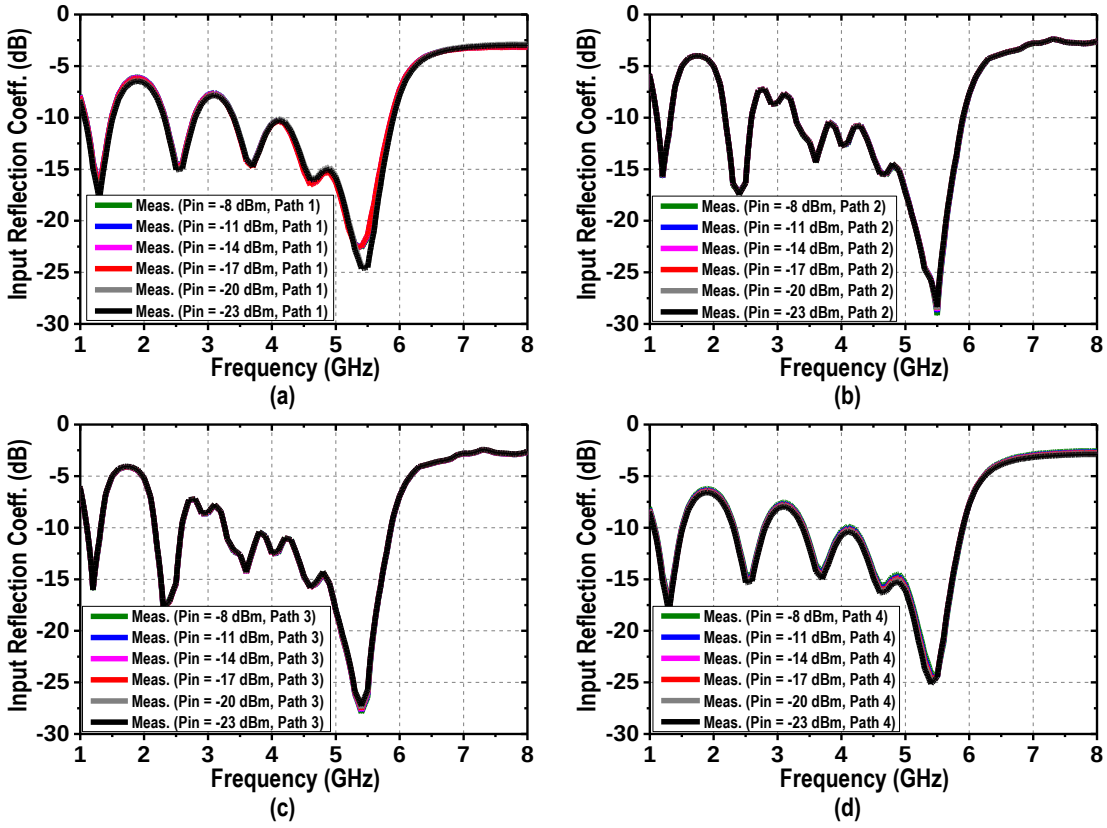

Figure 2.14 – Measured input reflection coefficient of the (a) path 1, (b) path 2, (c) path 3, and (d) path 4 at different RF input power levels (P_{in} per element).

2.4.1 Open-Loop Measurement

To evaluate the open-loop performance, the negative feedback loop is disabled by opening the switches and disconnecting the feedback voltage (Figure 2.3). The measured differential DC feedback control voltage for the path 1 and path 2 versus the open-loop phase error $\Delta\phi_{out}$ is shown in Figure 2.15. Note that $\Delta\phi_{out} = \phi_{in}$, since the loop is open, and

ϕ_{in} is the input progressive phase difference of two adjacent channels. The voltages in the path 1 and path 2 exhibit a sinusoidal behavior versus $\Delta\phi$out from -180° to 180°, agreeing well with the theoretical phase-to-voltage conversion analysis (Section 2.3.1). Moreover, the measured feedback voltage in the path 1 is 3× larger than that in the path 2, verifying that the 3:1 resistive divider at the rectifier output indeed creates a 3× replica control voltage.

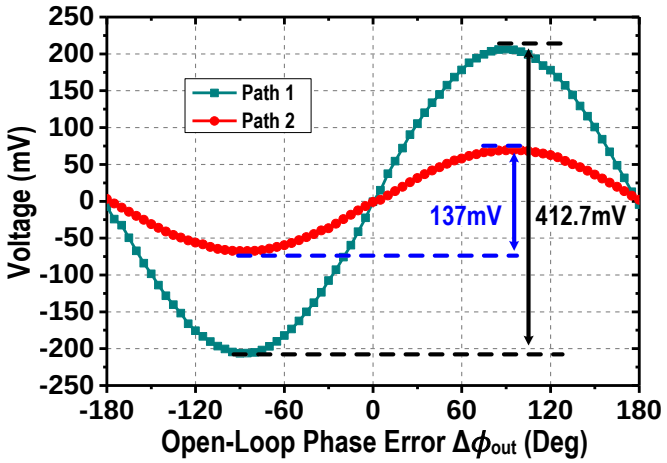

Figure 2.15 – Measured feedback control voltage difference across varactors in the path 1 and path 2 versus the open-loop phase error $\Delta\phi_{out} = \phi_{in}$ with P_{in} = -17dBm/element at 5GHz.

Figure 2.16 shows the measured differential DC feedback voltage in the path 2 versus the open-loop phase error $\Delta\phi$out at different Pin/element. From (2.5), when the input power is increased by 3dB, the Vctrl should be doubled, assuming that the rectifier is a square-law device with a constant conversion coefficient α and a constant coefficient β for the matching network. In measurements, when Pin is increased by 3dB, the measured Vctrl is increased by a factor of 1.9 (Figure 2.16), matching well with the theoretical

analysis. The small difference is possibly due to the conversion coefficient drop at a higher RF input power.

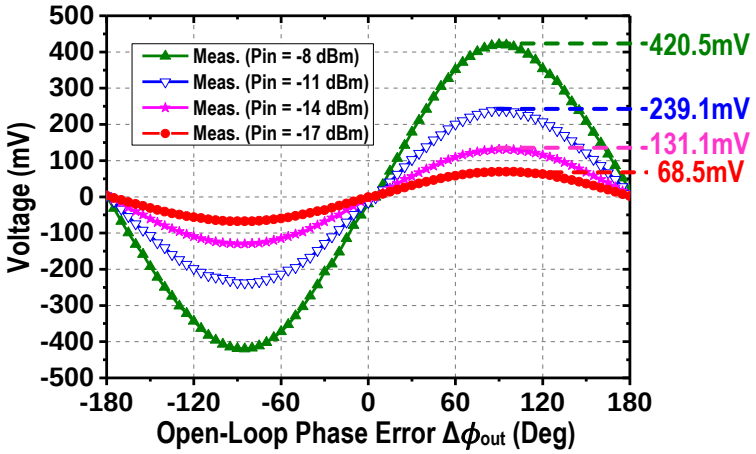

Figure 2.16 – Measured feedback control voltage difference across varactors in the path 1 and path 2 versus the open-loop phase error $\Delta\phi_{out} = \phi_{in}$ with different P_{in}/element at 5GHz.

2.4.2 Closed-Loop Measurement

The measured normalized array factor of the all-passive 4-element self-steering beam-former at 5GHz is shown in Figure 2.17. For an ideal self-steering beam-former, the normalized array factor should be constant at 0dB regardless of the input progressive phase shift ϕ_{in}. On the other hand, a static 4-element phased array with no self-steering compensation shows narrow beam-width with two array factor nulls at $\phi_{in} = \pm 90°$, restricting the FoV. When the self-steering negative feedback loop is enabled, the proposed beam-former achieves significant array factor improvement from -180° to 180°. At P_{in} = -17dBm/element, the measured normalized array factor is -2.87dB/-2.8dB at +90°/−90°, showing >25 dB improvement over the null points when the feedback is disabled. The array factor also improves with a higher RF input power due to the increased feedback loop gain.

The measured array factor reaches -0.15dB/-0.14dB at +90°/−90°with P_{in} = -8dBm/ element. Moreover, a higher RF input power also substantially improves the array factor even at $\phi_{in} = \pm 180°$, benefiting from the nonlinear feedback loop operation of the proposed self-steering beamformer. On the other hand, decreasing the RF input power weakens the array loop gain. Array factor nulls start to appear, and the array performance is eventually degraded to a static 4-element phased array without any compensation, meaning that the feedback loop gain gradually becomes zero.

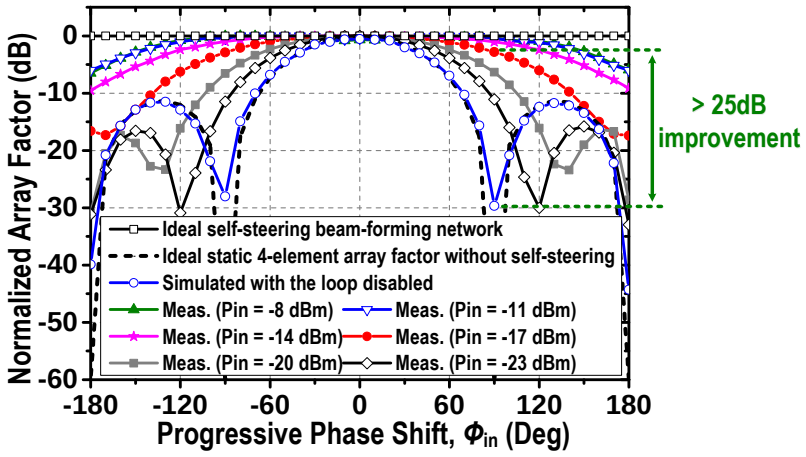

Figure 2.17 – Measured normalized array factor of the 4-element array versus ϕ_{in} with different P_{in} per element at 5GHz.

Figure 2.18 shows the measured array factor at ±90° with and without negative feedback versus P_{in} per element. The negative feedback loop shows substantial effect for Pin > -29dBm/element. Figure 2.19 shows the Monte Carlo simulation result based on 200 samples and a measured normalized array factor of our proposed passive self-steering beam-former circuit with Pin = -17dBm/element at 5GHz. The Monte Carlo simulations use the default Monte Carlo models in the GlobalFoundries GFUS 8RF design kit, including both corner variations and device mismatches. The error bar of the simulated

normalized array factor equals one standard deviation. The measurements (3-mesaurement curves) are based on three independent samples and thus include the random variations and mismatches in practice. Based on our Monte Carlo simulations, the variation of the simulated normalized array factor is within 0.8dB, which shows the robustness of the proposed design.

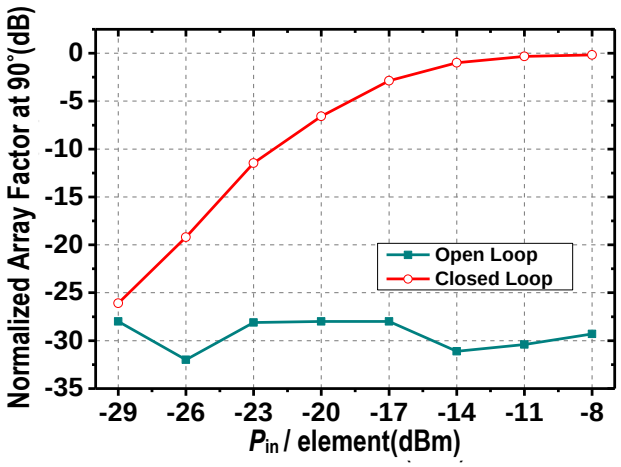

Figure 2.18 – Measured normalized array factor versus P_{in} per element with ϕ_{in} = 90° at 5GHz.

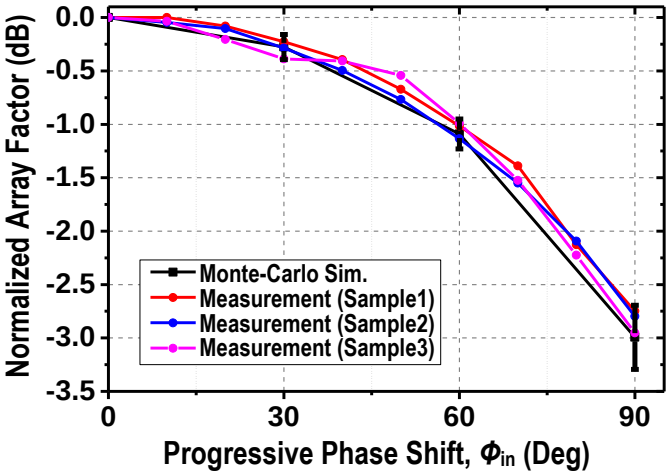

Figure 2.19 – Monte-Carlo simulation result and measured normalized array factor of the proposed passive self-steering beam-former circuit with *P*in = -17dBm/element at 5GHz for three independent chip samples. The highly consistent results show the robustness of the design.

Moreover, the measured normalized array factors for the three independent samples closely match the Monte Carlo simulations, verifying that the process variations and device mismatches will not cause significant degradation in array factor in practice. To characterize the FoV and bandwidth of the proposed beam-former, the FoV is defined by the input progressive phase shift ϕin range, within which the normalized array factor is better than -6dB. The reason to choose -6dB is that a 4-element phased array offers 10×log4=6dB array gain at 0° incidence compared with a single-element receiver. Within the FoV defined by this criterion, the 4-element phased array maintains its array gain advantage over single-element operation.

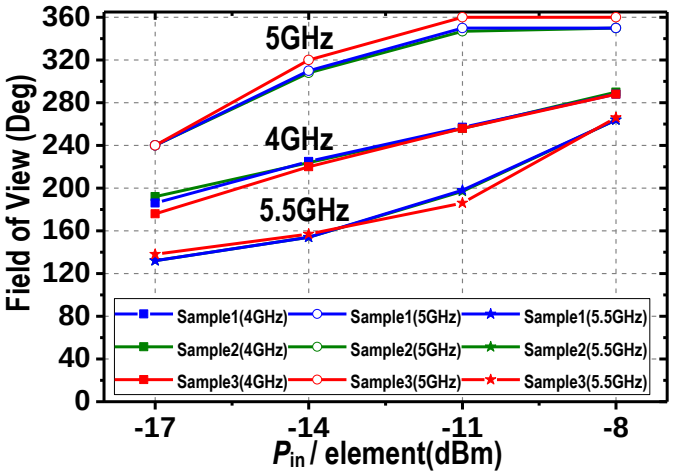

Figure 2.20 – Measured FoV versus P_{in}/element at 4GHz, 5GHz, and 5.5GHz for three independent beam-former chip samples.

At 5GHz, the measured FoV is from -120° to +120° with Pin = -17dBm/element and from -180° to +180° with Pin = -11dBm/element (Figure 2.20), showing a very wide and consistent FoV for all three independent samples. Wide FoV is also achieved at other frequencies (4GHz and 5.5GHz). The measured normalized array factors at different frequencies and different input power levels are summarized in Figure 2.21a - Figure 2.21c.

The proposed all-passive self-steering beam-former achieves a high-performance array factor enhancement from 4GHz to 5.5GHz. The self-steering beam-former fractional bandwidth is defined as the frequency range, within which the array FOV is larger than 180° (±90°) for a given RF input power. Based on the measurements, the fractional bandwidth versus the input power for three independent samples is summarized in Figure 2.21d. At -17dBm/element input power, the measured fractional bandwidth is 26%, which is expanded to 35% for -8dBm/element, demonstrating a broadband operation.

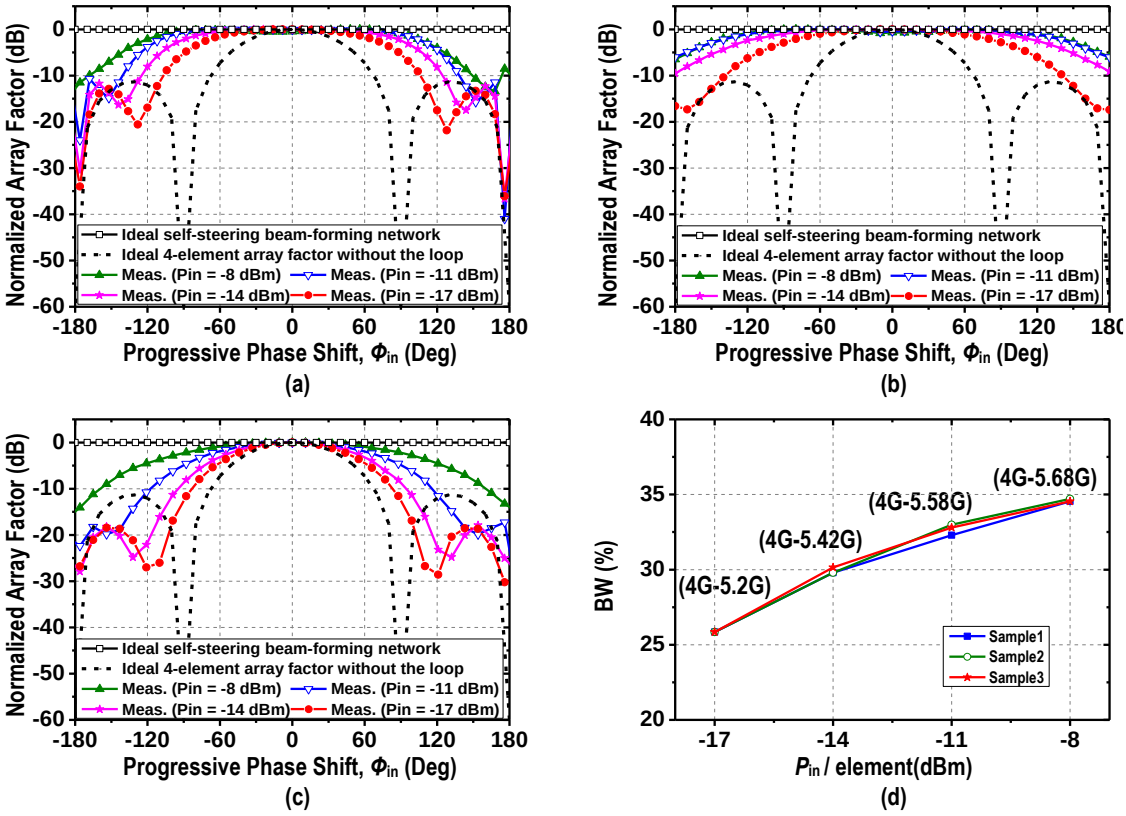

Figure 2.21 – Measured normalized array factor of the 4-element array versus ϕ_{in} with different P_{in}/element at (a) 4GHz, (b) 5GHz, and (c) 5.5GHz. (d) Measured fractional bandwidth versus different input power for three independent beamformer chip samples.

2.4.3 Time-Domain Response Measurement

The time-domain response of a self-steering beamformer is critical, since it governs how fast the system can perform BF in response to the onset of an input or beam-tracking to a varying input, i.e., a moving source target. The time-domain response measurement setup is shown in Figure 2.22.

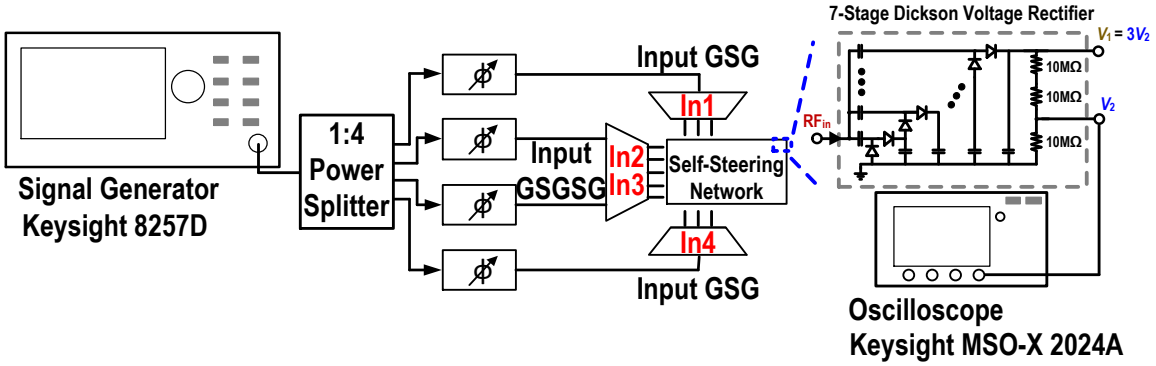

Figure 2.22 – Measurement setup for the system response time measurement.

The input RF signal (Pin = -17dBm/element) is generated by a vector signal generator (Keysight 8257D) with an OOK modulation, and the input progressive phase shift ϕ_{in} is generated by the off-chip phase shifters to synthesize the incident wave for the self-steering beamformer chip. The time-domain response is measured by monitoring the DC feedback voltage on a real-time oscilloscope (Keysight MSO-X 2024A). On the beamformer IC, each DC feedback voltage node from the rectifiers is connected to 14 differential varactors in the phase shifters with a total capacitive loading of 168pF, which, together with the resistive load (~30 MΩ), forms the dominant pole of the negative feedback loop. Figure 2.23a shows the measured time-domain waveform of the DC feedback voltage at ϕin = 90°, showing a measured time constant of 3ms. The measured time constant versus ϕin is summarized in Figure 2.23b, showing a similar time constant

over a wide FoV. The proposed all-passive self-steering beam-former achieves an acquisition time constant of several milliseconds, which is similar to the active self-steering beam-formers and is fast enough for many phased array beam-forming applications [23]-[25]. The proposed all-passive self-steering beam-former is compared with the state-of-the-art active designs in the Table I. It demonstrates superior performance, including broad bandwidth, wide FoV, and large array factor improvement, all with zero DC power consumption.

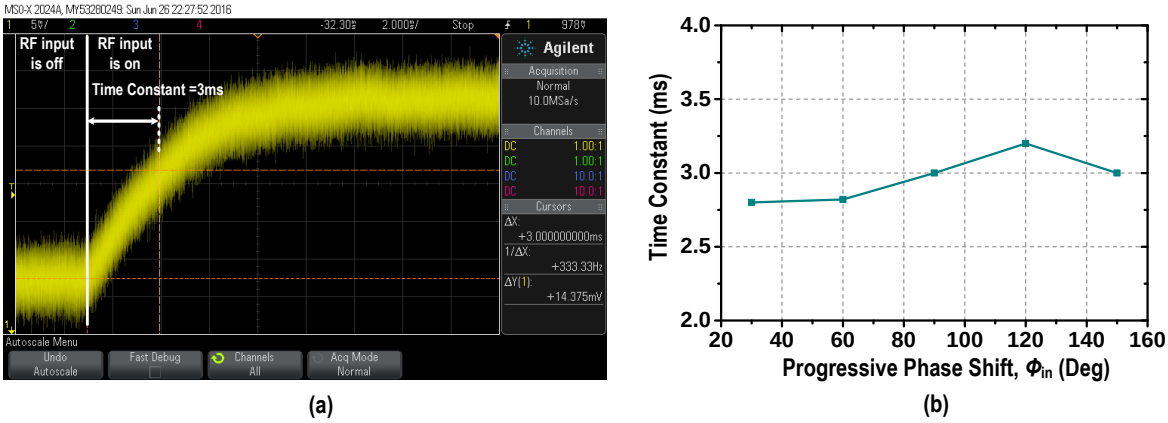

Figure 2.23 – (a) Measured time-domain response of the DC feedback control voltage V_2 with -17dBm/element at 5GHz for ϕ_{in}=90°. (b) Measured time constant versus ϕ_{in} with -17dBm/element at 5GHz.

Table 2.1 – Performance Summary and Comparison with State-of-the-Art Beamformers

	Self-Steering (No External Controls)	Element No.	Freq. (GHz)	BW	DC Power (mW)	FoV‡	Normalized Array Factor versus Input Progressive Phase Shift $??_{in}$	Topology	Area (mm^2)	Tech.
[9]	No	2	11.2	N/A	36	±120°	N/A	ILOA	1.2 (with pads)	180nm CMOS
[10]	No	3	2.68-2.72	1.5%	725*	-28°~+39°	N/A	ILCOA	N/A	Not Fully Integrated
[8]	No	4	42.8-49.5	14.5%	85	±90°	N/A	ILOA	2.8 (core area)	65nm CMOS
[5]	Yes	2	1.425	N/A	430*	±155°	N/A	Open Loop Phase Detection + Feedforward Phase Correction	N/A	Not Fully Integrated
[6]	Yes	4	6.5	N/A	565*	-90°~+127°	N/A	Power Detector + DSP	N/A	Not Fully Integrated
[7]	Yes	4	7.4-9.4	23.8%	143	±100°	-3dB@60°/-7dB@90°**	COA + CPLL	3.5 (with pads)	45nm CMOS SOI
This Work	**Yes**	**4**	**4-5.68**	**34.7%**	**0**	**±120°† ±180°††**	**-1.1dB@60°/ -2.87dB@90°† -0.1dB@60°/ -0.15dB@90°/ -5.9dB@180°††**	**All-Passive Nonlinear Negative Feedback Loop**	**4.1 (with pads)**	**130nm CMOS**

* Estimated DC power consumption
**Estimated based on the measurement figures in [7]
† P_{in} = -17dBm/element at 5GHz
†† P_{in} = -8dBm/element at 5GHz
‡ The FoV is defined by the input progressive phase shift ϕ_{in} range, within which the normalized array factor is better than -6dB for the proposed circuit.

CHAPTER 3. A FULL FIELD-OF-VIEW SELF-STEERING BEAMFORMER FOR 5G MM-WAVE FIBER-WIRELESS MOBILE FRONTHAUL

The upcoming new radio access allows ultra-high data rate using mm-Wave frequencies, while it normally suffers from large path loss. To compensate for path loss, phased arrays for both the transmitter and receiver are used. The 5G new radio (NR) three beam management process proceeds as follows: the transmitted beam is first swept in the downlink direction from the remote radio unit (RRU) to the user equipment (UE), and then the uplink beam is aligned to determine which beam direction has the best reception quality, and vice versa. However, this sequential beam management requires that the RX must be able to perform both beam detection and steering across all the reception angles. Moreover, due to the narrow beamwidth of the phased array operation, a "quantum leap" performance improvement of the receiver operating at mm-Wave is required. In this paper, a self-steering array beamformer (SSA-BF) receiving system is proposed, which is composed of a homedesigned IC package with zero DC power consumption and a 4-element antenna array. We firstly conduct the measurement without the antenna, and the SSA-BF receiver shows a significant array factor enhancement with negligible SNR degradation over full FoV (incidence angle = ± 90°), < 3ms fast beam alignment time and it can support enhanced mobile data-rate up to 10 Gb/s and 7.8 Gb/s with 20x100MHz carrier aggregation OFDM in back-to-back and over 25-km fiber transmission, respectively. Moreover, a broadside 3-dB beamwidth ±80° and broadband 17-36GHz antenna is designed for the proposed SSA-BF receiver in a 5G fiber-wireless access. The

SSA-BF receiving system with the 1×4 antenna array is designed at 28GHz and it shows the normalized array gain better than 3- and 6-dB degradation over broad FoV incidence = ± 68° and ± 85°, respectively. Without any external tuning controls, the proposed SSA-BF achieves the state-of-the-art autonomous beamforming for 6Gb/s 64-QAM signal over 50-cm wireless distance, achieving a substantial array factor improvement. To the best of authors' knowledge, this is the first demonstration of a high-speed switching SSA-BF receiver in a fiber-wireless integrated radio access as a true enabler for mm-Wave mobile fronthaul applications.

3.1 Introduction

To support future wireless communication systems, such as 5G new radio (NR), orthogonal frequency division multiplexing (OFDM) using radio over fiber (RoF) technique in radio access network (RAN) [26] is adopted and standardized because its manageable signal processing resources enable flexible software defined RF operations and simplifies the remote radio units (RRU) architecture [28]-[37]. However, mm-Wave 5G-NR is susceptible to atmospheric attenuation such as water vapor and oxygen, suffering from higher wireless propagation loss. Therefore, in 5G communication network, RRUs can leverage large array sizes to substantially compensate the millimeter-wave (mm-Wave) link loss. [28]-[66]; however, it results in a "pencil-like" beamwidth, which drastically complicates and poses challenges in the beam alignment for the transmitter and receiver. Moreover, unlike conventional static microwave beamforming in satellite communication, many future mm-Wave links are expected to operate in relatively "dynamic" environments, such as wireless AR/VR and machine-based communications, necessitating fast and precise beam-forming/-tracking to ensure high link reliability, enhanced data-rate and low

latency, as shown in Figure 3.1. Furthermore, future dense deployment of mm-Wave small cells will result in a complex EM inter-cell interference and thus beam management is extremely important.

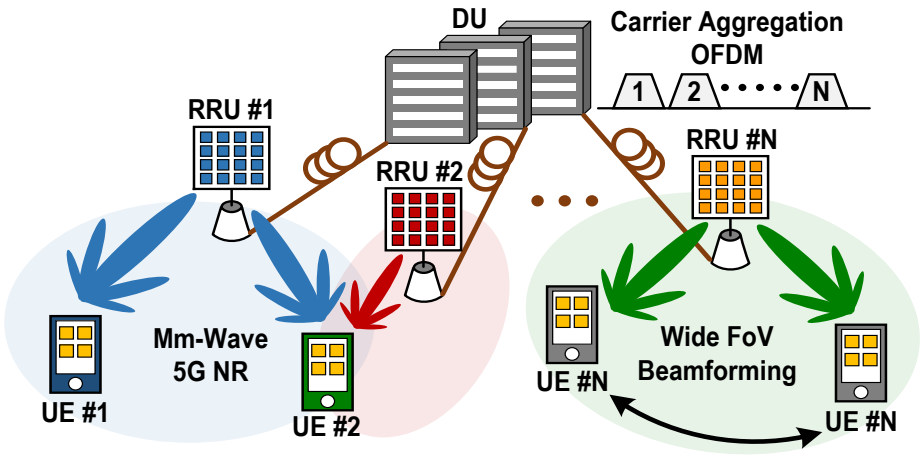

Figure 3.1 – Dynamic 5G fiber-wireless communication for uplink.

Beam management is composed of the following three step sequence[27], which are initial beam acquisition, transmitter beam refinement, and receiver beam refinement. We utilize the downlink as an example to elaborate the beam management process; while the uplink can follow the similar method in a reverse transmission direction. To initial a data delivery for an idle user, the RRU first transmits and sweeps the beam to different directions via a synchronization signal burst set. Then, the UE will find the best-connected beam and feedback the information to the RRU. After the RRU knows the selected beam information, the second step will repeat the sweep process with a narrower beamwidth to UE and get a more accurate UE direction. To get the full beamforming gain, the receiver needs to refine and compute its receiving direction by reusing the beam information from the previous step. However, most receiver phase arrays have non-uniform array factor over scanning angles which can cause misjudgments in the beam alignment, for example, ± 30°

and ± 90° incidences in a generic 4-element phase array antenna receiver. Therefore, to ensure UE feedback the accurate beam connection information in the first and second steps, 5G-NR beam management requires an advanced receiver design with fast beam scanning, searching, beamforming, and computation and it is necessary to have the capability for detecting and performing beamforming over full reception angle.

Most existing beamforming systems in 5G fiber-wireless access are open-loop operations, which require extensive phase control signals [29]. Recently, photonic-aid beamformer (BF) with higher operation bandwidth was reported based on array waveguide grating and dispersive fiber [30]; however, its feasibility is limited by its bulky sizes and thus it causes system stability issue due to environmental vibration, pressure, and temperature changes, which is problematic to precisely and stably align the beam toward the location of the user equipment (UE). Photonic integrated circuit based phased array with 9.61 Gb/s has been demonstrated in [31]. However, the thermo-optical ring-resonator phase shifter is also sensitive to environmental temperature and difficult to achieve fast beamforming. Multiple calibrations are required to facilitate accurate beam-tracking, adding system complexity to future 5G ultra-reliable low-latency link.

To address these challenges in future dynamic mm-Wave mobile applications, we present a mm-Wave fiber-wireless integrated network with a broadband scalable full-FoV self-steering array beamformer (SSA-BF) over 25 km fiber link. The SSA-BF achieves calibration- and digital signal process (DSP)-free beamforming via zero-DC power consumption IC [16][67] with a passive delay-locked-loop (DLL) phase domain negative feedback loops to cover 2-GHz wide bandwidth. A proof-of-concept experiment demonstrates that it can rapidly yet accurately align the desired signals with low-latency <

3ms beam-tracking and exhibits long-term system stability. The network has been demonstrated by probing-based measurement and it can achieve 20 x100-MHz carrier aggregation OFDM with aggregating 10Gb/s. In the over-the-air measurement, 6Gb/s 64-QAM single-carrier signal is transmitted over 50-cm wireless distance for future high-speed and dynamic mm-Wave 5G fiber-wireless systems. This Chapter is organized as follows. Section 3.2 presents the wideband full-FoV fiber-wireless SSA-BF system architecture. The operation principle and implementation details of the zero-DC SSA-BF IC as well as the wide-FoV antenna array design are demonstrated in Section 3.3. Section 3.4 shows the measurements and a performance comparison with various reported fiber-wireless systems.

3.2 Fiber-Wireless Self-Steering BF

The proposed SSA-BF receiver system for a fiber-wireless network uplink includes mm-Wave front-end low noise amplifiers (LNAs), down-conversion mixers, zero-DC SSA beamforming IC package and electrical to optical converter (E/O converter). A proof-of-concept fiber-wireless system is designed at 28GHz for mm-Wave 5G NR.

After down-conversion mixing, the IF signal is then sent to the home designed IC for conducting beamforming, including the detection of angle of the arrival signal and beam alignment. The closed-loop IC consists of a passive power-aware phase detector, time-delay-based LC synthetic phase shifters, and resistive progressive feedback control voltage generation [67]. As shown in Figure 3.2a, the negative feedback loop is realized by the passive phase detector with phase-to-voltage conversion G1 and a DLL-based voltage-controlled phase shifter with voltage-to-phase conversion G2 (Figure 3.2b). In order to

execute this close-loop beamforming operation, we have to ensure a large loop gain (LG) = G1G2 for autonomous operation over full-FoV and self-steering operation with zero DC power consumption [67].

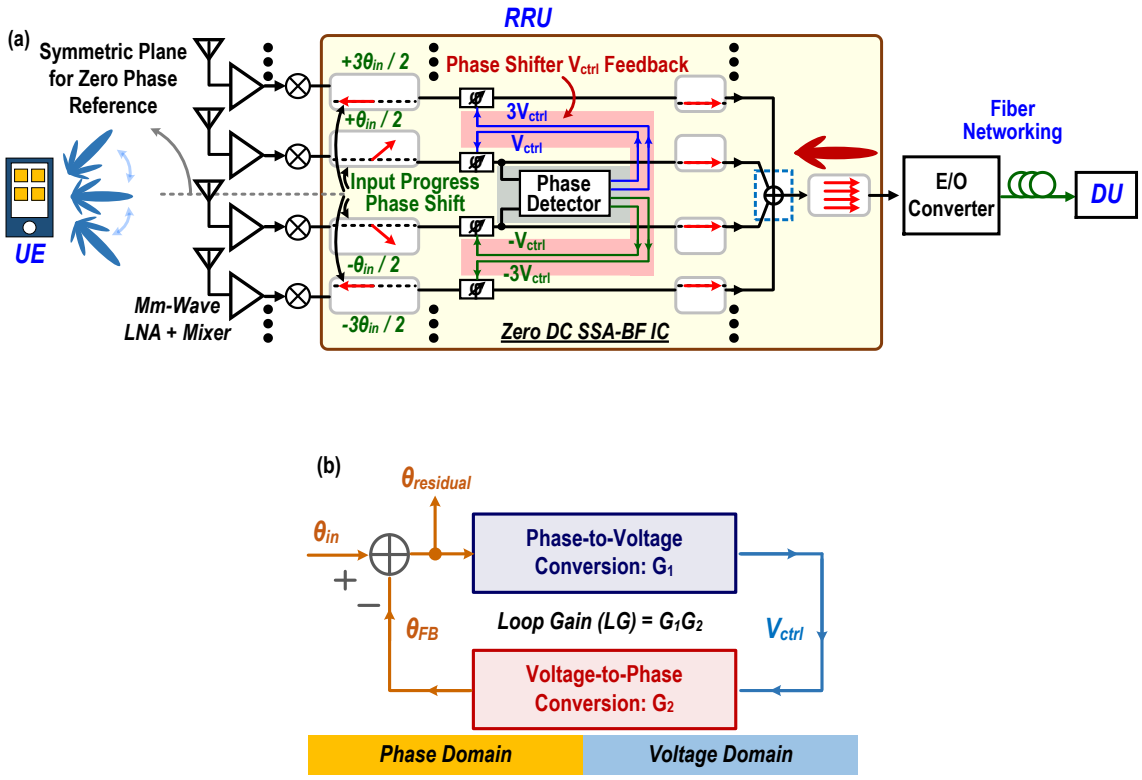

Figure 3.2 – (a) Operation principle of the full-FoV DLL-based negative feedback. (b) Conceptual diagram for scalable fiber-wireless SSA-BF.

In the first step of beamforming, when the incoming signals with an incident angle ϕ are injected into the receiver with a uniform $\lambda/2$ array (Figure 3.2a), the middle two paths would induce the input progressive phase shift (IPPS) is $\theta_{in} = \pi\sin\phi$. Then, the successively power-aware phase detector would react to that phase deviation and feedback the compensation voltage V_{ctrl} for phase shifters to generate θ_{FB}. Since it is a close-loop feedback manipulation, the feedback phase θ_{FB} would be subtracted from the input signal

and thus reduce the phase difference in the adjacent paths. The residual output phase deviation θres can be expressed as [16][67]:

$$\theta_{res}=\theta_{in}/(1+G_1G_2). \quad (3.1)$$

It is worth to note that θ_{res} is minimized as the total loop gain G_1G_2 is maximized, which implies a high accuracy for beam alignment of the received signal over a wide progressive phase shift range θ_{in}, i.e. wide FoV. The nonlinear conversion between the phase and voltage domain is further exploited in Section 3.3.1 to be extremely large even at end-fire incident angle (i.e. $\theta_{in} = \pm 180°$ and $\phi = \pm 90°$) [16][67].

The SSA beamforming IC can be scalable for a large-scale phased array via generating a set of progressive feedback control voltages from the power-aware phase detector for the preceding phase shifters to align the entire array. For example, in Figure 3.2a, $-3V_{ctrl}$, $-1V_{ctrl}$, $1V_{ctrl}$, and $3V_{ctrl}$ are generated for a uniform 1×4 array to compensate the input IPPS. After this autonomous phase detection and alignment, the N output channels are in-phase summed up to achieve a beamforming gain with 10logN signal-to-noise ratio (SNR) and array factor enhancement. The SSA beamforming IC acts only on the signal power due to its nonlinear loop operation [67] and does not need any prior signal knowledge of angle of arrival information. Moreover, the all-passive design ensures its zero DC operation power, which is important for large-scaled phased arrays. To conduct the upstream signal transmission, the beamformed signal is then upconverted by an E/O converter and then sent to distributed unit (DU) through the dedicated fiber links. Detailed system design and implementation are shown in the Section 3.3.

3.3 System Implementation and Analysis

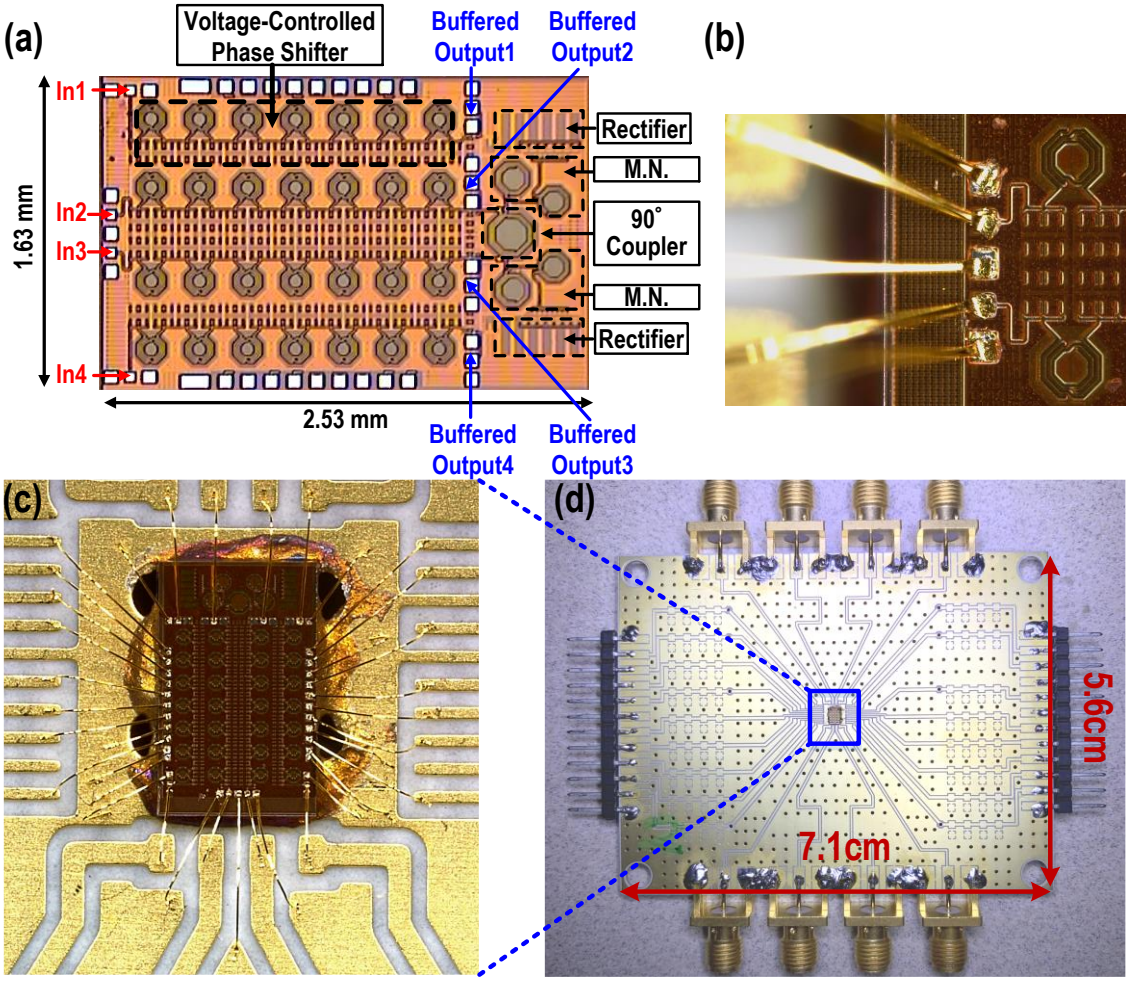

Figure 3.3 – (a) Chip microphotograph. (b) Zoom-in view, (c) complete wire-bonding view, and (d) full package of the zero-DC SSA-BF IC.

3.3.1 Operation of the Zero DC SSA beamforming IC

To demonstrate the proposed the mm-Wave fiber-wireless network with a full-FoV autonomous beamforming receiver, a proof-of-concept DLL-Like SSA beamforming IC is implemented in a 130nm CMOS process with a size of 1.63 mm×2.53 mm [67] and then packaged in low-loss FR4 PCB with an area of 5.6cm×7.1cm to process the down-conversion 4-6 GHz IF signals (Figure 3.3). The closed loop converts signals between two

different domains, i.e., phase and voltage domains, and the loop gain is explored to be extremely large even the circuitry is all-passive with zero DC power consumption [67].

3.3.1.1 Phase-to-Voltage Feedforward Conversion G1

The phase-to-voltage feedforward convertor (phase detector) consists of a compact single-ended 90˚ coupler and a 7-stage Dickson voltage rectifier [16][67]. The coupler is designed as a transformer-based poly-phased network [21][68] [69] for a compact low-loss IQ generation [16][67]. When the two signals in the adjacent path with IPPS = θ_{res} and with same amplitude A are injected to input and isolation ports of the 90° coupler, output signals at the through and coupled ports of the coupler are then followed by passive matching networks and the two 7-stage Dickson voltage rectifiers [67]. Assume that two matched rectifiers are as square-law devices, after the rectification, the differential DC voltage signal Vctrl of the rectifier outputs can be expressed as [67]

$$V_{\text{ctrl}} = 2\alpha\beta^2 A^2 \sin\theta_{res}, \tag{3.2}$$

where the factor β is the passive voltage amplification by the matching network and the coefficient α is rectification efficiency [67]. Note that the phase-to-voltage conversion is proportional to signal power A^2 and it is a power-aware phase detector without prior knowledge on angle of arrival. The differential DC outputs V_{ctrl} of the rectifiers are then sent to phase shifter to generate the feedback compensation phase θ_{FB}. The phase-to-voltage feedforward conversion is [67]

$$G_1 = V_{\text{ctrl}}/\theta_{res} = 2\alpha\beta^2 A^2 \sin\theta_{res}/\theta_{res}. \tag{3.3}$$

3.3.1.2 Voltage-to-Phase Feedback Conversion G2

To support wideband modulated signal for 5G NR, the zero DC SSA beamforming IC chooses DLL-based delay line for wideband phase shifting and signal processing. It is composed by a multi-section LC network as synthetic transmission lines for true-time delay [67]. The varactors in the multi-section LC network are controlled by the V_{ctrl} to generate corresponding feedback θ_{FB}, aligning adjacent channels and suppressing the $\theta_{res.}$. The voltage-to-phase feedback conversion is [67]

$$G_2 = \theta_{FB}/V_{\text{ctrl}}. \tag{3.4}$$

The overall loop gain G_1G_2 is exploited to be large even all of them are passive components and the large loop gain value is maintained over a wide FoV [67]. Moreover, the V_{ctrl} generated from rectifier outputs of G_1 are further scaled via the resistive dividing loads [67] to generate progressive $\pm V_{ctrl}$, $\pm 3V_{ctrl}$ for inner or outer path phase shifting (Figure 3.2a), achieving a large-scale phased array.

3.3.1.3 Loop Analysis of zero-DC SSA beamforming IC

The overall closed loop of the zero-DC SSA beamforming IC is next analyzed. First, the output residual phase difference θ_{res} can be expressed as [67]

$$\begin{aligned}\theta_{res} &= \theta_{in}/(1 + G_1G_2) \\ &= \pi\sin\phi/\,[1+ (2\alpha\beta^2A^2\sin\,\theta_{res}/\theta_{res})G_2].\end{aligned} \tag{3.5}$$

Under different θ_{res}, the feedforward conversion gain G_1 varies during the feedback phase compensation and it is not a fixed value, showing the negative feedback loop is a nonlinear loop. It can be further modified as

$$\theta_{res} + k \sin \theta_{res} = \pi \sin\phi, \tag{3.6}$$

where $k = 2\alpha\beta^2 A^2$, which is the loop gain value at incidence ϕ = 0º. Moreover, k is with a quadratic relationship to the incident signals amplitude, showing that the loop response is a function of the signal input power. Moreover, the transcendental equation (3.6) is further explored to achieve effective phase error reduction and high alignment accuracy. For a linear loop operation, the loop gain is normally peaking at broadside incident angle (ϕ = 0°) and gradually decreasing when the signal is injected from end-fire region (ϕ = ±90°). However, due to its nonlinear bifurcation behavior, the proposed power-aware closed loop can still maintain its large loop gain value across a large incident angle coverage and even at ϕ = ±90° or IPPS θ_{in} = ±180°, showing the full-FoV operation as long as the k is >>1 [67].

For the stand-alone SSA beamforming IC measurement, it can achieve wideband input matching (S_{11}< -10dB) from 4 to 5.9 GHz to support wideband IF signals. With the feedback off, the zero-DC SSA beamforming IC behaves as a broadside phased array and forms an array factor null at IPPS θ_{in} = ±90° and ±180°, i.e., ϕ = ±30° and ±90°, in a uniform four-element array. With the feedback on, the measured normalized array factor of the SSA beamforming IC achieves significant array factor improvement (at least > 25dB) over full-FoV, i.e., IPPS from −180° to 180° [67]. Moreover, with a higher input power, the measured normalized array factor can be further improved over full-FoV because of its nonlinear operation [67]. The array FoV is significantly expanded which cannot be realized via a linear feedback loop. Moreover, the proposed feedback operation

is robust to corner variation and device mismatch and provide accurate phase shifting based on multiple chip sample measurements and Monte Carlo modeling simulations [67].

To achieve a larger LG and minimize the residual phase difference of the four paths even at end-fire incidence (IPPS = ±180° or ϕ = ±90°. Mm-Wave frontend LNAs and down-conversion mixers are applied before the SSA beamforming IC package to increase loop conversion gain and lower the system noise figure with better sensitivity. The IC package is wire bonded on the FR4 PCB and experimentally verified with Mm-Wave frontends as a Mm-Wave SSA-BF system. Overall nonlinear loop gain of the system is increased to achieve a flat normalized array factor over full-FoV, supporting the proposed SSA-BF to preserve self-steering operation even when receiving an end-fire signal (IPPS = ±180° or ϕ = ±90°). Moreover, the signals are operated in DLL-like loop, which can support wideband modulated signal through the following optical fiber as a proof-of-concept mm-Wave mobile fronthaul.

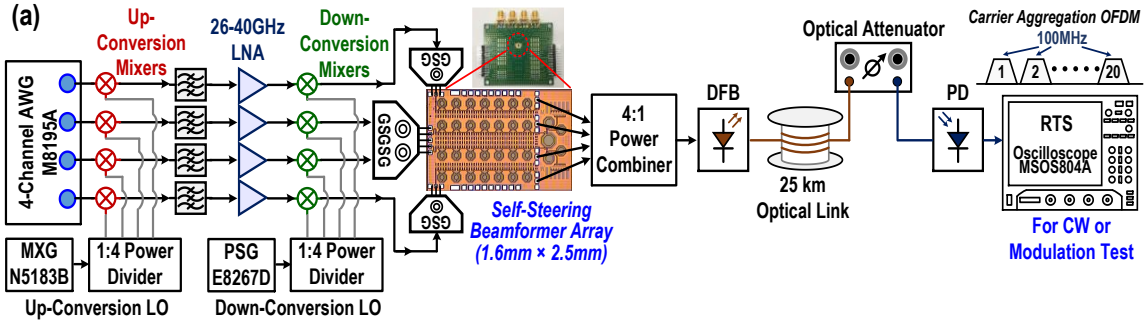

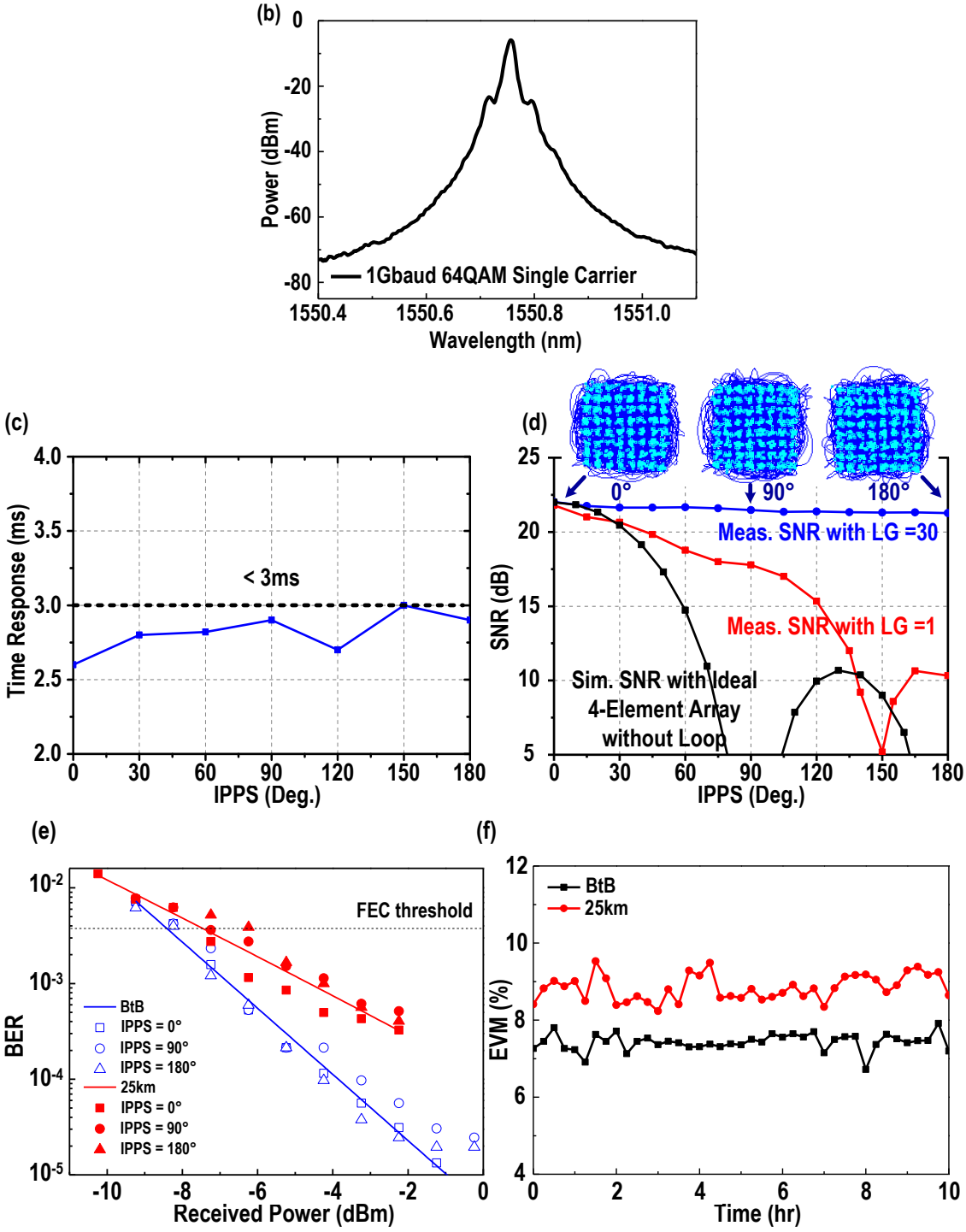

Figure 3.4 – (a) Experimental setup. (b) Optical spectrum of 1Gbaud 64QAM single carrier. (c) Response time of the SSA-BF mm-Wave SSA-BF fiber fronthaul system. (d) Received SNR versus IPPS. (e) The BER performance of 1Gbaud 64QAM single carrier with different IPPS in BtB and over 25-km fiber link. (f) Stability measurement of 1 Gbaud 64QAM single carrier over 10 hours.

3.3.1.4 Experimental Verifications of SSA-BF with Fiber Link

The experimental setup of the proposed SSA-BF with fiber link is illustrated in Figure 3.4a. We apply a 4-channels 16 GSa/s arbitrary waveform generator (AWG) to mimic the wireless signals with different incident angles as electrical phase shifting generation. The applied signals for this SSA-BF measurement are 1 Gbaud single carrier 64QAM, 10 and 20 100-MHz carrier aggregation of OFDM signal, which is generated via ordinary DSP [70][71], including serial-to-parallel, inverse FFT, and cyclic prefix insertion. The output signals are firstly up-converted to 28 GHz for 5G-NR applications via a local oscillator (LO) and then pass through bandpass filters for sifting out the unwanted LO leakages. 4 LNA with 2 dB noise figure from 26 to 40 GHz are employed to boost the input power up to 10 dBm before the proposed SSA-BF. It is worth bearing in mind that those wideband LNAs are applied for supporting multiple 5G-NR bands (especially at 28, 37, and 39 GHz), supporting future multi-standard communication and international roaming. After down-conversion to 5-GHz as center frequency, the 4 IF signals with corresponding IPPS are sent into the proposed SSA-BF, which the PCB and chip photo of the SSA-BF are also shown in Figure 3.4a.

After autonomous beamforming, the 4 in-phase output signals are directly summed up by a 4-by-1 power combiner and delivered to a direct modulation distributed feedback (DFB) laser with 1550.76 nm central wavelength and 5.5-dBm output power. After 25-km fiber link, an optical attenuator and a10-GHz commercial photodetector is used to convert optical information to electrical domain for testing received performance. After analog-to-digital conversion via a 20G GSa/s real-time oscilloscope (RTS), the received signals are then evaluated via their EVM, BER, SNR, and their corresponding constellation diagrams.

Due to fully symmetric performance of the SSA-BF [67], a representative IPPS from 0˚ to 180˚ is used to characterize in this measurement. The optical spectrum of 1 Gbaud 64QAM (6Gb/s) single carrier after 25-km transmission is shown in Figure 3.4b. Figure 3.4c demonstrates that the mm-Wave SSA-BF fiber fronthaul system can achieve low-latency response time < 3ms over full-FoV, supporting future dynamic 5G networks. The SSA-BF is also tested with wideband modulated 1 Gbaud 64QAM (6Gb/s) signal under different LG setting over full FoV and 25-km fiber link transmission. With a medium LG = 30, it remains similar SNR and shows clear constellations over full FoV in Figure 3.4d. Figure 3.4e exhibits the BER performance of the proposed full-FoV mm-Wave SSA-BF fiber fronthaul system with different IPPS. Again, the received performance is similar even when the IPPS is at end-fire 180˚. The received sensitivities, defined as the received power at the FEC criterion, are -8 and -7 dBm for BtB and 25km respectively. A 1 dB power penalty is measured due to the fiber dispersion. In Figure 3.4f, over ten hours, stable EVM performance of 1 Gbaud 64QAM (6Gb/s) single carrier is measured with 7.4% and 8.8% in BtB and 25-km scenario, showing that the SSA-BF fiber-wireless system still provide stable beamforming for the input wideband modulated Gb/s signal with a consistent EVM performance.

Figure 3.5a shows the electrical spectra of 10 carrier aggregation of 100 MHz OFDM bands with an accommodated 1 GHz bandwidth. Each of them has similar SNR and the average BER performance shows the received sensitivity (FEC threshold BER = 3.8×10^{-3}) is -6 dBm of the BtB scheme and -5 dBm after the 25 km link respectively in Figure 3.5b. Compared to the 1 Gbaud 64QAM (6Gb/s) single carrier, the performance of the OFDM signals is slightly degraded due to higher PAPR and lower SNR under the constrained

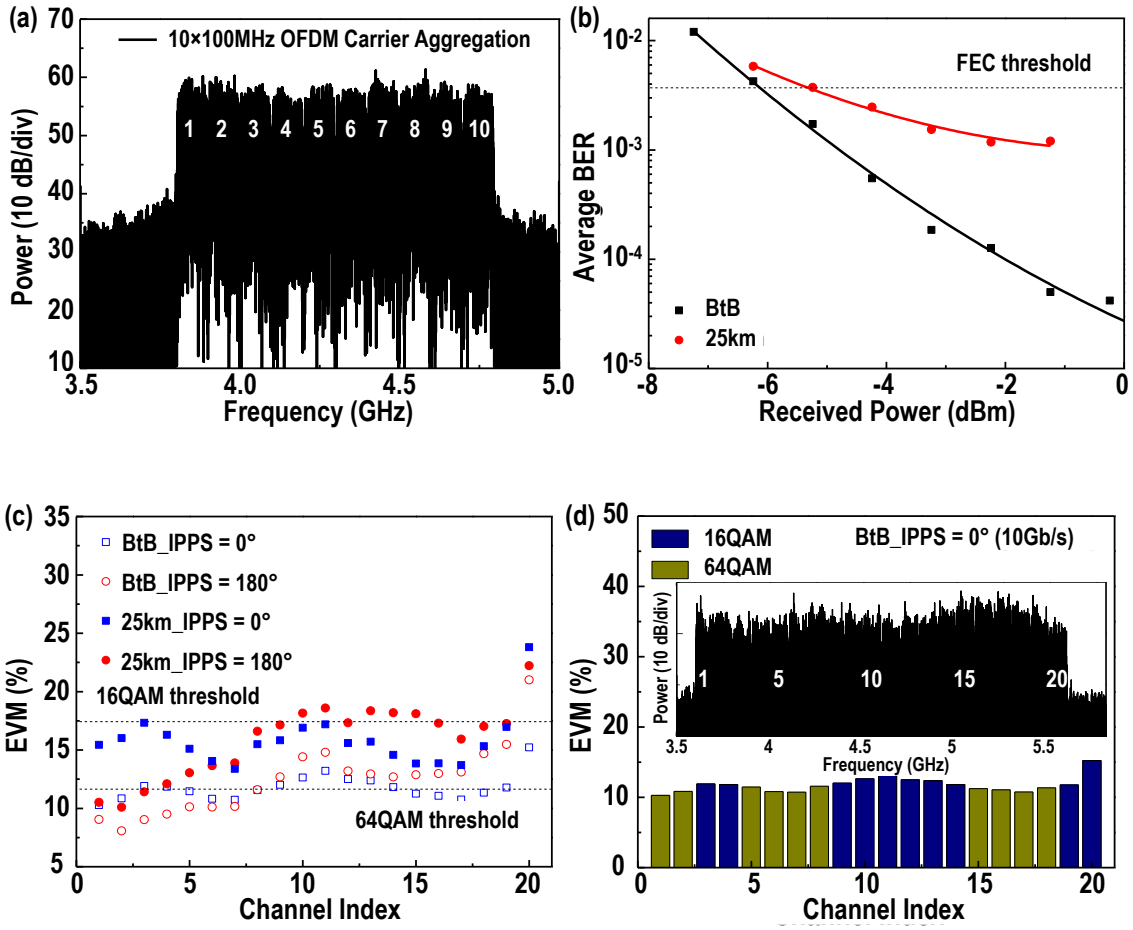

Figure 3.5 – (a) Electrical spectrum of 10 carrier aggregation of 100 MHz OFDM signals in BtB scheme. (b) Average BER performance of 10 carrier aggregation in BtB and over 25km. (c) EVM performance of the 20 × 100 MHz carrier aggregation OFDM as IPPS = 0˚ and 180˚ IPPS. (d) upper inset, 20 × 100MHz signal; lower inset, maximum EVM in achievable QAM level BtB scheme with IPPS = 0˚ (64QAM × 10, 16QAM × 10).

linearity of the front-end LNAs. To further enhance mobile data capacity of the proposed mm-Wave SSA-BF fiber fronthaul system, 20 carrier aggregation OFDM signals with total 2 GHz bandwidth are applied and are successfully demodulated. By applying different QAM level to different OFDM bands, we can achieve raw data rate under FEC threshold to support 10 Gb/s and 9.4 Gb/s in BtB scheme as well as 7.8 Gb/s and 7.4 Gb/s over 25-km fiber transmission with 0- and 180-degree IPPS respectively (Figure 3.5c). The

corresponding QAM level among each OFDM bands and electrical spectrum in the BtB scheme with 0-degree IPPS is also presented in Figure 3.5d. As we considering the 7% FEC overhead, 1/32 CP length, 10% training symbols, and 10% signal guard band, we can achieve a net data rate of 7.3 Gb/s in BtB and 5.7 Gb/s for over 25 km, showing the mm-Wave SSA-BF fiber fronthaul system with full FoV and self-tracking abilities for future mm-Wave enhanced mobile services. The measurements in Section 3.3.1.4 are based on electrical phase shifting and it shows a flat array factor enhancement with negligible SNR degradation over full-FoV and supports enhanced mobile data-rate carrier aggregation OFDM over 25-km fiber transmission without considering FoV coverage of the antenna. However, in the practical scenarios, the FoV coverage of the entire fiber-wireless SSA-BF system is also limited by the antenna design. In following section 3.3.2, a proof-of-concept broadband wide-FoV antenna is presented.

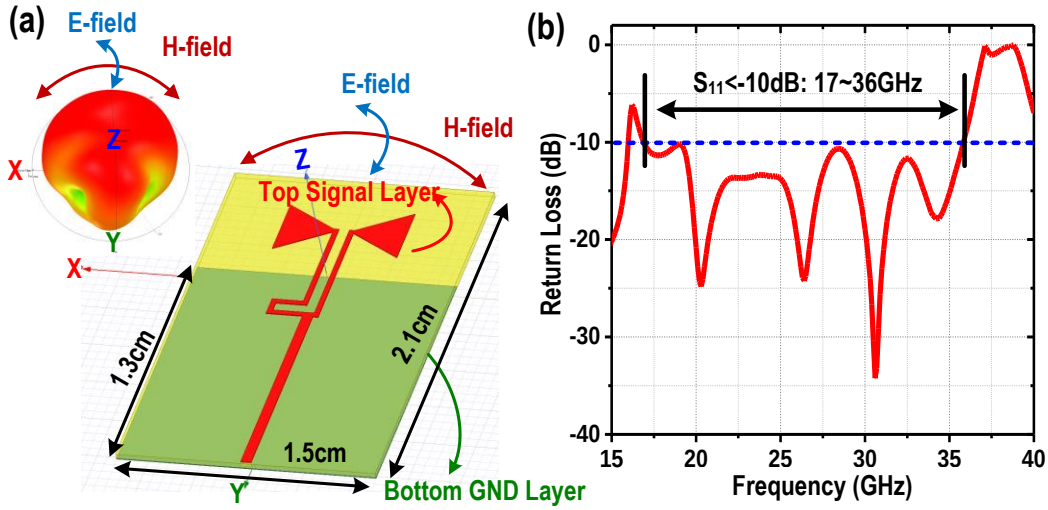

Figure 3.6 – (a) 3D EM HFSS model and radiation pattern of the proposed bow-tie antenna. (b) Measured input matching S11 of the antenna.

3.3.2 Broadband Wide-FoV Antenna Design

To extend FoV and broadband coverage, a bow-tie dipole antenna fabricated on two-layer Rogers RO40350 with 10mil height and 1oz cooper thickness is proposed to support a mm-Wave low-loss antenna design (Figure 3.6). The top signal layer is first designed via differential feeding lines with differential impedance ~100Ω. One of feeding line is banding/meandering to create out-of-phase 180° phase difference and they are then combined as one input single-end 50Ω feeding transmission line (Figure 3.6a). On the other hand, the bottom copper layer is served as PEC plane and designed as a finite ground to create extremely broadside FoV coverage and multi-resonance broadband frequency response. The 3D EM simulation of the broadside radiation at 28GHz and the antenna are shown in Figure 3.6a with ground size of 1.5cm×1.3cm and entire antenna area of 1.5cm×2.1cm. Measured input matching S_{11} < -10dB is from 17GHz to 36GHz, supporting wideband multi-5G standard communication (Figure 3.6b).

Then, the single-element antenna and the four-element antenna array are connected with southwest connectors for far-field radiation test (Figure 3.7). Four meandering transmission line traces in the four-element antenna array are applied for equal phase distribution for the four inputs and the area of the array is 2.1cm×5.5cm (Figure 3.7b). In the single-element antenna, the antenna gain patterns are measured with a peak antenna gain 2dBi and wide 3-dB beamwidth FoV = ± 80° coverage (total 160° incidence) on both E- and H-field, showing a state-of-the-art broadside performance. Note that the overall array gain pattern of the fiber-wireless system is a product of the antenna gain of each element and the beamforming array factor. Since the proposed SSA-BF generate near-ideal autonomous beamforming array factor over full-FoV, the far-field array gain pattern

measurement in Section 3.4 of the entire fiber-wireless SSA-BF system is limited by the FoV of the antenna.

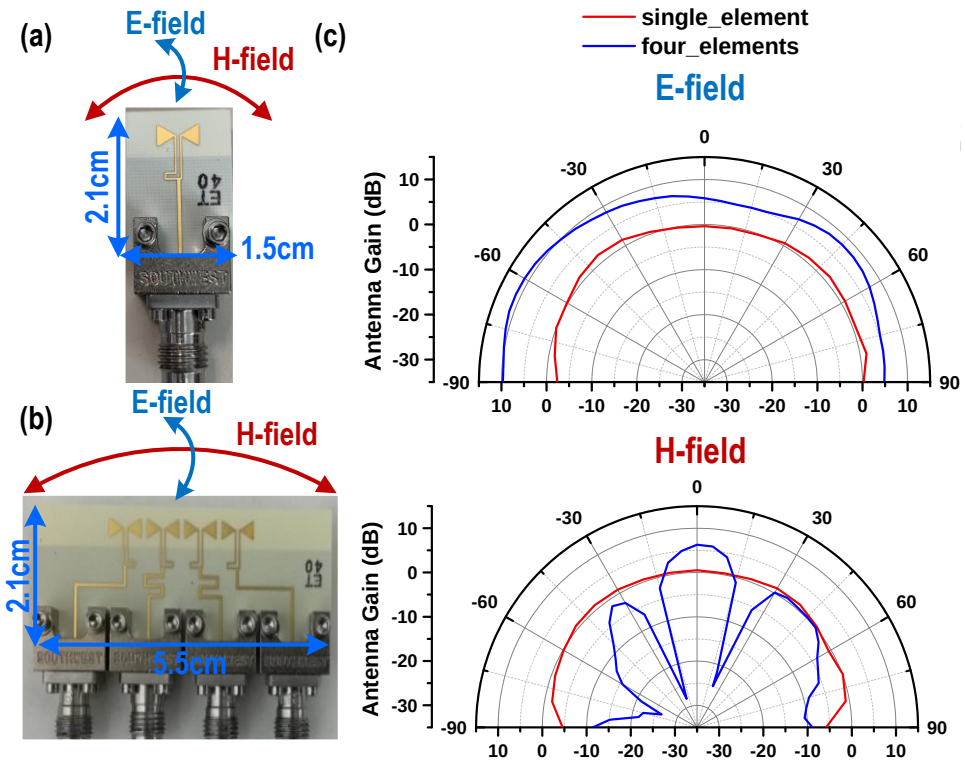

Figure 3.7 – Fabricated (a) single-element and (b) four-element antenna design. (c) Measured E- and H- field performance of the single-element and four-element antenna designs.

The far-field performance of four-element antenna array is then measured with an in-phase 4-to-1 power combiner without any phase tuning. Due to the IPPS of the four-element antenna arrays in H-field, the measured array gain peaks with 10×log4 = 6dB array factor enhancement compared to the single-element antenna and the 3-dB beamwidth FoV coverage is largely decreased from 160° to 20° (Figure 3.7c). With the proposed SSA-BF, the peak of the array gain real-time autonomously tracks and beamforms to the incoming signal over full-FoV with significant array factor improvement in the proposed fiber-wireless SSA-BF system (Section 3.4).

3.4 Far-Field Experimental Results

Figure 3.8a exhibits the experimental setup of far-field over-the-air measurement over 50 cm mm-Wave wireless transmission and 25 km fiber link. The 1Gbaud single carrier signal is generated via a 64 GSa/s AWG, and then up-converted to 28 GHz carrier frequency by mm-Wave mixers. A horn antenna with 25 dBi Gain is then employed for wireless signal delivery (Figure 3.8a).

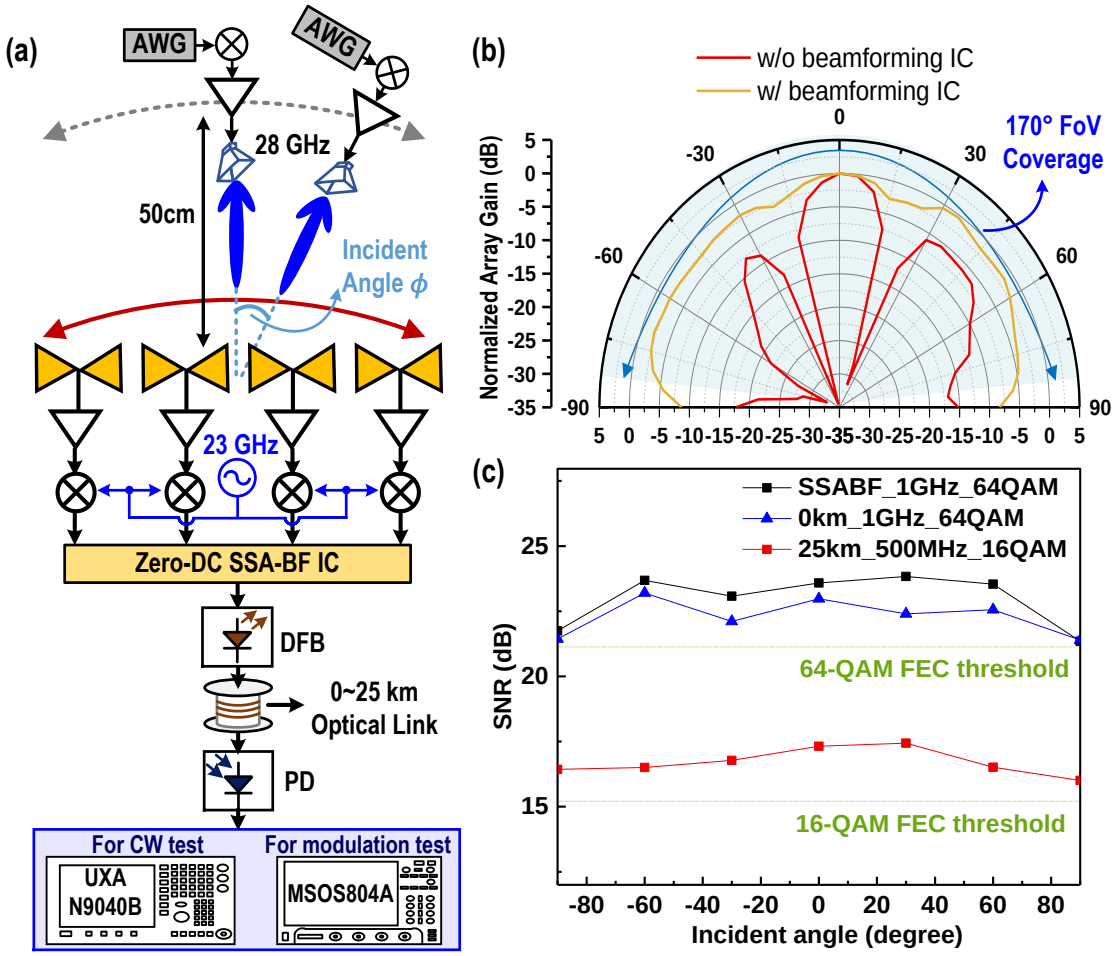

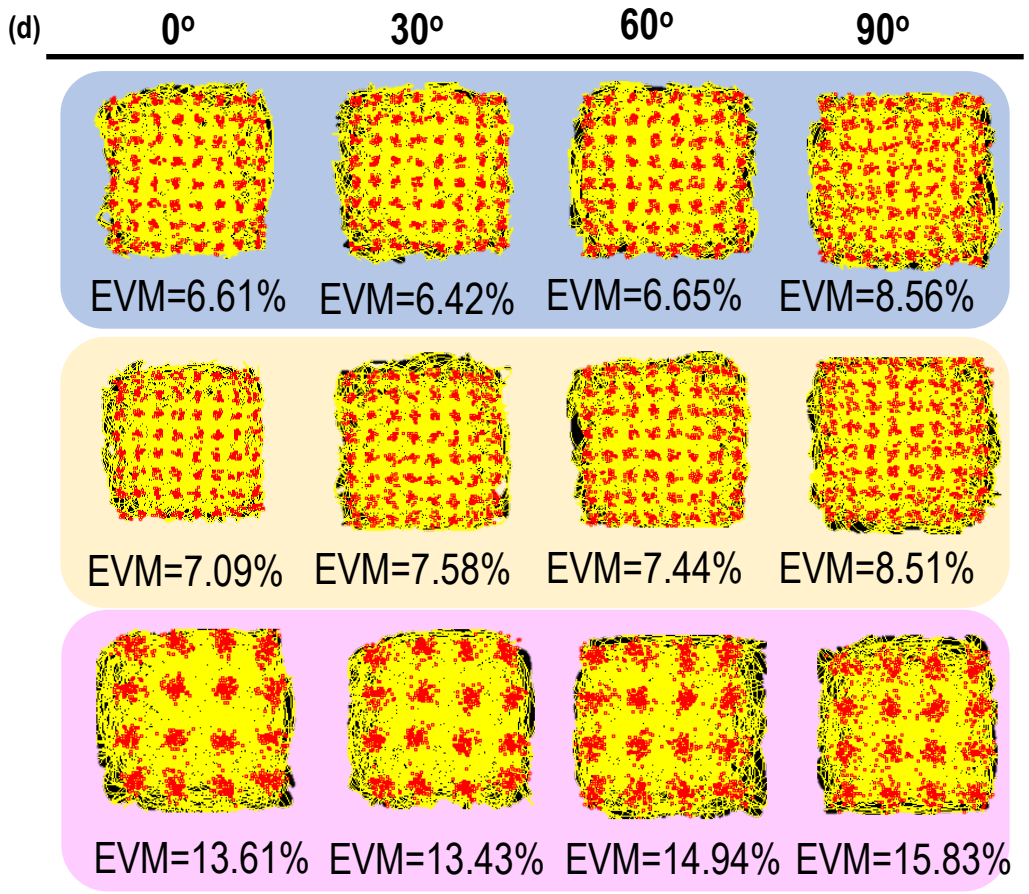

Figure 3.8 – (a) Far-field experimental setup for the proposed SSA-BF fiber-wireless system. (b) Far-field normalized antenna array gain pattern versus with incident angles. (c) Measured far-field SNR of SSA-BF only, SSA-BF with BtB fiber link, and SSA-BF with 25km fiber link over full-FoV. (d) Measured constellations and EVMs over full FoV in different case scenarios of SSA-BF only testing, b2b and 25-km transmission following the order from the top to bottom.

The wireless transmission distance is conducted under the far-field criteria, which is expressed as

$$R_f = 2D^2/\lambda, \tag{3.7}$$

where R_f, D, and λ are the radiating far-field distance, antenna diameter, and the RF signal wavelength respectively. To operate the wireless link at 28GHz, R_f needs to be > 42 cm. The far-field distance of 50 cm is chosen for over-the-air measurement and the received

signal could be approximately as plane waves with the progressive phase shifts across adjacent channels. After the four-element antenna array, the received signals are firstly amplified via the wideband LNAs with 25 dB gain, and then frequency is down-converted via 23-GHz LO mixers. The beamformer is operated at 5-GHz IF frequency to accommodate IF signal bandwidth and practical IC package design issue, which is especially easy for accurate phase matching, and lower propagation loss at RF frequency rather than at mm-Wave frequency. After initial one-time calibration between the antenna array and the SSA-BF system for phase and amplitude correction, measured array patterns of four-element fiber-wireless system over full FoV with/without the proposed SSA-BF are shown in Figure 3.8b.

The available reception angle of the proposed beamformer is evaluated via 28-GHz single-tone mm-Wave source as shown in Figure 3.8b. Without employing the proposed beamformer, power fading (< -30dBc), i.e. array factor null, incurs as the incident angle are near -30^{o} and 30^{o}. The result is similar as an ideal static four-element array factor without self-steering. On the other hand, with the proposed SSA-BF, the measured normalized array gain pattern better than 3-dB and 6-dB degradation is largely improved to cover wide FoV incidence = 136 ^{o} and 170 ^{o}, respectively, showing that the proposed SSA-BF effectively and autonomously traces the incident signal and beamforms the summing signal towards the desired direction over the extreme FoV.

Then, the modulated beamforming signal from the proposed SSA-BF is launched into a 10 GHz direct-modulated laser as electrical-optical conversion for optical signal delivery over 25 km fiber link. Then, a commercial 10-GHz PD is employed to conduct the opto-electrical down conversion with -0.6 dBm received optical power. After signal is analog-

to-digital converted via an 8-GHz, 20 GSa/s RTS, it is decoded by Keysight Vector Signal Analyzer with 0.035 filter roll-off and FIR equalizer (Figure 3.8a). Figure 3.8c shows the received SNR with over-the-air measurement coverage over the full FoV incidence. The black curve represents the SSA-BF only testing without the optical components and it shows best received performance with stabile SNR of near 24 dB in most of the cases, and a 3-dB SNR drop at the end-fire angles (incidence = ± 90°) is observed. As the beamformed signal passing through the optical channel, additional noises and signal losses slightly degrades the received SNR as the blue curve in Figure 3.8c. Note that the SNR at the end-fire angle is mainly dominated by the SSA-BF loop gain performance and the limited antenna FoV, and the measured corresponding demodulated EVM performance are similar at end-fire angles in both SSA-BF only testing and BtB transmission scheme. While, after 25-km fiber link, the received SNR is further reduced by about 5 dB and thus the available QAM level is declined to 16 QAM, which can be improved by applying a PD with a higher received sensitivity or adopting IF LNAs before the RTS. *To the best of our knowledge, this is a first-ever fiber-wireless SSA-BF system to achieve the state-of-the-art wideband 6 Gb/s 64-QAM single carrier with EVM above the FEC threshold in an optical system over full-FoV ± 90^{o} incidence (Table 3.1).*

Table 3.1 – Comparison with State-of-the-Art Optical Beamformer and Fiber-Wireless System

	M. Michele Sisto *OFC'10*	T. Mengual. *OFC'08*	C. G. H. RoeloffzenJ *OFC'15*	N.M. Tessema *MPW'17*	H. Lu, *OFC'18*	A.M. Trinidad *OFC'18*	K. Furuya *IEICE'17*	V. C. Duarte *OFC'18*	This Work
Element No.	4	8	16	4	4	4	2x4	4	**4**
Frequency (GHz)	N/A	7.5-8.5	11.72	20	22-25	20	60	28	**28**
Topology	Thermal or stretching controlled FBG	Optical TDD with spatial light modulator	Thermal controlled phase shifter	Thermal controlled phase shifter	Optical comb lines with SCM	single optical ring resonator for phase shifting	Optical variable delay lines	True time delay phase tuner and DSP	**True time DLL with all-passive nonlinear loop**
Beamforming	Open-Loop	Open-Loop	Open-Loop	Open-Loop	Open-Loop	Open-Loop	Open-Loop	Closed-loop	**Closed-loop**
Electrical Phase Shifting Incident FoV Coverage	-60˚~30˚	N/A	N/A	N/A	-48˚~35˚	N/A	N/A	N/A	**Full-FoV -90˚~90˚**
Radio Over Fiber (Distance)	N/A	Yes (N/A)	N/A	N/A	N/A	Yes (85 cm)	Yes (35 cm)	N/A	**Yes (50 cm)**
Antenna Array Far-Field Incident FoV Coverage	N/A	20˚	N/A	N/A	N/A	45˚	40˚	N/A	**3-dB AG Degradation*: -68˚~68˚ 6-dB AG Degradation*: -85˚~85˚**
Response Time	N/A	N/A	N/A	N/A	N/A	N/A	N/A	~10s	**< 0.003s**
Modulation Scheme	N/A	N/A	N/A	32-QAM	16-QAM	16-QAM	QPSK	QPSK	**64-QAM**
EVM	N/A	N/A	N/A	9.61 Gb/s	8 Gb/s	2.8 Gb/s	3.5 Gb/s	1 Gb/s	**6 Gb/s: 64-QAM 10.08 Gb/s: bit-loading**

AG Degradation* : Normalized array gain degradation

CHAPTER 4. A FULL-FOV AUTONOMOUS HYBRID BEAMFORMER ARRAY WITH UNKNOWN BLOCKERS REJECTION AND SIGNALS TRACKING FOR LOW-LATENCY 5G MM-WAVE LINKS

This Chapter demonstrates an 8-element multiple-input-multiple-output (MIMO) hybrid beam-forming receiver array with autonomous millimeter-wave (mm-Wave)/RF frontend beam-forming and digital baseband BF. It enables autonomous dynamic suppression of unknown blockers and BF on unknown desired signals, without knowing their carrier frequency, angle-of-arrival (AoA), and modulation scheme as a priori. After autonomous cancellation of an in-band/co-channel wideband-modulated blocker, a wideband-modulated desired signal is measured with high SNR, achieving -25.7 dB EVM for 6Gb/s 64QAM and -31.8 dB EVM for 1.6Gb/s 256QAM. Without baseband DSP beam-searching, the closed-loop mm-Wave/RF frontend beam-former realizes < 1 μs rapid response per stage, 100-to-1000× faster than existing mm-Wave analog/digital beam-formers with DSP beam-searching. The 8-element MIMO receiver array covers a wide frequency range (23-30 GHz) and the full Field-of-View (FoV) to address future low-latency applications of practical 5G MIMO systems. To the best of the authors' knowledge, this is the first MIMO receiver array enabling autonomous wideband modulated 64-/256-QAM blocker rejection and desired signal BF with μs response time.

4.1 Introduction

Mm-Wave MIMO, such as 5G new radio (NR) transceivers [38]-[66], often employ a large number of array elements to boost the array gain and spatial selectivity, resulting in narrow beamwidth that substantially complicates the transmitter-receiver (TX-RX) alignment. Unlike existing mm-Wave applications that are mostly in "static" settings (e.g., wireless HDTV transmission), many future mm-Wave links need to operate in highly "dynamic" environments, such as wireless AR/VR and vehicle-/drone-/machine-based communication, necessitating rapid and precise beam-forming/-tracking to ensure high link reliability and extremely low latency, e.g., 1ms response time for 5G links. Future dense mm-Wave link deployment will result in congested/contested EM environment, and thus spatially tracking/rejecting "unknown blockers", i.e., unknown carrier frequency, angle-of-arrival (AoA), or modulation, becomes essential.

Conventional RF/analog frontend beamformers (BFs) support limited number of beams and are open-loop systems per se, requiring baseband MUSIC-based computation to generate phase/amplitude control signals [39][47][50]. Digital beam-forming enables concurrent multi-beam operations [38][65][72][73], yet fully relies on baseband beam computation. A state-of-the-art digital beam-forming mm-Wave link in an almost idealistic environment requires tens of milliseconds beam searching time and thus, cannot meet <1ms 5G latency requirement [38]. Self-steering arrays (SSA) perform closed-loop and rapid BF at the mm-Wave/RF/IF frontends without DSP. However, existing SSAs mostly rely on PLL- or coupled-oscillator-based architectures [7]-[9] that are inherently narrowband with limited Field-of-View (FoV) and cannot support multi-beam operations. The fundamental inter-element incident angle phase shifts range for coupled oscillator array (COA) is ± 30°

[9] rather than full-FoV incident angle range of ± 90°. Although the FoV of the COA can use multiplier (doubler or quadrupler) [7] for phase shifts range extension to cover full FoV, narrowband and nonlinearities make it difficult to operate when signals have wideband modulation schemes. Notably most existing SSAs will lock to the blockers and fail to function in complex EM environments. In parallel, although array-based spatial blocker filtering has been extensively studied [74]-[76], most of them are open-loop systems, which rely on prior knowledge of the blockers or baseband computation to generate spatial-notch control signals.

To address these challenges in dynamic and mobile mm-Wave 5G applications, we present a scalable full-FoV MIMO receiver array with hybrid beam-forming by using closed-loop multi-stage cascadable DSP-free mm-Wave/RF beam-formers and digital beam-forming. The closed-loop BFs autonomously create spatial notches on multiple in-band blockers and perform BF on the desired signals with μs dynamic response time. The array rejects wideband in-band blocker and receives desired signal with 6Gb/s 64QAM and 1.6Gb/s 256QAM over full FoV in measurements.

This Chapter is organized as follows. Section 4.2 presents the hybrid autonomous BF system architecture. The operation principle and implementation details of a 23-30 GHz 8-element SSA front-end BF prototype are demonstrated in Section 4.3. Section 4.4 shows the measurements and a performance comparison with various reported MIMO RX arrays.

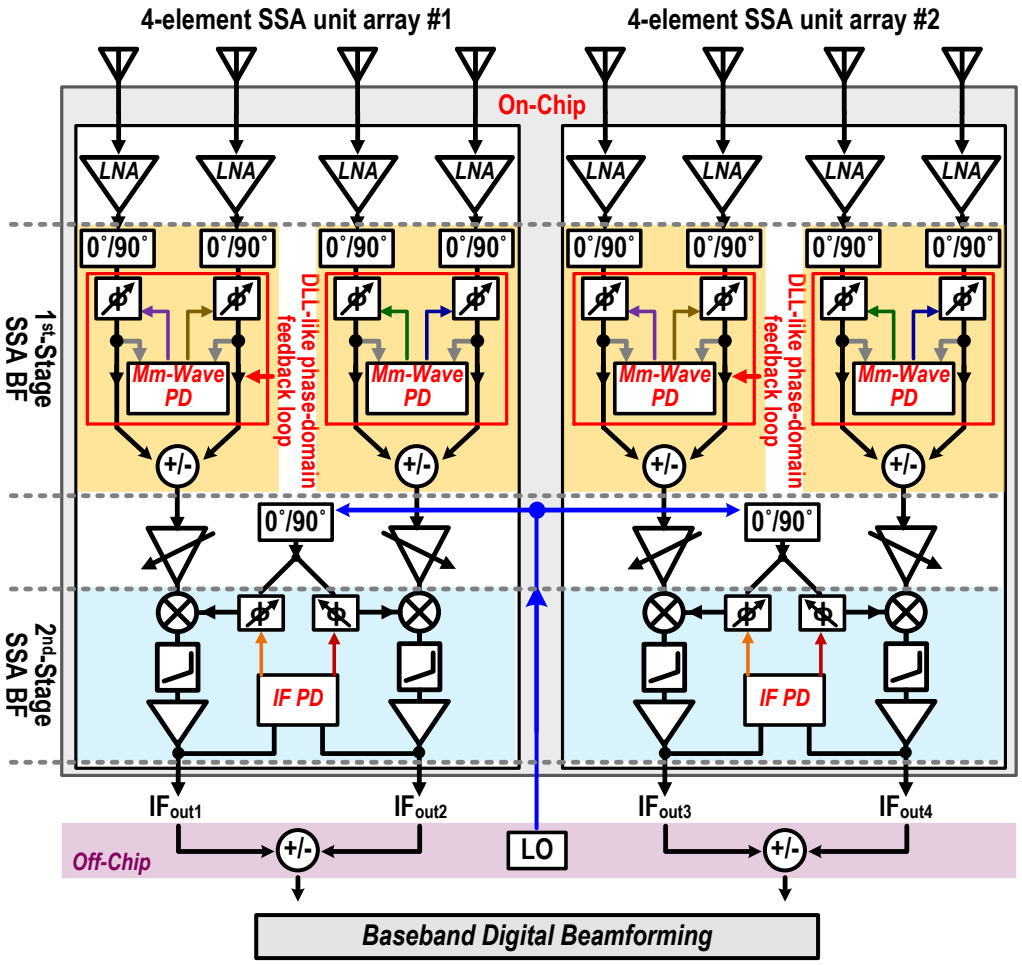

Figure 4.1 – System architecture of the 8-element full-FoV MIMO RX array.

4.2 Hybrid BF Receiver with Closed-Loop Multi-Stage Self-Steering Array

4.2.1 System Architecture

Future dynamic wireless applications necessitate low-latency frontend hardware and leave most latency budget for the software layer. The proposed SSA front-end RX BF architecture is calibration- and DSP-free via closed-loop BF (Figure 4.1). Moreover, the negative feedback loop operates in a delay-lock-loop-like (DLL-like) fashion in the phase domain with intrinsic broad bandwidth and full FoV [16][67]. The negative feedback loops

are also cascadable with multiple stages to handle multiple beams (Figure 4.1). It supports autonomous unknown blockers rejection and unknown desired signals alignment, while the digital BF provides further beam alignment or processing.

A proof-of-concept 8-element RX array chip is demonstrated with two parallel 4-element SSA unit arrays (Figure 4.1). Multiple chips can further form a scalable massive MIMO. Each 4-element SSA unit array is composed of front-end mm-Wave wideband low-noised amplifiers (LNAs), two parallel 1st-stage mm-Wave SSA BFs, and one 2nd-stage IF SSA BF (Figure 4.1). The 1st-stage SSA BF contains two mm-Wave wideband signal-path I/Q phase shifters (PS) and a mm-Wave power-aware nonlinear phase detector (PD). An on-chip combiner/subtractor performs beam-forming/notching for the 1st-stage SSA BFs. The 2nd-stage SSA BF includes two down-conversion mixers, IF amplifiers, and IF PD. At the 2nd stage, two LO-path I/Q PS are adopted to avoid phase-dependent amplitude variations in RF- or IF-path PS. An off-chip combiner /subtractor is then applied after the 2nd-stage SSA BF.

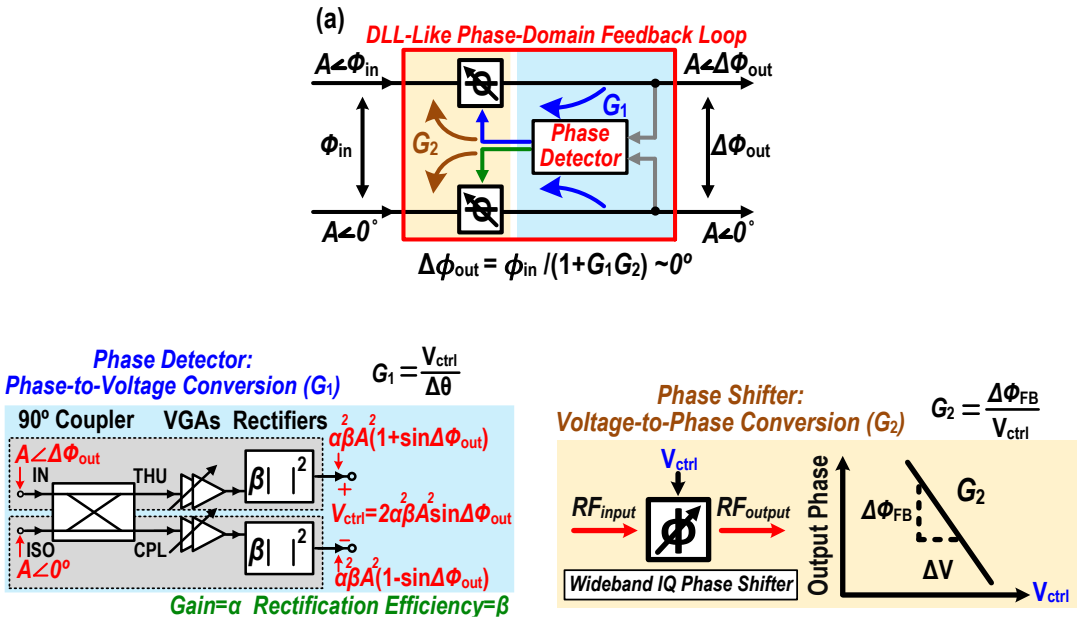

(b)

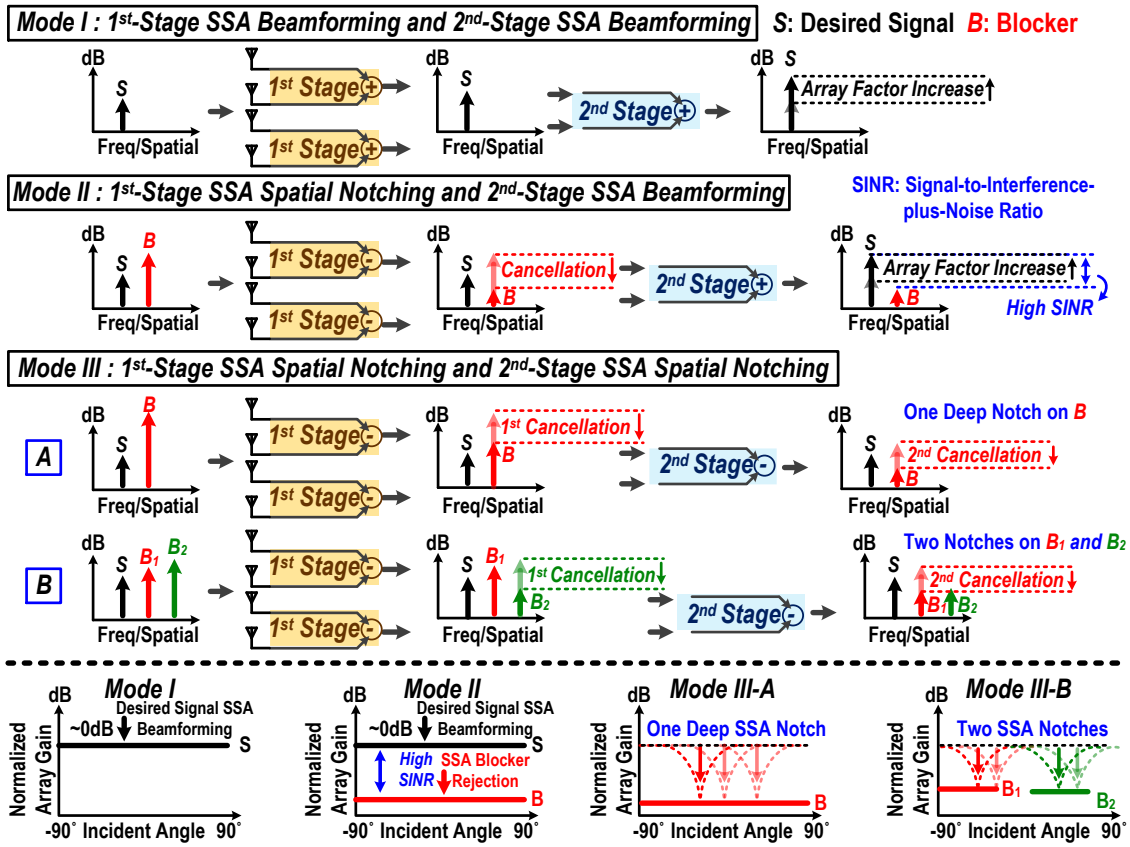

Figure 4.2 – (a) The operation principle of the SSA front-end BF as well as simulated residual phase difference. (b) Various operation modes of the RX array by reconfiguring the output combiners or subtractors in the 1st- and 2nd-stage SSA front-end BF stages.

4.2.2 Operation of the DLL-Like SSA BF

The DLL-like operation of the SSA BF stages is explained (Figure 4.2a). When the incoming signals are injected to the receiver with an incident angle θ, the received signals in the adjacent two paths exhibit progressive phase $\phi_{in}= \pi\sin\theta$ for a uniform λ/2 array. The phase shift is then detected by the PD and generates corresponding differential DC control voltages. This forms the phase-to-voltage conversion gain G_1. The DC control voltages are then fed back as the control voltages for the I/Q PS with voltage-to-phase conversion gain

G_2. This forms a negative-feedback closed-loop operation in the phase domain with a wideband nature and an overall loop gain of G_1G_2. The output residual phase difference $\Delta\phi_{out}$ can be expressed as

$$\Delta\phi_{out} = \phi_{in}/(1+ G_1G_2) = \pi\sin\theta /(1+ G_1G_2). \quad (4.1)$$

The negative feedback loop behaves like a DLL to autonomously align the phase of the two adjacent paths and minimize $\Delta\phi_{out}$ at their outputs. If the combiner is used at the outputs, it can constructively beamform the desired signal. If an unwanted strong blocker is present, the subtractor is chosen to destructively suppress the blocker by spatial notching. Note that the PD is implemented as a nonlinear power-aware device. If multiple signals are received concurrently, the signal with the highest power dominates the PD output due to its nonlinear rectification operation, so that each BF stage only responds to its strongest received signal, e.g., the dominant blocker. Moreover, variable gain amplifiers (VGAs) are used in the feedback loop to ensure a large loop gain and achieve a near-zero path-to-path phase error $\Delta\phi_{out}$ even when the signals are at end-fire incidence $\theta = \pm 90^{\circ}$. Large nonlinear loop gain G_1G_2 is exploited to achieve full FoV coverage without loop gain degradation over FoV [67]. Unlike conventional coupled PLL- or oscillator-based SSA, our DLL-like SSA BF does not require resonators and is intrinsically broadband [67]. Furthermore, our SSA BFs can be cascaded to process multiple concurrent blockers and desired signals [40].

4.2.3 Receiver Operation Modes

Figure 4.2b shows the various operation modes supported by the 2-stage mm-wave/IF SSA BFs to accommodate different receiving scenarios. In mode I, the two SSA BF stages both use combiners at their outputs, and the RX array operates as an 8-element SSA per

chip that autonomously tracks and forms the beam toward one desired signal over full FoV. In mode II, the 1st-stage SSA BF stage uses subtractor and the 2nd-stage SSA BF stage uses combiner. The receiver first creates a spatial notch to autonomously reject one unknown in-band strong blocker, and further enhances one desired signal with self-steering BF, boosting its SINR. Notably, the power-aware PD ensures that the 1st-stage SSA BF only responds to the strong blocker and spatially cancels the blocker rather than the desired signal. In mode III, when both the 1st- and 2nd-stage SSA BF stage use subtractors, the RX can either suppress one strong in-band blocker twice to form a deep spatial notch (Mode III-A) or it can create two independent spatial notches to reject two different in-band blockers (Mode III-B). For operation mode II and III, deep spatial notch largely suppresses the in-band blockers, relaxes the following dynamic range requirement (e.g., ADC), and enables subsequent baseband digital BF. Most importantly, for all the aforementioned operation modes, except the one-step DSP demodulation for blocker/signal classification, the SSA front-end BF does not require DSP for beam scanning or computation and signal/blocker are autonomously tracked for beamforming /rejection, drastically accelerating the beamforming.

4.3 Circuit Implementation and Analysis

To demonstrate the proposed mm-Wave hybrid beam-forming for full-FoV autonomous unknown signal beam-forming and blocker rejection, an 8-element proof-of-concept design for 23-30 GHz is implemented in a 130nm SiGe process [40]. Signals through each two adjacent elements are sampled and processed with autonomous phase alignment via 1^{st}-/2^{nd}-stage SSA BFs for multiple signals BF or blockers rejection. Simplicity of the scaling for the proposed architecture can easily facilitate a large-scale

receiver array. Detailed circuit implementations for the mm-Wave broadband LNAs and the SSA BFs with the voltage-to-phase conversion G_1 via power-aware PDs as well as phase-to-voltage conversion G_2 by PSs are shown and analyzed.

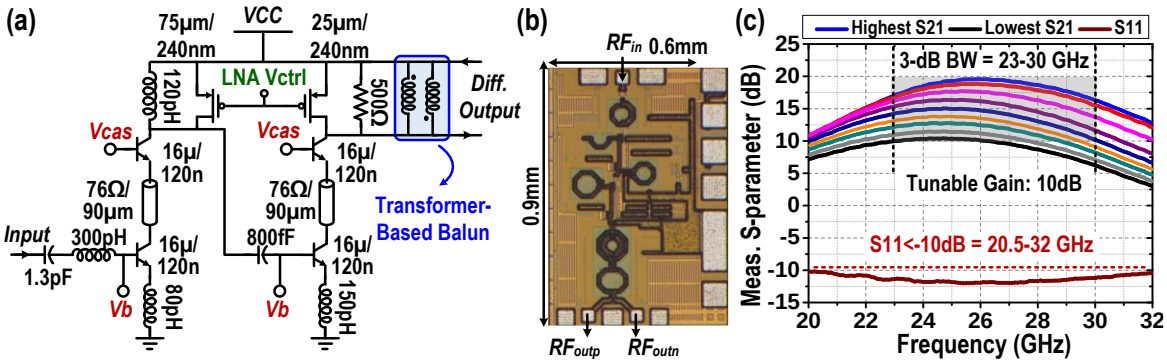

Figure 4.3 – (a) Schematic, (b) chip photo, and (c) measurements of the mm-Wave 2-stage LNA.

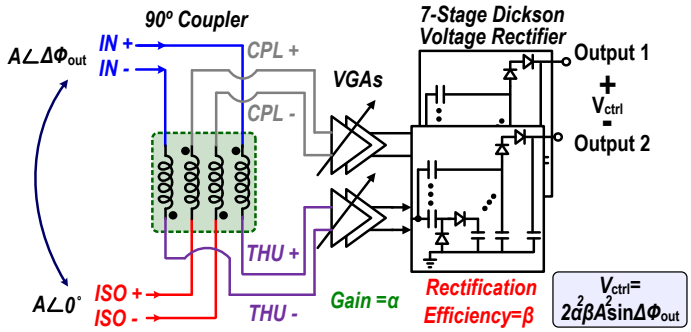

Figure 4.4 – Schematic of the power-aware phase detector.

4.3.1 Front-End Mm-Wave Broadband LNA

The LNA is designed with resonant loads in two stages at different frequencies to provide broadband performance and serve as a wideband frontend (Figure 4.3a). The PMOS switch at the LNA loads is used for variable gain control for accommodating different linearity scenarios when the MIMO system operates in complicated EM

environment. The total size of the LNA is 0.54 mm2 (Figure 4.3b). The measured performance for the LNA-only test structure is shown in Figure 4.3c. It achieves S11 < -10 dB from 20.5-32 GHz and peak gain 19.5 dB with 10 dB tunable gain from 23-30 GHz.

4.3.2 Phase-to-Voltage Conversion G_1 Circuit

The simplified block diagram of the phase-to-voltage convertor is shown in Figure 4.4. It consists of a compact differential 90˚ coupler [77], VGAs, and a 7-stage Dickson voltage rectifier. The differential 90˚ coupler is built using a transformer-based poly-phased network for wideband low-loss IQ generation [77]. When the two signals in the adjacent path exhibit phase-shifts and are concurrently fed to the input (IN) and isolation (ISO) ports of the 90° coupler, outputs from the through (THU) and coupled (CPL) ports are fed to the VGAs followed by the multi-stage Dickson voltage rectifier (Figure 4.4). The VGAs are used to maximize the driving voltage amplitude for the Dickson voltage rectifiers with higher nonlinear rectification efficiency. The boosted nonlinear loop gain is explored to be extremely large even at end-fire incidence without significant degradations. The outputs of the rectifiers are then used as the differential control voltages Vctrl for the wideband continuous-tuning I/Q voltage-controlled PS to generate the compensation phase ϕ_{FB}. The large-signal behaviour of the phase-to-voltage converter can be analyzed by applying two RF incident signals with the same amplitude A but at a phase difference $\Delta\phi$out into the IN and ISO ports of the 90° coupler. The voltage amplitudes of the output RF signals at the THU and CPL ports are amplified by the gain α. Then, the amplified output voltages are further converted to a differential DC voltage Vctrl by the rectifiers with the rectification efficiency β. Assume that the two matched rectifiers are square-law

devices, the differential feedback DC output voltage signal V_{ctrl} of the two rectifiers is obtained as [67]

$$V_{\text{ctrl}} = V_{\text{DCout1}} - V_{\text{DCout2}} = 2\alpha^2\beta A^2 \sin \Delta\phi_{\text{out}}. \quad (4.2)$$

The large-signal phase-to-voltage conversion gain G_1 can be further calculated as [67]

$$G_1 = V_{\text{ctrl}}/\Delta\phi_{\text{out}} = 2\alpha^2\beta A^2 \sin \Delta\phi_{\text{out}}/\Delta\phi_{\text{out}}. \quad (4.3)$$

Two-stage VGA is used to achieve a high gain α and maximize the phase-to-voltage conversion gain G_1. The differential DC outputs of the Dickson rectifiers are directly connected to the differential gates of the following DC amplifier. The output loads of the rectifiers are high impedance (~MΩ) to generate a large DC output voltage. Notably, unlike conventional energy harvester designs, the rectifiers are optimized for the conversion efficiency between RF power and DC voltage rather than between RF power and DC power. By combining these techniques, the proposed rectification scheme can properly operate with a large phase-to-voltage conversion gain G_1 (overall > 50, linear scale) over the full-FoV. The proposed phase-to-voltage convertor serves as full-FoV PD with a high detection sensitivity due to high active conversion gain. A sufficient loop gain G_1G_2 is provided and its value is maintained even at incidence edge (± 90˚) of FoV [67]. The simulated SSA BFs performance for signal self-steering/autonomous blocker rejection versus the loop gain G_1G_2 will be presented and discussed in Section 4.3.4.

On the other hand, reliability of the phase-to-voltage converter is also analyzed. Assume that there is an amplitude mismatch ε with ε < 1 and a phase error θ_{error} between the THU

and CPL ports of the 90˚ coupler (Figure 4.5), the DC output voltages of the two rectifiers are

$$V_{\text{DCout1, mismatch}} = \beta \left| \frac{\alpha A}{\sqrt{2}} [1 - j(1-\varepsilon) e^{j(\theta_{\text{error}} + \Delta\phi_{\text{out}})}] \right|^2$$

$$= \frac{\alpha^2 \beta A^2}{2} [2 + 2(1-\varepsilon)\sin(\theta_{\text{error}} + \Delta\phi_{\text{out}}) + (1-\varepsilon)^2], \text{ and } V_{\text{DCout2, mismatch}}$$

$$= \beta \left| \frac{\alpha A}{\sqrt{2}} [e^{j(\Delta\phi_{\text{out}})} - j(1-\varepsilon) e^{j(\theta_{\text{error}})}] \right|^2$$

$$= \frac{\alpha^2 \beta A^2}{2} [2 + 2(1-\varepsilon)\sin(\theta_{\text{error}} - \Delta\phi_{\text{out}}) + (1-\varepsilon)^2]. \quad (4.4)$$

Then, the differential feedback voltage signal with the phase and amplitude mismatch $V_{\text{ctrl, mismatch}}$ is obtained as

$$V_{\text{ctrl, mismatch}} = V_{\text{DCout1, mismatch}} - V_{\text{DCout2, mismatch}}$$

$$= 2\alpha\beta^2 A^2 [(1-\varepsilon)\cos(\theta_{\text{error}})] \sin \Delta\phi_{\text{out}}. \quad (4.5)$$

Differential operation ensures that the common-mode errors are cancelled and the large-signal phase-to-voltage conversion gain due to the mismatch is further calculated as

$$G_{1, \text{mismatch}} = V_{\text{ctrl, mismatch}} / \Delta\phi_{\text{out}}$$

$$= 2\alpha\beta^2 A^2 [(1-\varepsilon)\cos(\theta_{\text{error}})] \sin \Delta\phi_{\text{out}} / \Delta\phi_{\text{out}}. \quad (4.6)$$

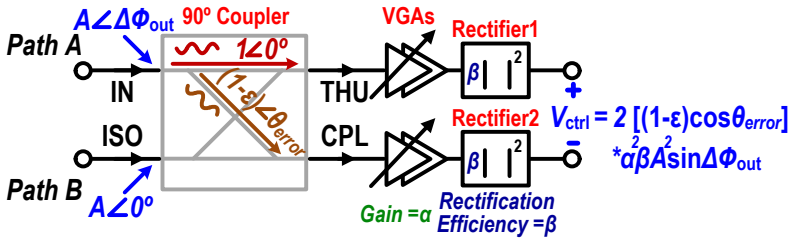

Figure 4.5 – Conceptual diagram for mismatch of the proposed PD analysis.

Compared to (4.2) and (4.3), the V_{ctrl} and G_1 value are decreased by the coefficient $(1-\varepsilon)\cos(\theta_{error})$, which is a linear number <1. Although the loop gain is degraded due to the mismatch, the nonlinear loop characteristic is not reformed and it still preserves full-FoV operation as long as the loop gain G_1G_2 is >>1 (Section 4.3.4). Moreover, for the proposed PD, the degradations from the phase and voltage domain are independent to each other. Unlike mixer-based PD operation, the amplitude/phase mismatch of the mixer may generate voltage-dependent phase error or phase-dependent voltage error due to the self-mixing and erroneously offsets the output DC control voltage. In summary, the proposed PD is robust to environmental variation and performs high-precision detection.

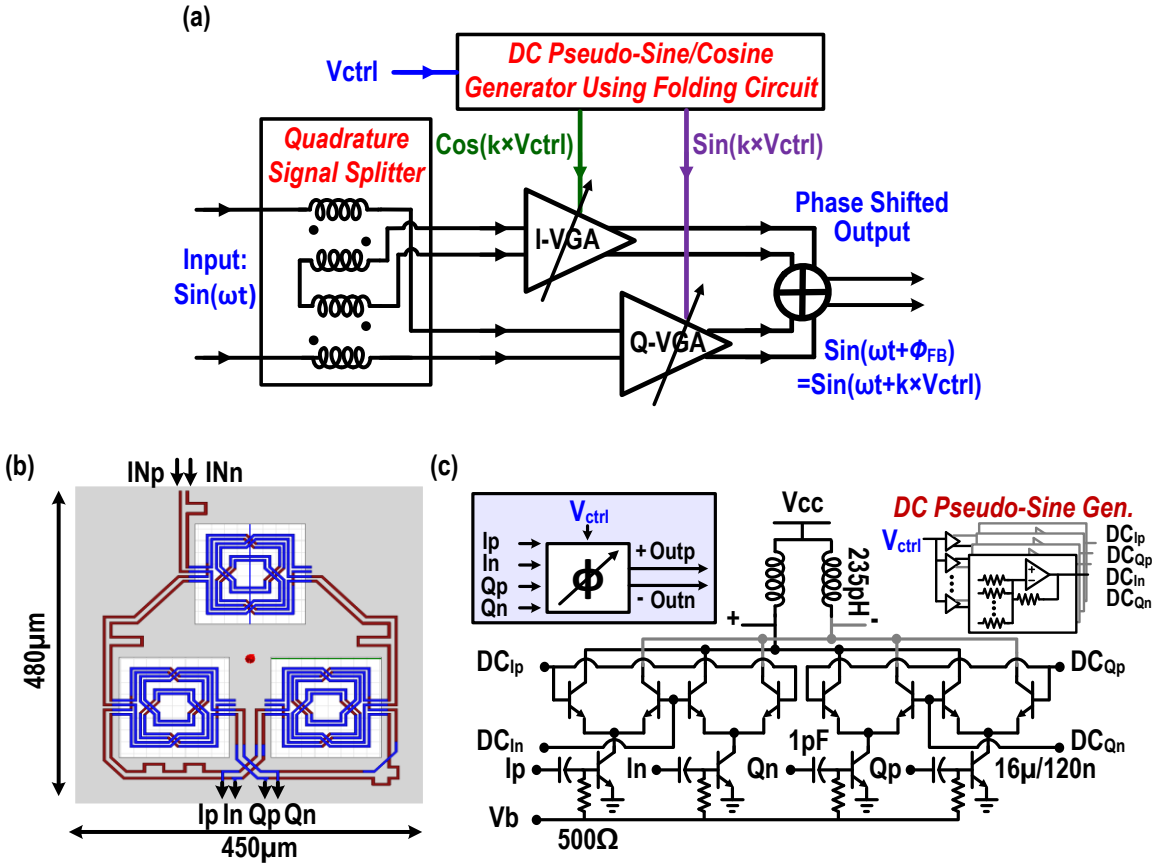

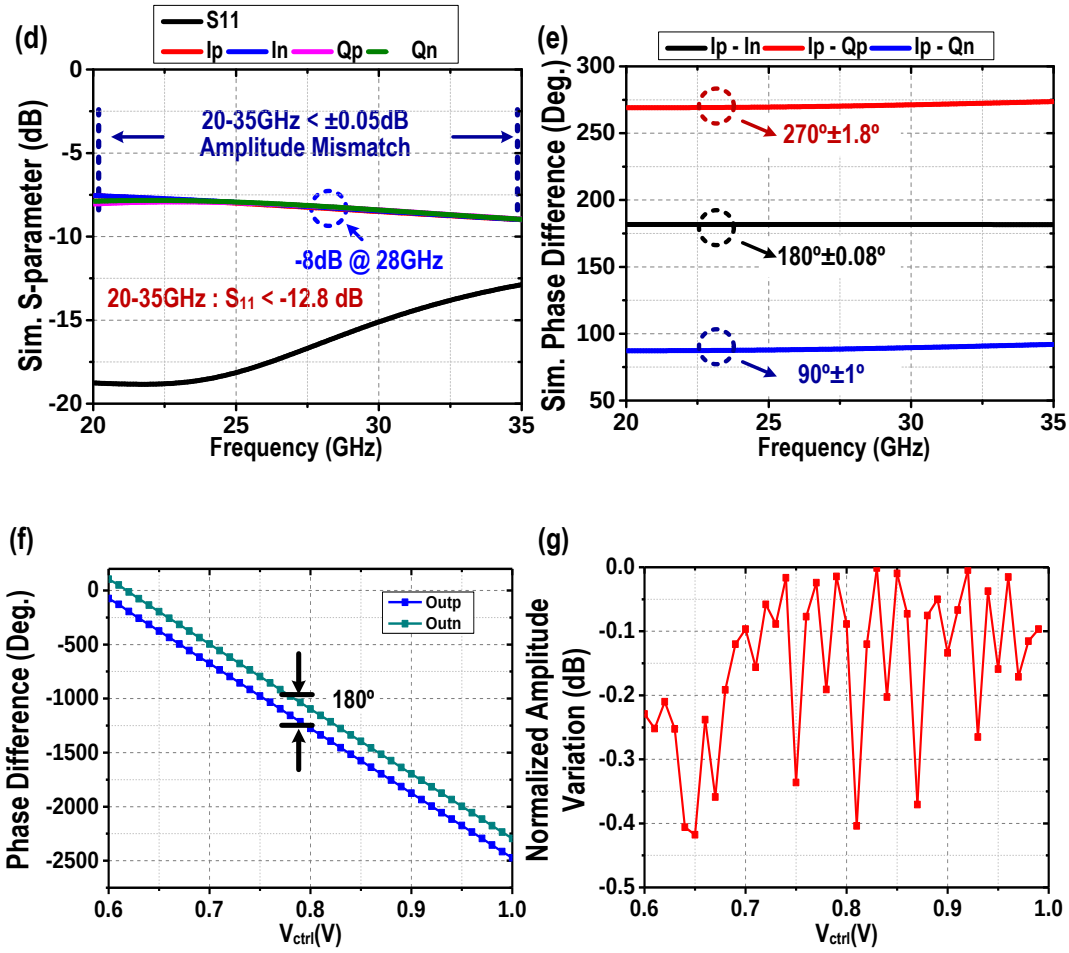

Figure 4.6 – (a) Block diagram of the mm-Wave IQ vector-modulator-based phase shifter. (b) 3D EM model of the mm-Wave transformer-based IQ network. (c) The wideband IQ phase shifter with built-in pseudo-sine generation circuits. (d) Simulated amplitude and (e) phase performance of the IQ. (f) Simulated output phase and (g) normalized amplitude variation and versus Vctrl of the wideband IQ phase shifters.

4.3.3 Voltage-to-Phase Conversion G_2 Circuit

The conceptual diagram and schematic for the wideband I/Q voltage-controlled continuous PS as the voltage-to-phase converter is shown in Figure 4.6a-6c. It consists of a two-stage transformer-based poly-phase network [77] and an analog multiplier with built-in DC pseudo-Sine/-Cosine generation [78] as a vector-modulator PS. Simulated mm-

Wave 2-stage transformer-based poly-phase network shows <±0.05 dB amplitude imbalance and <±1.8˚ I/Q phase mismatch over 20-35 GHz (Figure 4.6d-4.6e). It shows EM-simulated passive loss of only 2 dB at 28 GHz in addition to the 6 dB inherent loss due to 1-to-4 power splitting (overall 8 dB loss), supporting low-loss ultra-broadband IQ generation for mm-Wave/LO I/Q PS. Compared to the digital phase rotator [79][80], the proposed I/Q PS achieves wideband full-range continuous-tuning and only requires one analog control voltage for loop control simplicity. The V_{ctrl} from phase-to-voltage convertor is first sensed by the DC pseudo-Sine/-Cosine generation and then it generates corresponding compensation phase shift ϕ_{FB} and completes the negative feedback loop. The voltage-to-phase conversion gain is expressed as

$$G_2 = \phi_{\mathrm{FB}}/V_{\mathrm{ctrl}}. \tag{4.7}$$

Simulated amplitude and phase response of the PS is shown in Figure 4.6f-4.6g. It performs continuous phase shift > 2000˚ with only <0.4 dB amplitude variation, showing highly linear phase shifts with a negligible amplitude change. It achieves orthogonal controls between the phase and amplitude tuning, which is important for the beam-forming/steering [39]. The simulated voltage-to-phase conversion gain G_2 is 6.5°/mV at 28 GHz.

4.3.4 Loop Analysis of the SSA BFs

The phase-domain closed-loop performances of the SSA BFs, such as residual phase difference $\Delta\phi_{\mathrm{out}}$, the normalized array factor for signal BF, spatial notch for blocker cancellation, and response time, are next analyzed. First, the residual output phase difference $\Delta\phi_{\mathrm{out}}$ can be expressed as [67]

$$\Delta\phi_{\text{out}} = \pi\sin\theta\,/(1+G_1G_2)$$

$$= \pi\sin\theta\,/\,[1+\,(2\alpha^2\beta A^2\sin\Delta\phi_{\text{out}}/\Delta\phi_{\text{out}})G_2]. \tag{4.8}$$

G_1 varies with $\Delta\phi_{\text{out}}$ after the phase compensation, which shows the negative feedback loop is a nonlinear loop and (4.5) can be modified as

$$\Delta\phi_{\text{out}} + k\sin\Delta\phi_{\text{out}} = \pi\sin\theta, \tag{4.9}$$

where $k = 2\alpha^2\beta A^2$, which is the loop gain at incidence θ=0º when a boresight signal is received. k is in a quadratic relationship with the input mm-Wave/IF input amplitude A, showing that the loop response is a function of the input power. For a given incident angle θ of the received RF inputs, the residual phase error $\Delta\phi_{\text{out}}$ is calculated using (4.9), and the total loop gain is obtained as $G_1G_2 = (2\alpha^2\beta A^2\sin\Delta\phi_{\text{out}}/\Delta\phi_{\text{out}})G_2$. The large-signal loop gain peaks at θ = 0° and gradually decreases when the θ approaches ±90°. Because of its nonlinear bifurcation behavior, the power-aware feedback loop maintains its loop gain value for a given incidence θ within and even at ±90° with full-FoV operation as long as the k is >>1 [67].

The residual phase difference $\Delta\phi_{\text{out}}$, the normalized array factor for signal beam-forming, and spatial notch for blocker cancellation of the SSA BFs versus different loop gain G_1G_2 value at end-fire incidence θ = 90° are simulated in Figure 4.7a-4.7c. With the targeted loop gain > 300 (linear scale), residual phase difference $\Delta\phi_{\text{out}}$ is highly suppressed to < 0.6° (Figure 4.7a). For desired signal self-steering, the combiner is applied at the outputs of the adjacent paths. The normalized array factor is achieved > -1.2E-4 dB (~ 0 dB), achieving "ideal self-steering" over full FoV (Figure 4.7b). On the other hand, if

undesired strong signal/blocker is received, the outputs of the SSA BFs is followed by a subtractor to reject the signal. The notch filter for the blocker rejection has > 39.6 dB cancellation without any DSP calibration (Figure 4.7c). Although the practical phase/amplitude variation of the power-aware PD and the PS are not included in the simulated performances via (4.9), the non-ideal effects are measured and presented in Section 4.4. Most importantly, operating the proposed phase-domain nonlinear closed-loop with the large loop gain achieves the state-of-the-art full-FoV autonomous signal beam-forming and blocker rejection without down-time controls from the DSP.

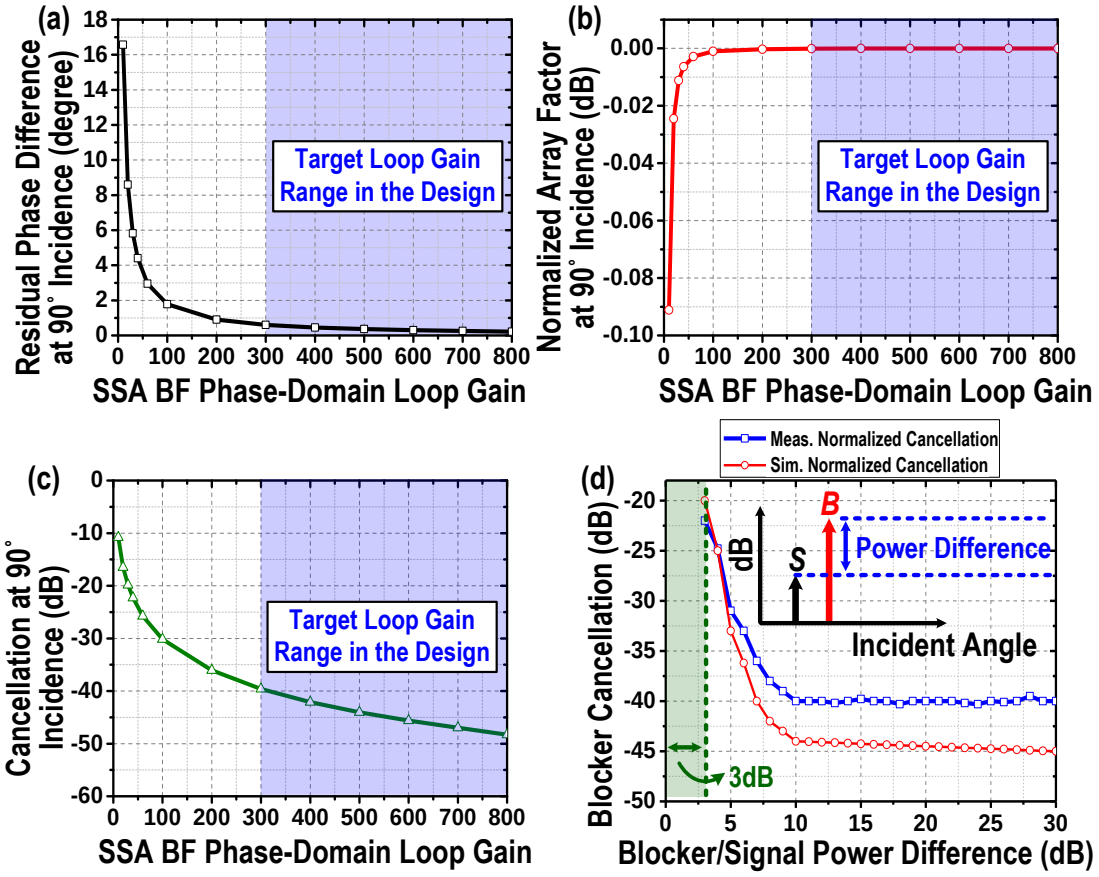

Figure 4.7 – Simulated (a) residual phase difference, (b) normalized array factor, and (c) blocker cancellation at end-fire incidence (90°) versus the SSA phase-domain loop gain for the two-input SSA beamformer. (d) Simulated and measured SSA-BF discrimination of concurrently received multi-tones.

The response time of the loop is mainly determined by the dominant pole that is created at the load of the phase-to-voltage converter. With at least 10000× smaller RC load than [67], the simulated instinctual response time for each SSA BF stage is < 0.5μs, enabling future low-latency mm-Wave applications. Additionally, the discrimination of the SSA-BF for concurrent received multi-tones is simulated and measured. When the two co-channel tones (blocker and signal) are concurrently injected, the power-aware PD can accurately respond to the blocker, not the desired signal, and achieve > 22 dB SSA blocker rejection, if the blocker/signal power difference is > 3 dB (Figure 4.7d). The detailed cascaded 2-sage SSA-BF measurements for various operation modes will be shown in Section 4.4.1.

4.4 Experimental Results

The proposed 8-element 23-30 GHz scalable SSA BFs RX array prototype is implemented in a 0.13µm SiGe BiCMOS process with a total chip size of 3.6mm×6mm (Figure 4.8) [48]. The measurement setup is shown in Figure 4.9. Multiple continuous-wave (CW)/modulated IF signals with programmable phase and amplitude in each channel are first generated by the Keysignt AWG M8195A. Then, they are up-converted to mm-Wave frequency by the external mixers, serving as the multiple signals/blockers which are concurrently injected to the RX array chip. The Keysight spectrum analyzer UXA is used for characterizing mm-Wave CW performance of the 1st-stage SSA BFs. The performance of the 2nd-stage IF SSA BFs, response time of the loop operation, and demodulation results are then captured by the Keysight oscilloscope MSOS804A.

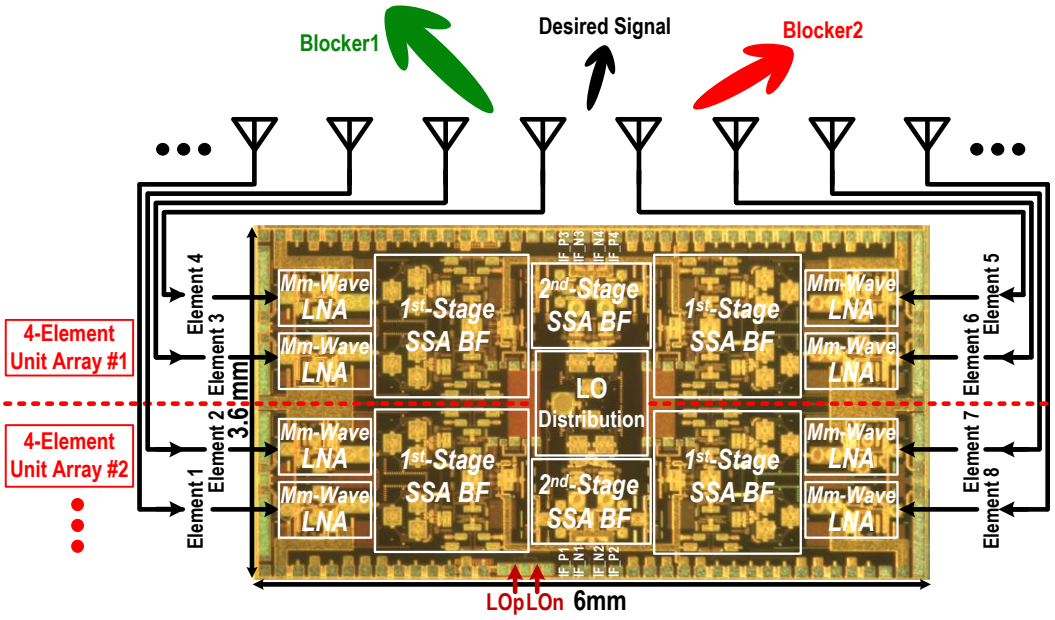

Figure 4.8 – Chip micrograph and its scalability for a large-scale phased array.

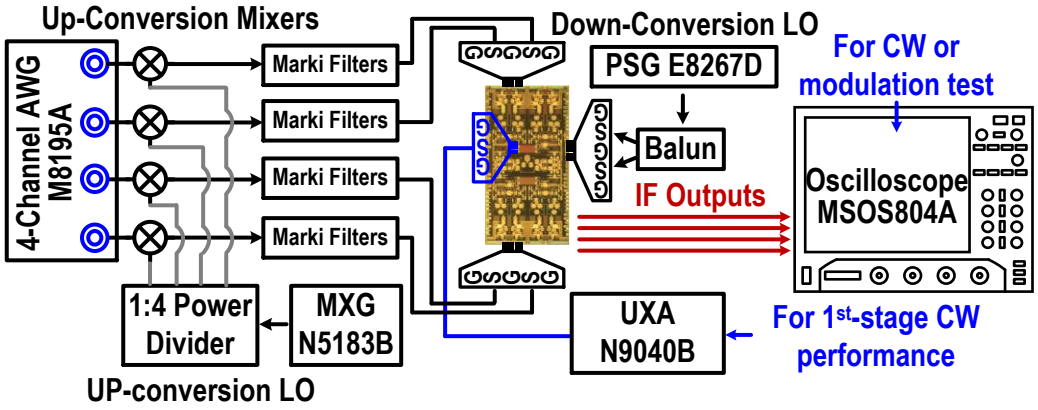

Figure 4.9 – Measurement setup.

4.4.1 CW Measurement

First, the CW performances of the 1st- and 2nd-stage SSA BFs are individually characterized (Figure 4.10a-4.10d). Over the full-FoV and a 23-30 GHz wide bandwidth, the 1st-stage mm-Wave SSA BF achieves an extremely flat normalized array factor >-0.6 dB for the desired signal beam-forming (using combiner) and a 20-41 dB spatial notch for

blocker rejection (using subtractor). Similarly, the 2nd-stage IF SSA BF also achieves a flat normalized array factor >-0.53 dB for desired signal beam-forming and a 21-36 dB spatial notch for blocker rejection, over full-FoV and wideband operation (0.1-4 GHz for IF). The full FoV and wideband coverage support autonomous beam-forming (or spatial cancellation) for unknown desired in-band signals (or unknown co-channel blockers) even with unknown carrier frequency, AoA, and modulation schemes, enabling fast signal management in the future complex EM environment.

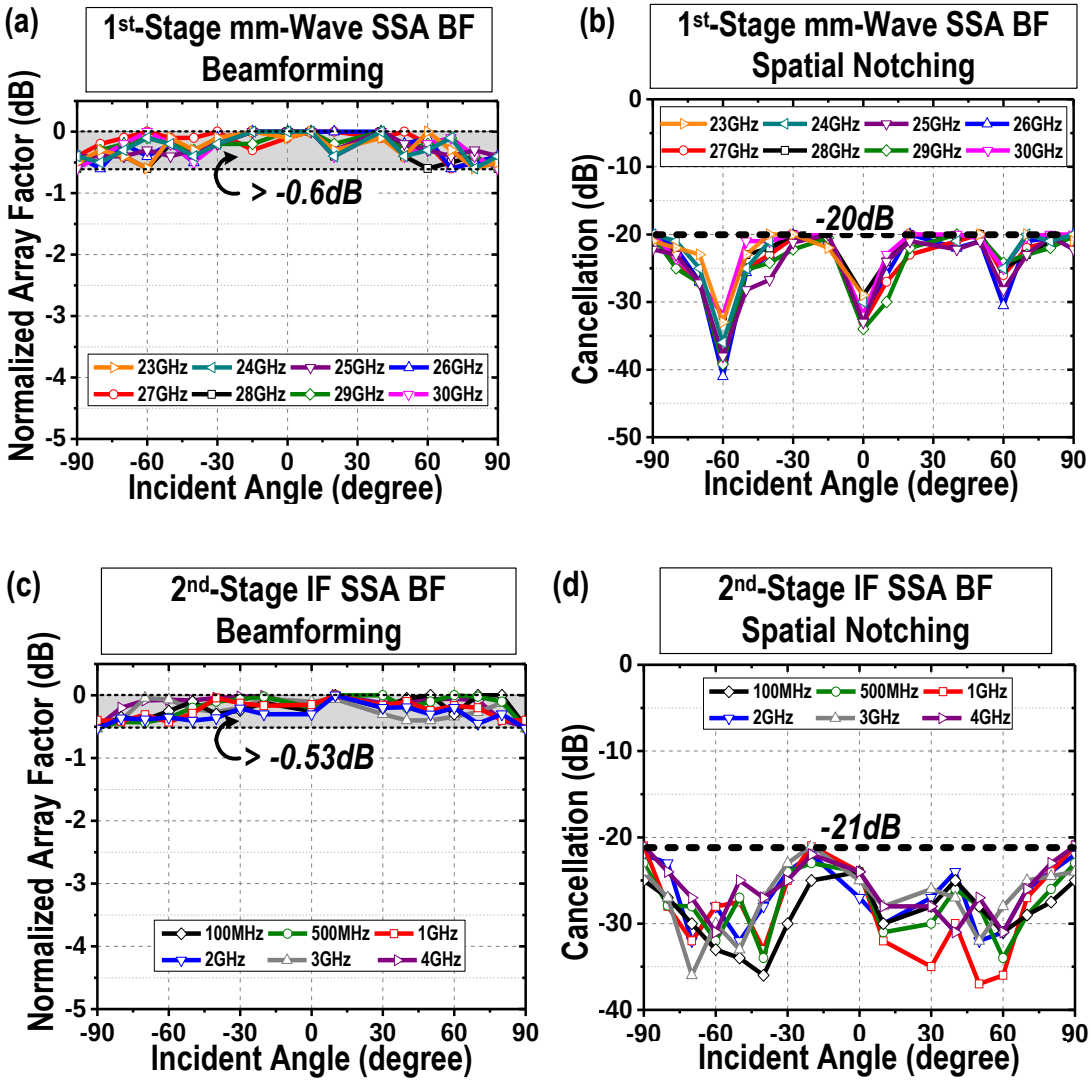

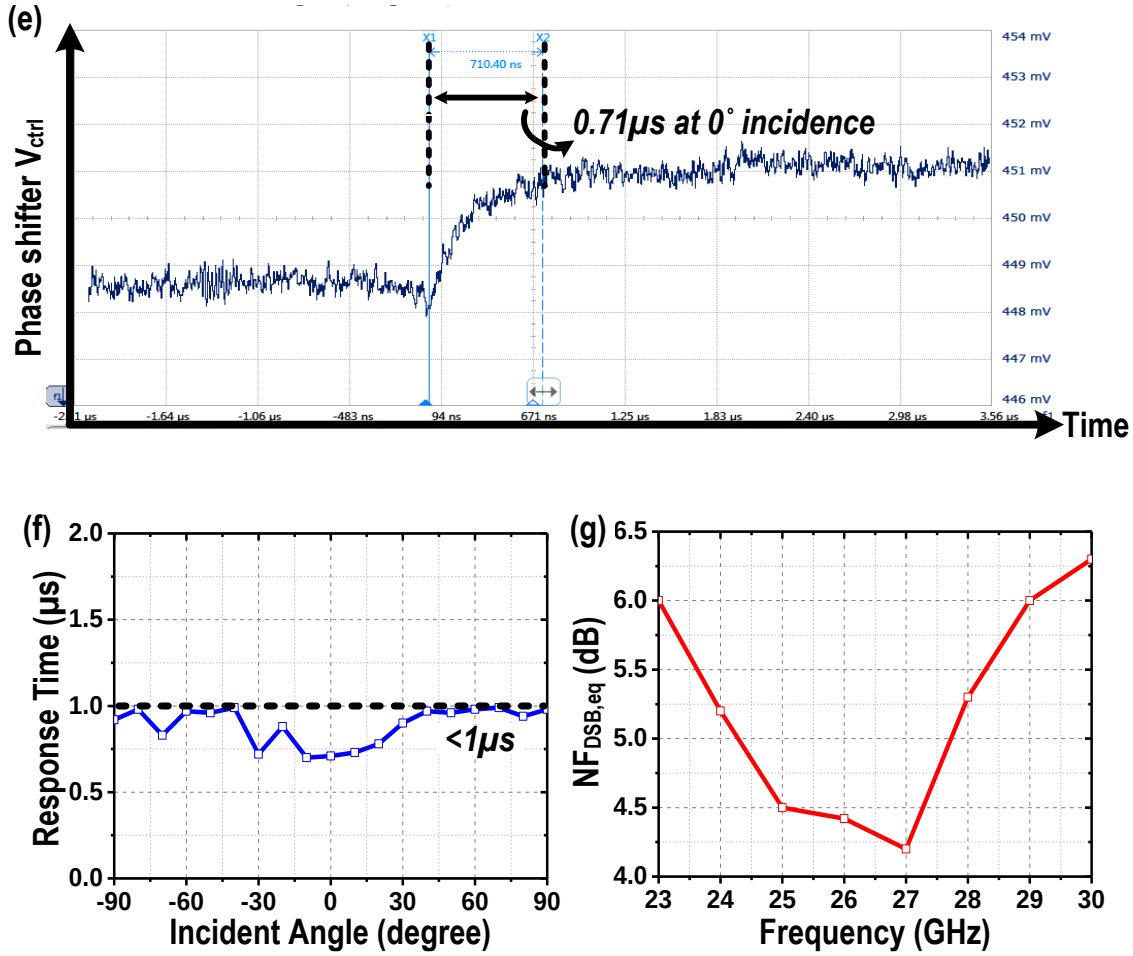

Figure 4.10 – (a)-(d) Measured wideband and full-FoV autonomous desired signal beamforming and blocker rejection in the 1st mm-Wave SSA BF and 2nd IF SSA BF. (e) Measured closed-loop response time of the SSA-BF using a real-time oscilloscope. (f) Measured dynamic response time over full FoV. (g) Measured $NF_{DSB,eq}$ with the 2-stage SSA BFs both turned on.

Next, the response time of each closed-loop DSP-free SSA BF stage is measured using a real-time oscilloscope as shown in Figure 4.10e. Over the full FoV, the measured response time is < 1μs (Figure 4.10f), achieving 100×~1000× faster response time than the existing state-of-the-art DSP-controlled BFs. The fast and instinctual yet precise response of the SSA BFs ensures rapid beam-forming/-tracking for the future mm-Wave low-latency applications. The equivalent single-element double-sideband noise figure ($NF_{DSB,eq}$) [74]

with the two-stage SSA BFs on is also measured with 4.2-6.3 dB over 23-30 GHz (Figure 4.10g).

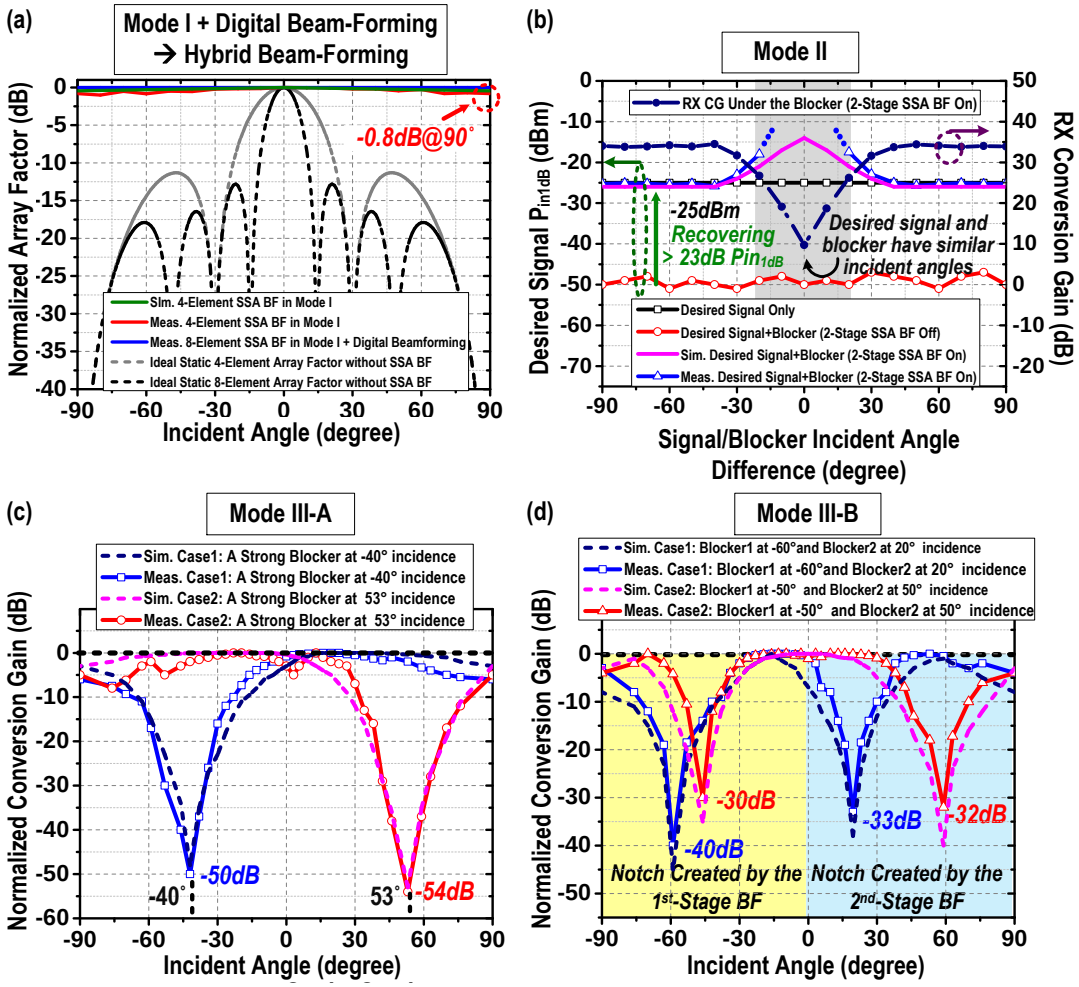

Figure 4.11 – Simulated and measured operation modes of the receiver array including: (a) Mode I (an 8-element hybrid beam-former). (b) Mode II (the RX Pin_{1dB} and conversion gain of the desired signal with the in-band blocker over full-FoV). (c) Mode III-A (one deep spatial notch over full-FoV). (d) Mode III-B (two independent spatial notches over full-FoV).

The 8-element RX array chip is then characterized for its various operation modes. In Mode I, when both the 1st- and 2nd- stage SSA BF are used with the combiners for desired signal BF, a 4-element SSA with flat normalized array factor >-0.8 dB over full FoV is achieved. The outputs of the two parallel 4-element SSA BFs are together with baseband

digital BF achieving a high-quality 8-element hybrid BF (Figure 4.11a). In Mode II, one desired signal and one medium-power blocker are simultaneously injected; the 1st-stage SSA BF suppresses the blocker, while the 2nd-stage SSA BF performs BF on the desired signal. The measured blocker-free RX Pin_{1dB} is -25 dBm/element. However, the RX Pin_{1dB} is degraded to <-48 dBm under a -15 dBm blocker (Pin_{1dB}+10 dB) injected to the RX. After the 1st-stage SSA BF is configured to autonomously suppress the blocker, the RX Pin_{1dB} is largely restored to the blocker-free value over a wide FoV (Figure 4.11b). However, if the desired signal is spatially aligned with the blocker, i.e. a small incident angle difference between the signal and blocker, the desired signal is also filtered by the 1st stage spatial notch, resulting in a larger but effectively erroneous Pin_{1dB} due to the lower conversion gain.

In Mode III-A, when a strong blocker and a desired signal are concurrently injected, the 1st- and 2nd- stage SSA BF both lock to the strong blocker and spatially notch it twice (Figure 4.11c). For different blocker incidence cases (-40° and 53°), a deep spatial notch is created to achieve maximum 54 dB rejection (Figure 4.11c). In Mode III-B, two moderate blockers and one desired signal are concurrently injected, the 1st- and 2nd- stage SSA BF sequentially lock to and suppress the two blockers, showing two different spatial notches with a maximum 40 dB rejection (Figure 4.11d). The Mode III-A/-B successfully relaxes the dynamic range of following ADCs and enables the digital BF.

4.4.2 Modulation Measurement

We also test the RX array under the Mode-II with wideband modulated co-channel blocker and desired signal without any digital BF. A desired signal (-46 dBm) and a

moderate co-channel blocker (-36 dBm), both wideband modulated with same modulation scheme and data rate, are injected (Figure 4.12). The desired signal and the blocker signal are first characterized with 100MSym/s / 500MSym/s 64QAM and 100MSym/s 256QAM. They are co-channel with a signal /blocker frequency separation offset f_{offset} = 100M/500MHz and 100MHz, respectively. When the 1st- and 2nd- stage SSA BF are off, the down-conversion spectra show that the blocker signal overwhelms the desired signal and the desired signal cannot be demodulated. After enabling the 1st-stage SSA BF for notching the blocker, the desired signal is autonomously beamformed at the 2nd-stage SSA BF and successfully demodulated, showing -27.2 dB EVM for 500MSym/s (3Gb/s) 64QAM and -32.6 dB EVM for 100MSym/s (0.8Gb/s) 256QAM.

The desired signal is then swept for its f_{offset} and incident angle difference from the blocker. The EVM performance of the demodulated desired signal is degraded when the f_{offset} is close to 0Hz, i.e, exact frequency overlap for the signal and the blocker, showing a clear spectral effect for various f_{offset} versus the co-channel SINR. On the other hand, if the desired signal is close to the spatial notch with a small signal/blocker incidence difference, the EVM performance is also degraded due to the attenuated desired signal strength, demonstrating a clear spatial filtering effect. The desired signal and the blocker signal are also measured with the high-speed 1GSym/s (6Gb/s) 64QAM and 200MSym/s (1.2Gb/s) 256QAM signal with 50% f_{offset} overlap in the spectrum (Figure 4.13). After the 1st- and 2nd- stage SSA BF are on, the desired signal is successfully demodulated with -25.7 dB and -31.8 dB EVM, exhibiting a first-ever demonstration for co-channel wideband modulated multi-Gb/s 64-/256-QAM blocker rejection.

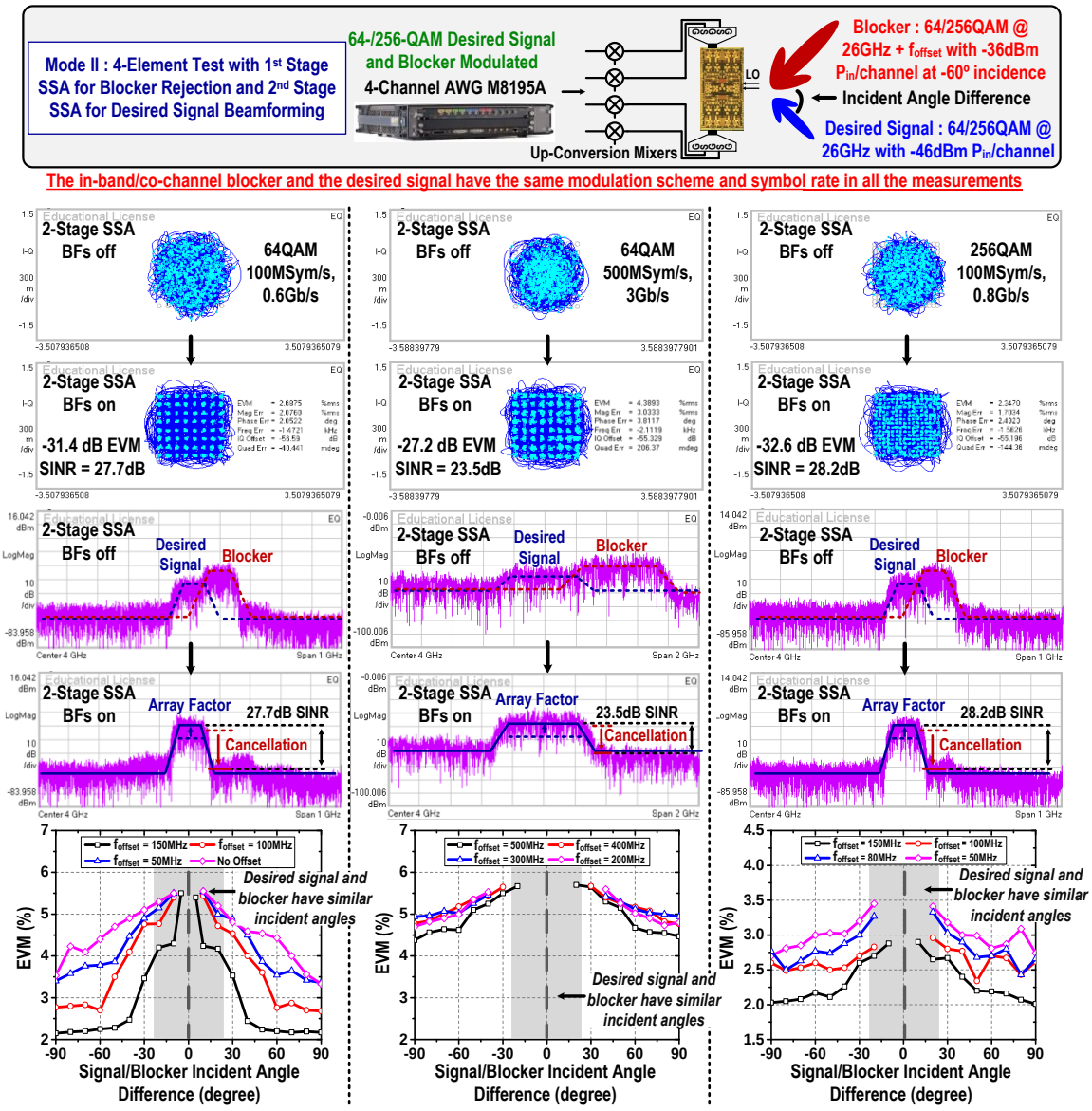

Figure 4.12 – Measured constellation and spectra of the co-channel blocker and the desired signal before and after turning on the 2-stage SSA BFs in Mode II. It demonstrates for blocker rejection and desired signal beamforming when the blocker and desired signal are both broadband modulated at the same scheme and speed. After the 2-stage SSA BFs are enabled, desired signal is successfully demodulated, showing autonomous spatial cancellation of co-channel blocker.

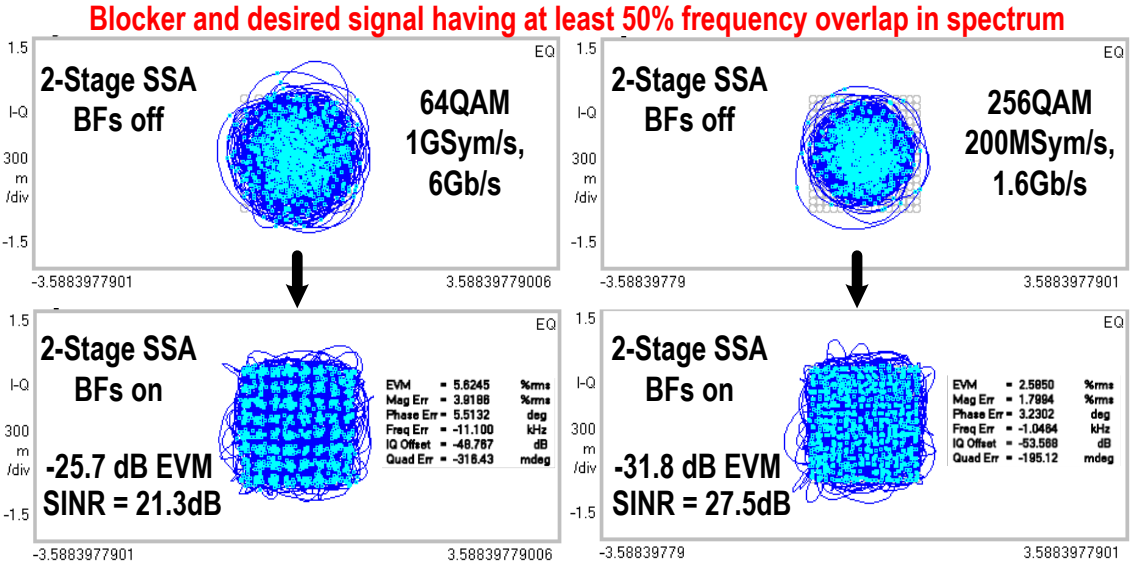

Figure 4.13 – Measured demodulated constellation of the desired signal with the co-channel blocker before and after turning on the 2-stage SSA BFs in Mode II, supporting autonomous multi-Gb/s 64-/256-QAM blocker rejection.

Table 4.1 compares the proposed mm-Wave MIMO RX array with the state-of-the-art designs. By exploiting the unique multistage closed-loop SSA BF architecture, the RX array demonstrates autonomous multiple concurrent blocker rejection and signal management. Measurement results show that the RX exhibits a full-FoV operation with low-latency < 1µs response time per SSA BF stage and achieves state-of-the-art wideband modulated multi-Gb/s 64-/256-QAM blocker rejection and signal BF.

Table 4.1 – Comparison with State-of-the-Art Spatial Notch Array RX, SSA RX, and Mm-Wave BF Array RX

	Spatial Notch Array RX		SSA RX		Mm-Wave Beam-Forming Array RX				
	L. Zhang JSSCC'17	S. Jain RFIC'16	M. Huang JSSC'17	A. Gupta TMTT'14	W. Roh Commun. Mag.'14	B.Sadhu JSSC'17	H. Kim JSSC'18	J. Dunworth ISSCC'18	This Work
Technology	65nm CMOS	65nm CMOS	130nm CMOS	45nm SOI	NR	130nm SiGe BiCMOS	28nm CMOS	28nm LPRF CMOS	**130nm SiGe BiCMOS**
Frequency (GHz)	0.1 – 3.1	10	4 – 5.68	7.4 – 9.4	28	28	25.8 – 28	25 – 30.5	**23 – 30**
Element No. /Chip	4	4	4	4	32	32	8	12	**8**
Blocker Rejection	Open Loop with DSP	Open Loop with DSP	No	No	No	No	No	No	**Closed Loop with SSA front-end BFs**
Beam-Forming	Open Loop with DSP	Open Loop with DSP	Closed Loop SSA	Closed Loop SSA	Open Loop with DSP	Open Loop with DSP	Open Loop with DSP	Open Loop with DSP	**Closed Loop with SSA front-end BFs**
Single-Element Conversion Gain (dB)	43	14	-8	NR	NR	34	39	22	**33**
$NF_{DSB,eq}$ (dB)[1]	3.4 - 5.8	9.5	NR	NR	NR	6[2]	6.7	4.4-4.8[2]	**4.2 – 6.3**
Spatial Blocker Suppression (dB)	56	32	No	No	No	No	No	No	**41 in Mode II and 54 in Mode III-A**
Blocker Modulation Scheme	CW	CW[3] / 200Mb/s QPSK[3]	No	No	No	No	No	No	**3Gb/s 64-QAM[4] and 0.8Gb/s 256-QAM[4]**
Desired Signal Modulation Scheme	2Mb/s QPSK	200Mb/s QPSK	NR	NR	2.1Gb/s 16QAM	NR	120Mb/s 64QAM	2.4Gb/s 64QAM	**3Gb/s 64-QAM[4] and 0.8Gb/s 256-QAM[4]**
EVM of Desired Signal after Blocker Rejection	2Mb/s QPSK: 20.5% [5]	NR	No	No	No	No	No	No	**0.6Gb/s 64-QAM : 2.68%[6] 3Gb/s 64-QAM : 4.39%[6] 0.8Gb/s 256-QAM : 2.34%[6]**
Response Time	NR	NR	3ms	NR	45ms	NR	NR	NR	**< 1µs per Beamformer Stage**
Power Consumption per Element (mW)	28.5 – 36.75	36.25	0	35.75	NR	206	50	42.5	**70**
Area (mm^2)	2.25	3.8	4.1	3.5	NR	165.9[2]	7.28[2]	29[2]	**21.6**

NR: Not reported. [1.] Equivalent Single-Element $NF_{DSB,eq} = NF_{DSB}$ measured with single-element excitation and output side beam-forming - 10log(number of elements). [2] It includes its transmitter design and T/R switch
[3.] Based on the RFIC'16 presentation slides, it presents CW blocker (when $P_{blocker} > P_{desired\_signal}$) and modulated blocker (when $P_{blocker} = P_{desired\_signal}$).
[4.] The modulation test is based on Mode II operation without any baseband digital beamforming. ($P_{blocker}$ = -36dBm and $P_{desired\_signal}$ = -46dBm.
[5.] 2 CW blockers + 1 modulated desired signal and f_{offset} / Modulation BW = 400%. [6.] 1 modulated blocker + 1 modulated desired signal and f_{offset} / Modulation BW < 100%.

CHAPTER 5. A MM-WAVE WIDEBAND MIMO RX WITH INSTINCTUAL ARRAY-BASED BLOCKER/SIGNAL MANAGEMENT FOR ULTRA-LOW-LATENCY COMMUNICATION

Chapter 5 demonstrates a wideband mm-Wave Multiple-Input-Multiple-Output (MIMO) receiver (RX) system with cascadable array-based high-order autonomous spatial filters (ASFs) for closed-loop frontend beamforming, achieving "instinctual" management of multi-blockers/signals with ultra-fast response time. Over a full Field-of-View (FoV), the ASFs achieve automatic blocker suppression and desired signal beamforming without prior knowledge on the Angle-of-Arrival/frequency/ modulation and without beam-searching using backend computations. In particular, the ASFs realize frontend blocker suppression and substantially relax the dynamic range requirement of down-stream analog-to-digital converters (ADCs) in digital arrays. Moreover, cascading multiple ASFs can sequentially suppress multiple blockers, essentially achieving the "iterative source localization" DSP algorithm by the frontend hardware. A proof-of-concept 27-41 GHz 4-element MIMO RX array is implemented in a 45nm CMOS SOI process to support multi-standard 5G links in future congested/contested EM environments. With autonomous cancellation of multiple co-channel wideband blockers, a wideband desired signal can be received with high SINR, achieving -28.64 dB EVM for 3Gb/s 64QAM and -32.73 dB EVM for 0.8Gb/s 256QAM. The measured MIMO beamforming response time for beam scanning, localization, and computation is < 1.75us/stage, enabling 5G and beyond-5G ultra-low-latency mm-Wave links.

5.1 Introduction

Mm-wave links will serve as the enabling technology for a plethora of commercial and defense applications, including 5G new radio, automotive radar, and drone-based networks [38]-[66]. With future ubiquitous mm-Wave links, mm-Wave transceiver (TX/RX) frontends should support high-reliability operations in future congested/contested EM environments and readily handle complex and fast-changing blocker scenarios, often with multiple blockers of unknown Angle-of-Arrival (AoA), frequency, and modulation. Different from conventional FoV limited analog beamforming, digital arrays are becoming a popular technology choice to support multi-beam MIMO operations with full field-of-view (FoV) by performing beamforming and spatial filtering all in the digital backend [73][74]. However, digital arrays typically need to handle all the aperture information and accommodate strong signals/blockers. Thus, the RX chain and ADCs require high dynamic range to avoid saturation, which exacerbates the power overhead of digital arrays. Therefore, there is a critical need for agile spectral-spatial frontend filtering for blocker suppression and spatial signal "power equalization" to aid digital arrays and reduce RX/ADC dynamic range requirements. In digital arrays, front-end spectral filtering, e.g., using mixers or filters, can readily suppress out-of-band blockers, but not in-band spatial blockers. Although generic frontend analog beamformers (BFs) create spatial notches [74][75], as fundamentally open-loop circuits, they require blocker knowledge beforehand or they rely on on-the-fly coefficient computation via digital backend [76], limiting their ability to handle unknown and dynamically changing blockers in complex EM environments. On the other hand, it is known that self-steering BFs can automatically align the RX array towards the incident beam in a close-loop fashion at the frontend. However,

most existing self-steering BFs exhibit limited functionalities. Van-Atta-array like BFs are simple reflectors that receive the incoming signal and then transmit it out with exactly the same information (modulation scheme or frequency). Coupled oscillators or coupled PLLs can serve as autonomous BFs as well. However, they often present limited FoV, and are not scalable to large arrays due to loop stability [7]. Moreover, their intrinsically nonlinear operation cannot support wideband Gbit/s complex modulations. Most importantly, in complex EM environment, most self-steering BFs will simply lock to the strongest blocker and cannot handle complex multi-blocker scenarios [7][9]. Recently, [48] demonstrated a DLL-like autonomous BFs as a hybrid beamforming architecture to suppress multiple unknown spatial blockers and support wideband Gbit/s signals. However, it performs only a 2-element spatial notch with limited spatial selectivity. More importantly, its array size reduces by ×2 after each autonomous beamforming stage; this cannot support true N-input-N-output MIMOs, and is undesired for digital arrays.To address these challenges and support future fast-changing and mobile mm-Wave applications, we present a scalable full-FoV MIMO RX architecture with array-based high-order autonomous spatial filters (ASFs) [64]. Our autonomous beamformer is defined as performing autonomous beam scanning, localization, and computation in the analog frontend without using any baseband/digital computation for beamforming, unlike most existing beamforming architectures [38],[72]-[76]. Multiple ASFs can be cascaded to realize frontend “iterative source location” DSP algorithm on multiple blockers without backend beam computation, achieving “instinctual” management on multiple blockers/signals. Moreover, the N-input-N-output RX architecture is conducive to MIMO systems. A proof-of-concept 27-41 GHz 4-element MIMO RX array with 3-stage ASFs is implemented in a 45nm CMOS SOI process to

support multi-standard 5G links in future complex EM environments. With autonomous cancellation of multiple in-band/co-channel wideband blockers, a wideband desired signal can be received with high SINR over full FoV and μs response time. With signal/blocker concurrent receiving (with blocker/signal power difference of 3-8dBc and frequency overlap up-to 50%), measurements shows receiving 3Gb/s 64QAM at - 28.64 dB EVM and 0.8Gb/s 256QAM at -32.73 dB EVM with ASFs on. To the best of the authors' knowledge, this is the first MIMO array with a generalized iterative source location architecture via autonomous scalable N-input-N-output array-based high-order spatial filters for wideband modulated 64-/256-QAM blocker rejection and desired signal beam-forming with μs response time, necessary for 5G and beyond-5G ultra-low-latency mm-Wave links.

This Chapter is organized as follows. Section 5.2 presents the proposed N-input-N-output MIMO system architecture using scalable cascadable multistage autonomous array-based spatial filters. The operation principles and circuit details are shown in Section 5.3. Section 5.4 demonstrates the measurements and a performance comparison with reported MIMO RX arrays.

5.2 MIMO Receiver with N-Input-N-Output Multi-Stage Array-Based Closed-Loop Signal Processing

5.2.1 System Architecture

The proposed wideband N-input-N-output MIMO RX array architecture is shown in Figure 5.1a. First, the RX frontend consists of mm-Wave broadband low noise amplifiers

(LNAs) and passive mixers for wideband and high-linearity spectral filtering. Then, after down-conversion, the RX frontend employs scalable array-based high-order ASFs as a "smart" frontend spatial filter bank to process multiple signals/blockers managements and assist the following downstream digital beamforming. The proposed ASF spatial selectivity could be further enhanced via its high-order scalability and each identical ASFs can be cascaded to perform front-end based "iterative source localization" computation on multiple blockers/signals sequentially [64]. Different from hybrid beamforming architectures [72][73], our proposed ASF-based frontend filtering ensures N-input-N-output without reducing the MIMO array order or compromising the FoV of the downstream system. Due to progressive phase shift symmetry of the proposed architecture (Figure 5.1b), scalability to a large MIMO array can be achieved by arranging multiple RX array chips along a zero-phase symmetric reference plane (Figure 5.1b). A proof-of-concept 27-41GHz 4-element broadband MIMO array chip is implemented in a 45nm CMOS SOI process that will be presented in this Chpater (Figure 5.1a).

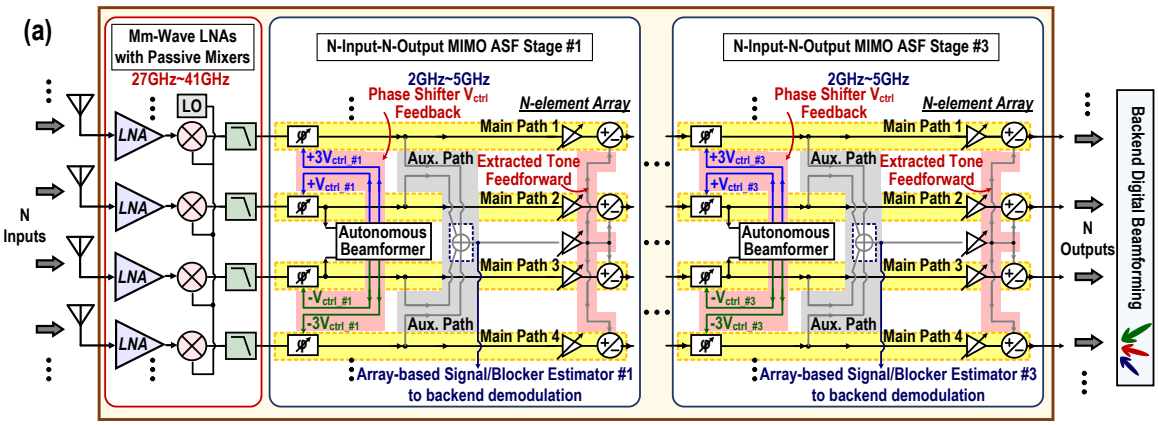

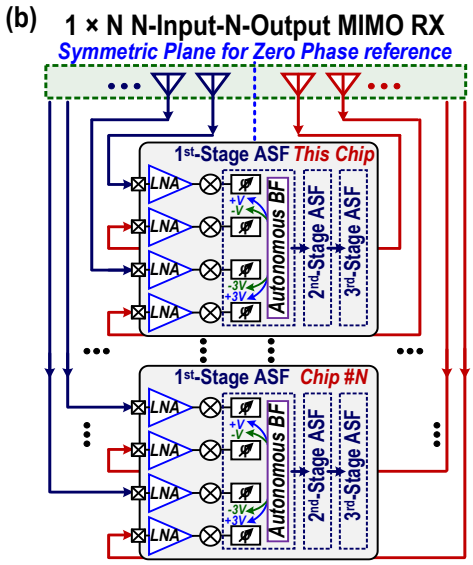

Figure 5.1 – (a) System architecture of the 27-41GHz N-Input-N-Output MIMO RX with scalable cascadable array-based high-order ASFs for instinctual full-FoV signal/blocker management. (b) Scaling to 1×N MIMO arrays by assembling multiple unit chips along the zero-phase symmetric reference plane.

5.2.2 Scalable Array-Based High-Order ASFs

In a uniform 1×4 array, the input progressive phase shift difference between path 1 and path 4 (the outer two paths) is three times ($3\phi_{in}$) of that for path 2 and path 3 (the inner two paths). Therefore, we can set a Symmetric Plan as the Zero Plan Reference in between path 2 and path 3 (the inner two paths). Referenced to this Zero Phase Reference, the input progressive phase shifts of path 1 to path 4 thus are $+3\phi_{in}/2$, $+\phi_{in}/2$, $-\phi_{in}/2$, and $-3\phi_{in}/2$. Figure 5.2shows a conceptual diagram for multiple signals processing in the following ASF. The ASF comprises phase shifters (PS), a closed-loop autonomous beamformer (BF), an auxiliary (Aux.) path for array-based signal/blocker extraction, and feedforward subtraction (combining) for spatial-notching (beamforming). Next, its operation details are explained (Figure 5.2).

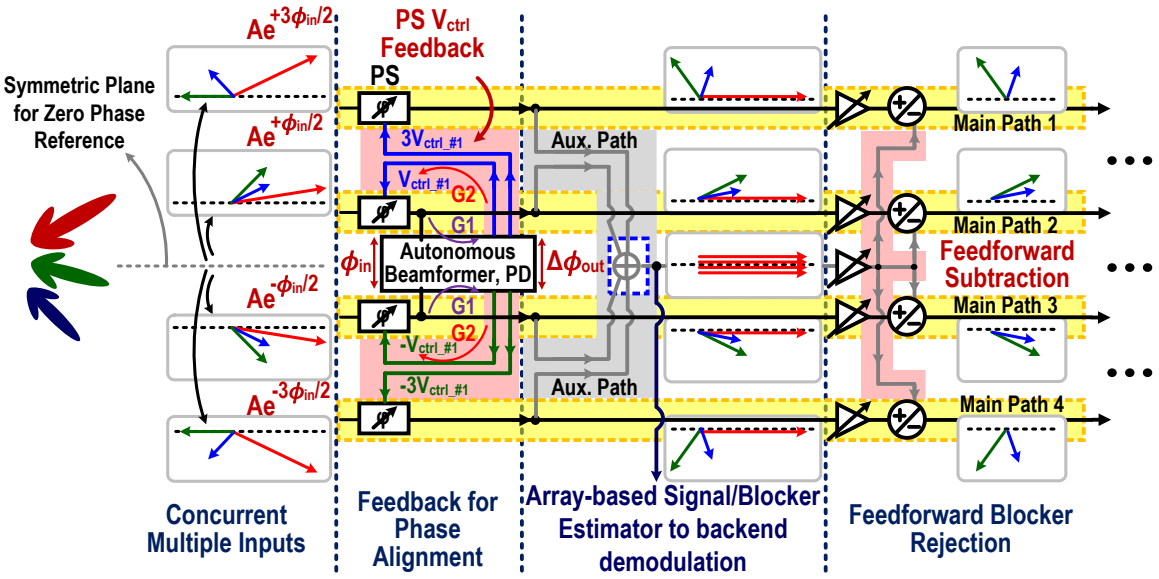

Figure 5.2 – 4-element conceptual diagram for the operation of the autonomous N-Input-N-Output array-based high-order ASF.

5.2.2.1 Closed-Loop Autonomous Beamformer

Assume a simple scenario with one received signal at an incident angle θ. A power-aware nonlinear phase detector (PD) detects the phase difference $\phi_{in} = \pi\sin\theta$ between the inner two channels and generates a differential output DC voltage (Figure 5.2) with a phase-to-voltage conversion gain G_1. The differential output DC voltage is then fed to the PS as the control voltages to apply phase shifts, resulting in a voltage-to-phase conversion gain G_2 [67]. The PD and PS forms a negative-feedback in the phase domain with a phase-to-phase loop gain of G_1G_2. In its closed-loop operation, the output residual phase difference $\Delta\phi$out can be expressed as [66]

$$\Delta\phi_{out} = \phi_{in} / (1+ G_1G_2) = \pi\sin\theta / (1+ G_1G_2). \quad (5.1)$$

A large loop gain G_1G_2 directly minimizes the resulting phase difference $\Delta\phi_{out}$ of the two paths and autonomously aligns their phases, similar to a delay-lock-loop (DLL) but now

operating as a beamformer. Unlike coupled PLL/oscillator self-steering arrays [7]-[9], our DLL-like autonomous BF does not require resonators or multipliers, and supports broad carrier frequencies. It is shown that for such an autonomous BF, a large phase domain loop gain G_1G_2 will ensure a full FoV coverage and improve the robustness against PD phase/amplitude variations [66]. The IF variable gain amplifiers (VGAs) in the feedback boost the loop gain and achieve a near-zero residual phase error $\Delta\phi$out, even for end-fire incidence ($\theta = \pm 90^{\circ}$) [67]. The autonomous beamformer can be extended to a large array size. Taking a uniform 1×4 array as an example, the input progressive phase shift of the outer two paths (Main path 1 and Main path 4) is three times of that of the inner two paths. Thus, to align the entire RX array for the detected tone, progressively scaled feedback PS control voltages should be applied to the four paths as $-3\times V_{ctrl}$, $-1\times V_{ctrl}$, $+1\times V_{ctrl}$, and $+3\times V_{ctrl}$ to compensate for the corresponding phase differences. Further scaling can be performed similarly. Taking the center plane as a zero-phase reference, the input progressive phase differences for all the channels are $\pm \phi_{in}/2$, $\pm 3\phi_{in}/2$, …, $\pm (N-1)\,\phi_{in}/2$ in an N-element uniform RX array, requiring feedback PS control voltages are $\pm V_{ctrl}$, $\pm 3V_{ctrl}$, and $\pm(N-1)V_{ctrl}$, correspondingly. When multiple co-channel tones are received, the power-aware PD responds to the strongest tone and performs autonomous beamforming on it (Figure 5.2). Measurements show this power-aware PD and beamforming characteristics (Figure 5.10a). As long as two tones exhibit a power difference larger than 1dB, the autonomous BF will respond to the stronger tone.

5.2.2.2 Auxiliary Path for Array-Based Signal/Blocker Extraction

Now all the N channels are phase-aligned towards the strongest tone by the autonomous BF. The signal path in each channel is then split into two, and an auxiliary

(Aux.) path is introduced to sum the N channels together. This essentially performs beamforming and extraction on the strongest tone, while the other tones are suppressed by the spatial filtering since they are not in-phase among the N-channels (Figure 5.2). It is clear that adding more channels in the ASF enhances the selectivity of this spatial extraction on the strongest tone and maximizing the suppression on the other tones. This extracted tone can be digitized and one-step de-modulated at the baseband, so that the RX system can decide whether it is a blocker or a desired signal. Since this extraction is already the strongest tone and other weaker tones are further suppressed by the Aux. path beamforming, its digitization only requires an ADC with a relaxed dynamic range. Moreover, this one-step demodulation for blocker/signal identification requires negligible backend computation, compared to running an FFT on the entire array in conventional digital beamforming. Notably, although blocker/signal classification needs one-step DSP demodulation, as this is true for most other RX systems, the proposed MIMO does not require DSP for beam scanning, localization, and computation, drastically accelerating the signal beamforming/blocker rejection, which also doesn't require prior knowledge for AoA, frequency, and modulation.

5.2.2.3 Feedforward Subtraction (Combining) for Spatial Notching (Beamforming)

Next, the extracted strongest tone is feedforwarded to the N-channel Main paths. If it is a desired signal, the combiner "+" is selected to perform constructive beamforming. For an unwanted blocker, subtraction "-" is chosen to form a spatial notch and suppress this strongest tone. Although other tones (e.g., green and blue tones in Figure 5.2) are also present in the Aux path, they are largely attenuated by the spatial selectivity of the beamforming before the feedforward operation, so that their presence in the Main paths

will not be affected significantly. To verify that the spatial notch selectivity can be enhanced by ASFs with large number of array elements, assume the strongest tone (a blocker) has an amplitude of A and one weaker received tone at phase difference of ϕdiff from the blocker is examined. The normalized N-element array factor (AF) gain |AF(ϕ_diff)|created in the Aux paths can be expressed as

$$|AF(\phi_{diff})| = |\frac{A}{N}[e^{j\left(-\frac{(N-1)\phi_{diff}}{2}\right)} + \cdots + e^{j\left(-\frac{3\phi_{diff}}{2}\right)} + e^{j\left(-\frac{\phi_{diff}}{2}\right)} + e^{j\left(+\frac{\phi_{diff}}{2}\right)} + e^{j\left(+\frac{3\phi_{diff}}{2}\right)} + \cdots + e^{j\left(+\frac{(N-1)\phi_{diff}}{2}\right)}]| = \frac{A\sin(\frac{N\phi_{diff}}{2})}{N\sin(\frac{\phi_{diff}}{2})}, \text{ where } \phi_{diff} = \pi\sin\theta_{diff}. \quad (5.2)$$

It shows that $|AF(\phi_{diff})|$ peaks at $\phi_{diff} = \theta = 0^{\circ}$ and the first null can be calculated as

$$\frac{N\phi_{diff}}{2} = \pm\pi \text{ and } \phi_{diff} = \pi\sin\theta_{diff} = \frac{\pm 2\pi}{N}. \quad (5.3)$$

Thus, the first null incident angle for a uniform λ/2 array is

$$\theta_{null\_1st} = \pm\sin^{-1}\frac{2}{N}. \quad (5.4)$$

For a large N element array (N >>1), the first null beamwidth angle can be approximated as

$$\theta_{BW\_null\_1st} = \left|2\sin^{-1}\frac{2}{N}\right| \approx \frac{4}{N}. \quad (5.5)$$

Based on (5.4), as N increases, the BF in Aux paths achieves higher-order AF with narrower beamwidth for a sharper spatial selection. Feedforward subtraction of this Aux path BF signal in the Main paths then realizes a spatial notch (Figure 5.3a). The null beamwidth of the Aux path BF becomes the notch beamwidth after feedforward

subtraction. Simulated 2-/4-/8-element array-based high-order spatial filter results are shown in Figure 5.3b. The notch beamwidth for the high-order ASF is 180˚(±90˚)/60˚(±30˚)/29˚(±14.5˚) and 10-dB suppression notch beamwidth is 59˚(±29.5˚)/27˚(±13.5˚)/12.8˚(±6.4˚) respectively, clearly showing a sharper spatial notch selectivity when the array size increases (Figure 5.3b). Effect of mismatch on the ASF spatial notch is discussed in Section 5.3.4.

5.2.2.4 Cascading ASFs for Front-End "Iterative Source Localization" Computation

In digital BF, to handle multiple received tones with large blockers, a DSP algorithm "Iterative Source Localization" is often used in backend computation [81]- [101]. First, an array-scaled FFT is performed to identify the spatial signature of the strongest tone, whose side-lobes may shadow other weaker signals. Next, this strongest tone is spatially filtered, and another FFT is performed on the remaining signals. This process is repeated to resolve all the received signals.

When cascading multiple ASF stages, the RX MIMO essentially realizes this "Iterative Source Localization" DSP algorithm yet at the RF/analog layer and more importantly in an autonomous fashion. The first ASF autonomously tracks and spatially filters out the first strongest tone (red in Figure 5.2). Note the feedback PS control voltages generate progressive phase shifts for the N channels on all the signals. Therefore, after notching the strongest tone, the remaining tones (green and blue in Figure 5.2) still preserve their progressive phase relationships among the N-channels. In addition, the ASF maintain its N-input-N-output configuration without sacrificing the array order or the array FoV (except for the spatial notches). Therefore, the 2nd ASF stage can again operate on the

remaining signals and similarly notch out the 2nd strongest tone (green in Figure 5.2). Alternatively, the cascaded ASFs operation can be explained in an intuitive way as follows. Essentially, the 1st-stage ASF rotates the entire MIMO array and aligns its boresight towards the strongest received tone, which is then spatially notched by the 1st ASF feedforward subtraction. Next, the 2nd-stage ASF aligns the entire MIMO array towards the second strongest tone and then notches it. This process is iterated through M ASF stages, so that the first M strongest tones are autonomously identified and removed from the received signals. Thus, the array size (N-input-N-output) and its FoV (except for the spatial notches) are preserved. This makes the proposed ASFs as ideal frontend spatial filter in a digital beamforming array. They relax the dynamic ranges of the downstream circuits and ADCs and more importantly allow the digital beamforming DSP backend to scan through the remaining FoV for signal identification with no loss of spatial information. In addition, different from other MIMO RX arrays with front-end spatial filtering [74]-[76], the proposed ASF with the power-aware PD acts only on the RF power and does not need any prior AoA/frequency/modulation information or external beamforming amplitude/phase controls. Thus, it is able to handle unknown blockers/signals without DSP backend beam computations. As a result, multiple ASF spatial notches can autonomously track multiple blockers via their closed-loop operation, ensuring low response time and latency for complex EM environment and dynamic mm-Wave applications.

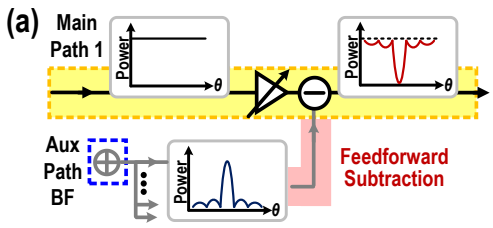

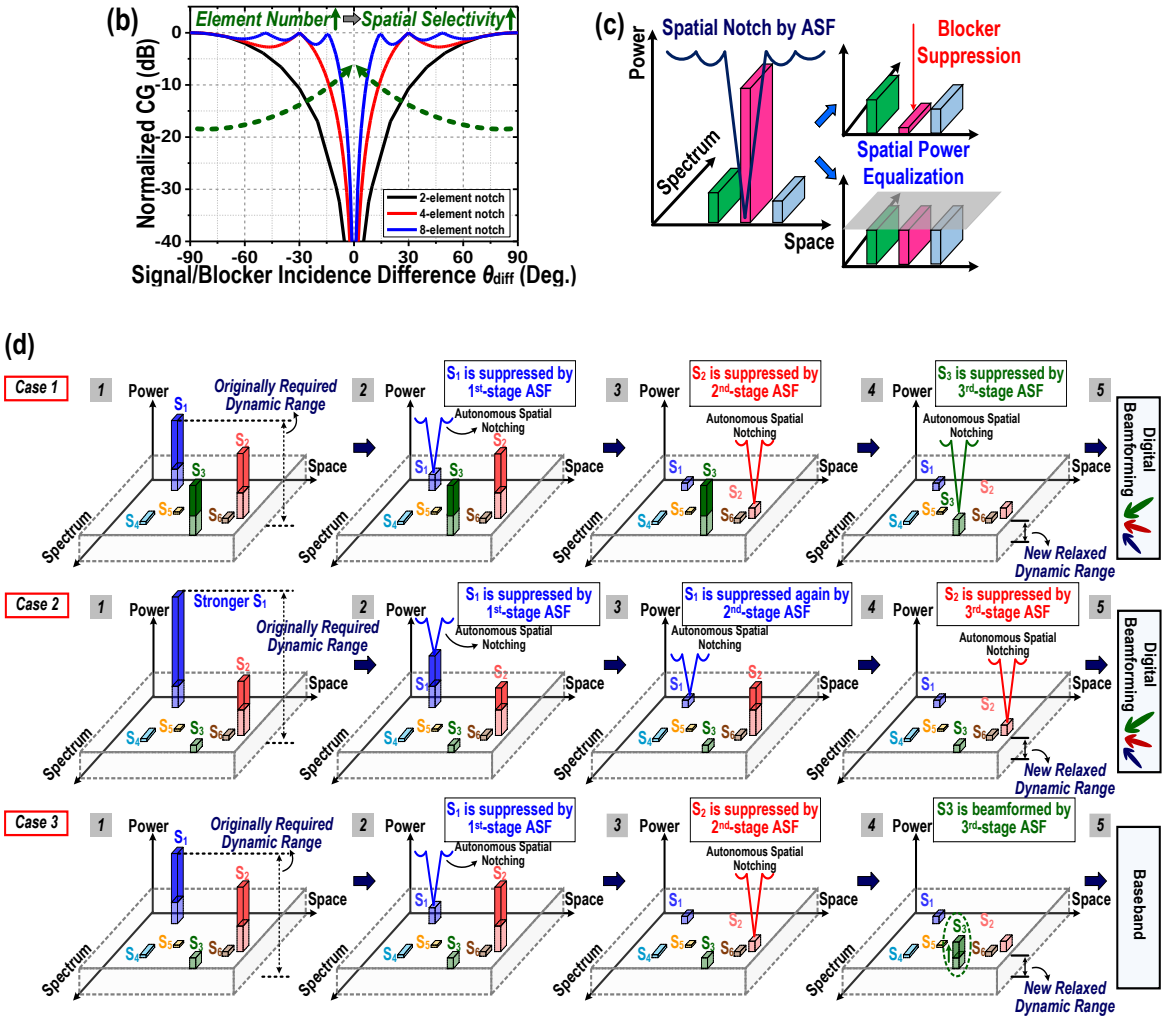

Figure 5.3 – (a) Conceptual diagram for array-based high-order spatial notching. (b) Simulated sharpened spatial effect versus element number. (c) ASF for blocker rejection or desired signal power equalization. (d) Various dynamic MIMO operation cases to relax dynamic range requirement for RXs/ADCs.

5.2.3 Reconfigurable ASFs for Various MIMO Scenarios

Cascading multiple ASFs offers reconfigurable modes for different MIMO scenarios. Cascading three ASFs for three operation cases are presented here as an example (Figure 5.3d). It is assumed that blockers are always stronger than desired signals. In case I, the three ASFs all use subtractors and create three independent spatial notches to autonomously and sequentially suppress three unknown in-band wideband blockers. In

case II, for one strong blocker and one medium-power blocker, the RX can suppress the strong one twice by the 1st- and 2nd-stage ASFs to create a deep spatial notch, and reject the other medium-power unknown blocker by the 3rd-stage ASF. In case III, the first two ASFs use subtractors, and the third ASF uses a combiner. Thus, the first two ASFs create two array-based spatial notches to autonomously suppress two unknown in-band blockers, and the third ASF enhances one desired signal for high SINR by autonomous beamforming. Notably, the power-aware PD ensures that the first two ASFs only spatially notch the two strong blockers instead of the desired signal.

5.2.4 Autonomous Beamforming Architecture Comparison

It is essential to compare this MIMO RX architecture with a recently published work [48]. Both achieve autonomous beamforming MIMO RX systems for unknown blocker rejection and signal beamforming with μs rapid response time. [48] is a hybrid beamforming architecture that realizes direct spatial filtering and beamforming at each of its self-steering array (SSA) stages (Figure 5.4a). Although a 2-element SSA spatial notch is reported, it can be readily extended to a higher-order SSA notch. Its MIMO array order decreases after each SSA stage (by 2 in this reported design), just like any hybrid beamforming arrays [38]. However, this hybrid beamforming architecture can autonomously process sub-arrays for signal/blocker managements and combine all the sub-arrays at the digital beamforming. In contrast, the proposed system in this Chapter preserves the MIMO FoV and size (N-input-N-output) through its ASF operations (Figure 5.4b). It can be readily scaled up with large number of array elements to enhance the spatial selectivity of ASF notches. Thus, the system in this Chapter is ideal as “intelligent”

frontend spatial filters to assist digital beamforming systems by reducing the required dynamic range of the downstream electronics.

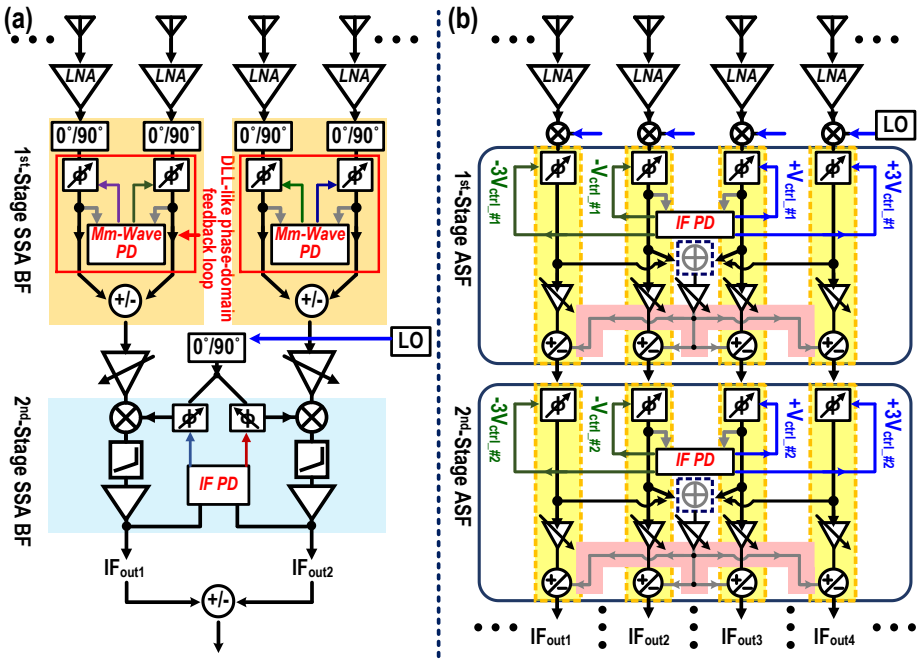

Figure 5.4 – (a) Autonomous self-steering array (SSA) BF [48]. (b) Proposed N-input-N-output MIMO.

5.3 Circuit Implementation and Analysis

A proof-of-concept 27-41GHz mm-Wave wideband 4-input-4-output MIMO RX array chip with 3-stage ASFs is implemented [64]. Detailed circuit implementations for the front-end and the ASFs with voltage-to-phase conversion as well as phase-to-voltage conversion are analyzed.

5.3.1 Wideband Mm-Wave Front-End

A two-stage LNA is designed with resonant loads at different frequencies to provide broadband performance (Figure 5.5a). The simulated performance for the frontend is

shown in Figure 5.5b. It achieves S11 < -10 dB from 28-44 GHz. Then, at the LNA output, the passive mixers are chosen to mitigate the entire RX linearity requirement for the following cascaded IF ASFs. The overall frontend (LNA + Mixer) conversion gain is at peak 20.1 dB with 15 dB tunable gain from 27.5-41.5 GHz with a fixed IF 3.5GHz, enabling 5G multi-band applications (Figure 5.5b).

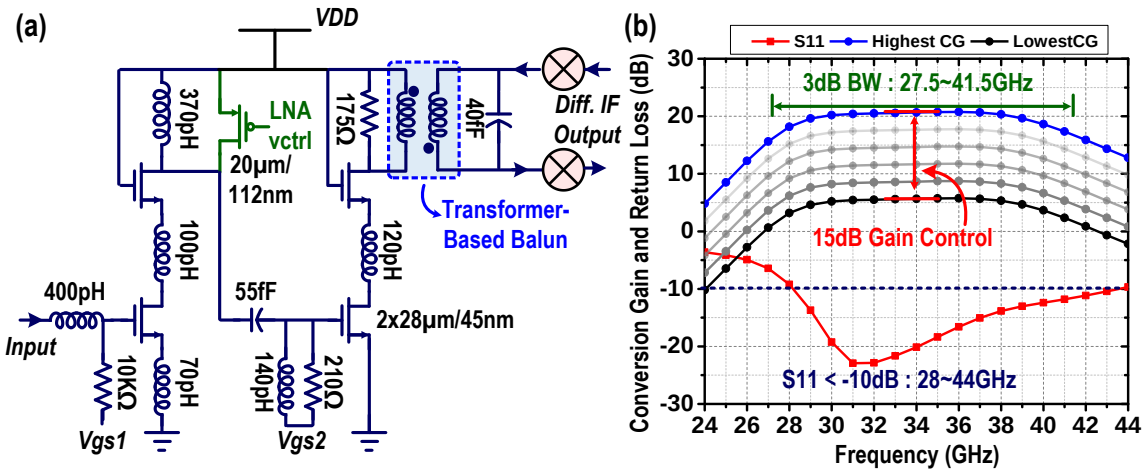

Figure 5.5 – (a) Schematic of the two-stage LNA with following passive mixers (b) Simulated conversion gain and S11 of the mm-Wave frontend.

5.3.2 Phase-to-Voltage Conversion

The simplified schematic of the phase-to-voltage conversion G_1 circuit is shown in Figure 5.6a. It is composed of a compact transformer-based low-loss differential 90˚ coupler [21][22], IF VGAs, multi-stage Dickson voltage rectifiers, and feedback DC voltage generators. The differential input (IN) and isolation (ISO) ports of the 90° coupler are used to sense phase-shifts in the adjacent inner two paths and the outputs from the differential through (THU) and coupled (CPL) ports are followed by the IF VGAs and the multi-stage Dickson voltage rectifier (Figure 5.6a). Compared to CMOS based square-law devices [102], the multi-stage Dickson voltage rectifiers are chosen to have larger output

DC dynamic range to detect from relatively small signals to blockers since the DC outputs are not clipped out by any fixed VDD. Compared to [48], the G_1 circuit in this Chapter includes common-mode feedback circuit to well control feedback voltage and DC voltage multiplier for progressive voltage generations in outer paths. Overall loop gain is explored and boosted to achieve full FoV coverage without any significant degradations [48]. Output differential control voltages Vctrl of the rectifiers are then fed into the wideband continuous-tuning I/Q voltage-controlled IF PS to generate the compensation phase ϕ_{FB}. The large-signal behavior model of the phase-to-voltage converter is then analyzed. Assume two IF incident signals with the same amplitude A but with a phase difference $\Delta\phi$out are injected into the IN and ISO ports of the 90° coupler. IF VGAs amplify the output RF signals at the THU and CPL ports with a gain α. The amplified output voltages are further converted to a differential feedback DC voltage Vctrl with rectification efficiency β. Assuming the two matched rectifiers are square-law devices, the Vctrl of the two rectifiers is [48]

$$V_{ctrl} = V_{DC1} - V_{DC2} = 2\alpha^2\beta A^2 \sin \Delta\phi_{out}. \quad (5.6)$$

The phase-to-voltage conversion gain G_1 is calculated as [48]

$$G_1 = V_{ctrl}/\Delta\phi_{out} = 2\alpha^2\beta A^2 \sin \Delta\phi_{out}/\Delta\phi_{out}, \quad (5.7)$$

which is designed >100 (linear scale). The conversion efficiency β is also maximized by loading a high impedance, i.e., the gates of the common-mode feedback (CMFB) DC amplifiers, which enhances RF power to DC voltage conversion [48]. Two inverting DC amplifiers with 1:3 ratio feedback resistors are then used to generate $\pm V_{ctrl}$ and $\pm 3V_{ctrl}$ (Figure 5.6a) for corresponding progressive compensation phase shifts to the inner and the

outer two paths. By conversion for the two independent domains (phase and voltage information), the proposed PD is not distorted by the amplitude/phase mismatch, robust to voltage-dependent phase or phase-dependent voltage error [48] as a precise PD.

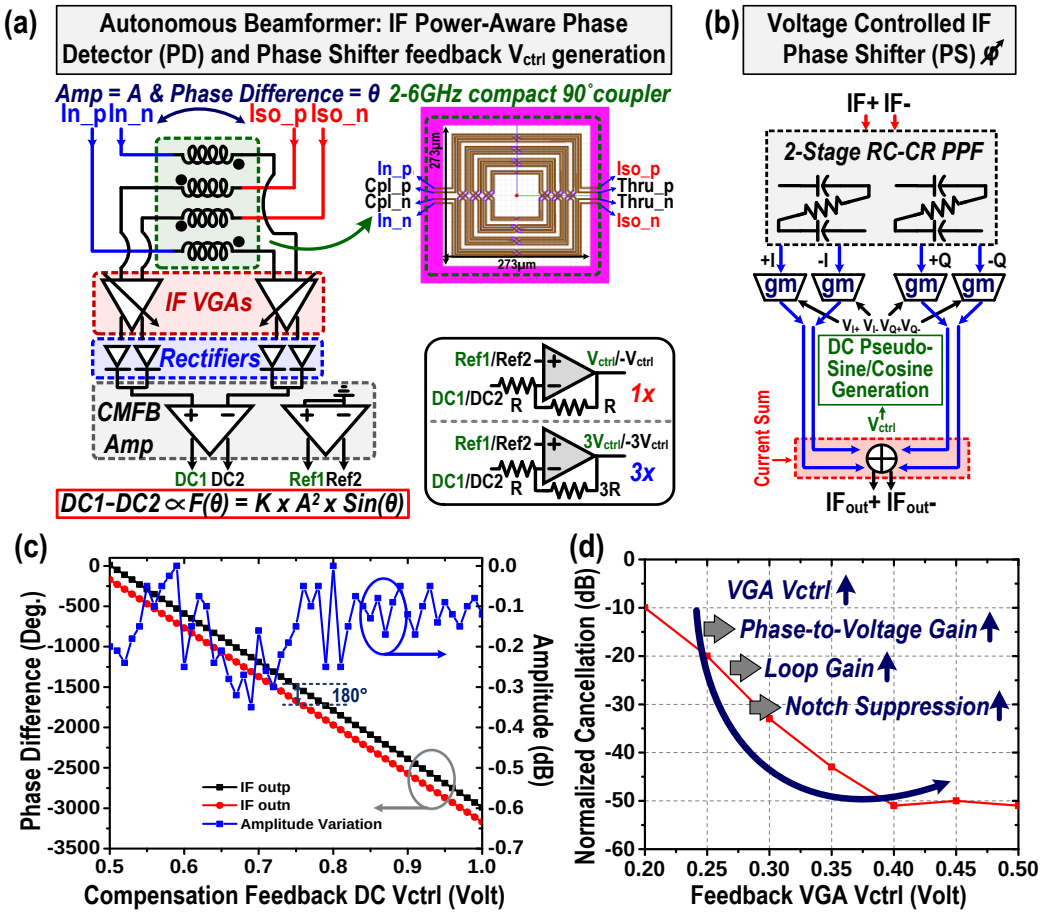

Figure 5.6 – Schematic of the (a) G_1 and (b) G_2 circuit. (c) Simulated output phase and normalized amplitude variation and versus V_{ctrl} of the wideband IF IQ phase shifters. (d) Measured tunable notch depth by changing the ASF feedback gain for multi-signal power-equalization.

5.3.3 Voltage-to-Phase Conversion

The schematic for the wideband IF I/Q voltage-controlled continuous PS as the voltage-to-phase converter is shown in Figure 5.6b. It consists of a two-stage RC-CR poly-phase filter and an analog multiplier with built-in DC pseudo-Sine/-Cosine generation [48]

as a I/Q vector-modulator PS. The proposed wideband full-range continuous-tuning IF I/Q vector-modulator analog PS only requires one analog control voltage, ensuring control simplicity for the proposed scalable closed loop. The $\pm V_{ctrl}$, $\pm 3V_{ctrl}$ generated from phase-to-voltage convertor are then sensed by the IF I/Q vector-modulator PS with corresponding compensation phase shift $\pm\phi_{FB}$, $\pm 3\phi_{FB}$, completing the negative feedback loop. The voltage-to-phase conversion gain is expressed as

$$G_2 = \phi_{FB}/V_{ctrl}. \tag{5.8}$$

The DC Pseudo-Sine/-Cosine generation can be easily extended to achieve a large phase tuning range for accommodating wide linearly progressive compensation phase shifts such as $\pm\phi_{FB}$ (±180°), $\pm 3\phi_{FB}$ (±540°), … to cover full FoV incidence for a large scaled array. Simulated amplitude and phase response of the PS shows that it performs continuous phase shift > 3000˚ with only <0.35 dB amplitude variation (Figure 5.6c), achieving highly linear phase shifts with negligible amplitude changes. The simulated voltage-to-phase conversion gain G_2 is 6°/mV at 3.5 GHz (Figure 5.6b).

5.3.4 Loop Analysis of the ASFs

The phase-domain closed-loop performances of the Aux BF and ASFs with feedforward cancellation are then analyzed. First, the residual output phase difference $\Delta\phi_{out}$ in the Aux paths can be expressed as [48]

$$\Delta\phi_{out} = \pi\sin\theta /(1+G_1G_2)$$

$$= \pi\sin\theta / [1+ (2\alpha^2\beta A^2 \sin \Delta\phi_{out}/\Delta\phi_{out})G_2]. \tag{5.9}$$

Notably, the G_1 varies with $\Delta\phi_{out}$ after the phase compensation, which shows the proposed feedback loop is a nonlinear loop and (5.9) can be modified as

$$\Delta\phi_{out} + k \sin \Delta\phi_{out} = \pi\sin\theta, \tag{5.10}$$

where $k = 2\alpha^2\beta A^2 G_2$. k has a quadratic relationship with the input IF input amplitude A, showing that the loop response is a function of the input power. The large-signal loop gain $G_1G_2 = (2\alpha^2\beta A^2 \sin \Delta\phi_{out}/\Delta\phi_{out})G_2$ peaks at θ = 0° and gradually decreases when θ approaches ±90° [48]. However, based on its nonlinear bifurcation behavior, as long as the k is >>1, the feedback loop can maintain its peak loop gain value with full-FoV operation even at incidence ±90° without any substantial degradation. Then, the residual phase difference $\Delta\phi_{out}$ is highly suppressed ~0° and the 4-element-based BF in Aux paths via (5.2) can be expressed as

$$F(\Delta\phi_{out}) = |AF| = \frac{A \sin(\frac{4\Delta\phi out}{2})}{4\sin(\frac{\Delta\phi out}{2})}, \tag{5.11}$$

and 4-element-based ASF after the feedforward cancellation is

$$1- F(\Delta\phi_{out}) = 1- \frac{A \sin(\frac{4\Delta\phi out}{2})}{4\sin(\frac{\Delta\phi out}{2})} \approx 1- \frac{A \cos(\frac{4\Delta\phi out}{2})}{\cos(\frac{\Delta\phi out}{2})} = 0, \tag{5.12}$$

where the $\Delta\phi_{out} \approx 0°$. It shows the proposed array-based high-order ASF can achieve ideally perfect cancelation regardless of the incidence of the blocker. With the targeted loop gain > 600 (linear scale), simulated residual phase difference $\Delta\phi_{out}$ can be highly suppressed to < 0.5° and maximum >50dB ASF cancellation over full FoV. The dominant pole of the proposed feedback is designed to achieve fast response time. Simulated

instinctual response time for each array-based high-order ASF stage is < 1μs, ensuring dynamic tracking for the signal/blocker and low-latency communications. The spatial notch depth is also tunable by the IF VGA in phase-to-voltage converter if multiple co-channel signals require "power equalization" and the measured notch depth can reach 40dB tuning range (Figure 5.6d).

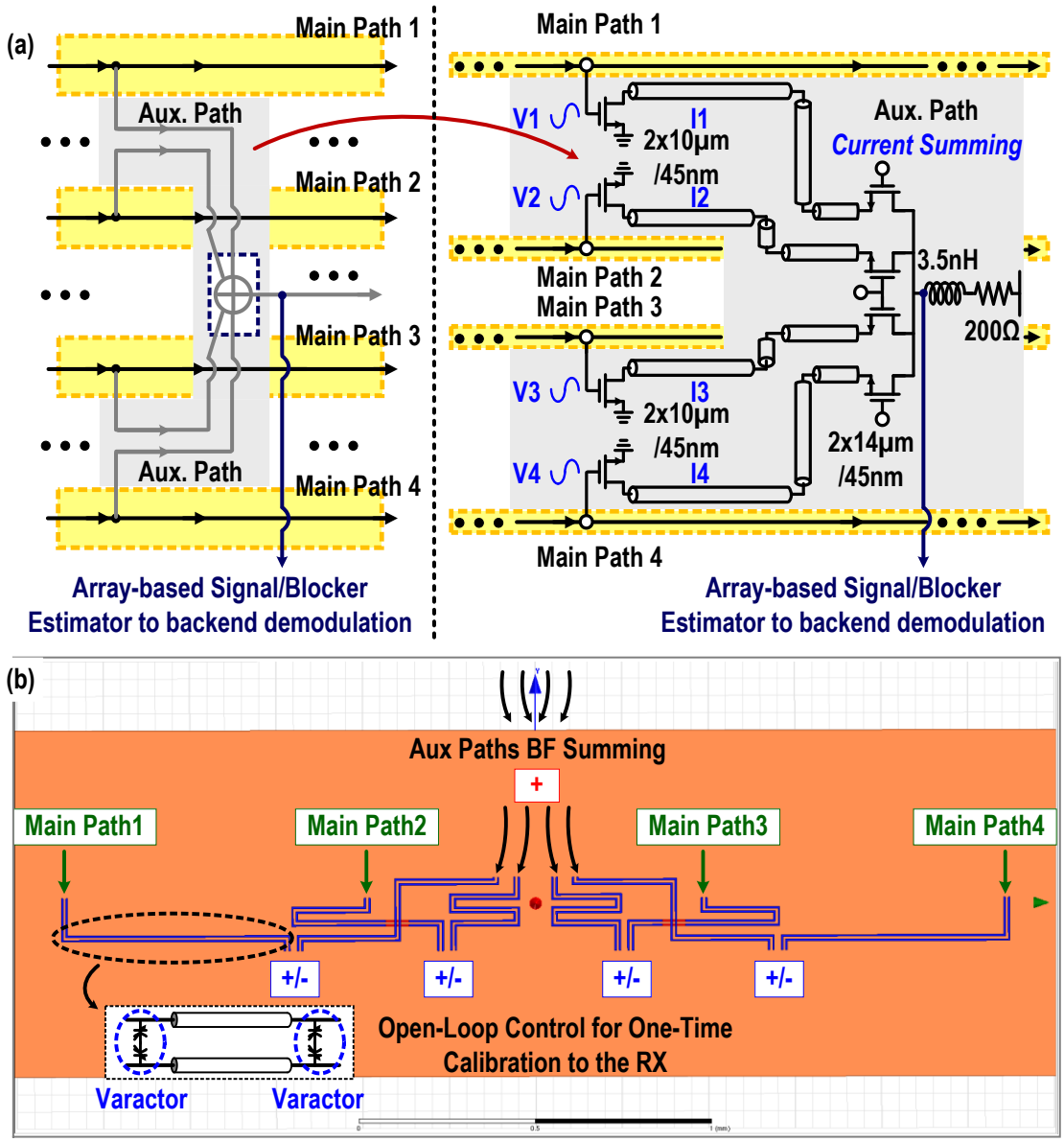

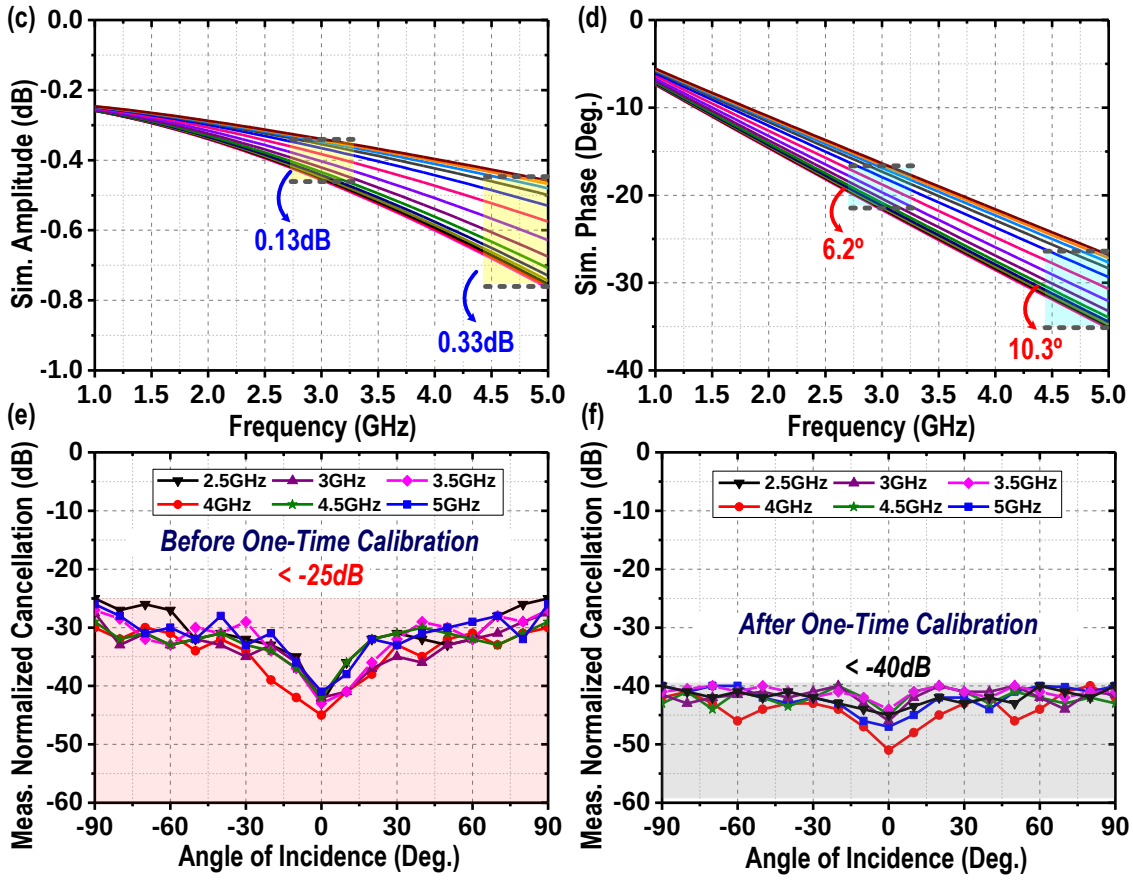

Figure 5.7 – (a) Schematic of the current-domain signal combiner for the 4-element-based BF in Aux paths. (b) 3D EM HFSS model for Main/Aux signal paths. (c) Simulated amplitude/(d)phase tuning range to compensate for component mismatch in Main/Aux signal paths. After initial one-time calibration, measured notch performance improves from (e) >25dB to (f) >40dB suppression over full FoV.

Figure 5.7a shows the detailed schematic of the 4-element-based BF in Aux paths. The voltage information (V1~V4) of four signals in Main paths are first sensed and then converted to current-domain signals (I1~I4) which are then added by a current domain combiner to achieve higher linearity. Moreover, in order to mitigate open loop feedforward PVT variation after chip fabrication, varactors are applied in each Main path (Figure 5.7b) to achieve simulated phase tuning 6.2°~10.3° with amplitude variation 0.13dB ~0.33dB (Figure 5.7c and 5.7d). After an initial one-time calibration using varactors in the

feedforward signal distribution lines, the measured notch performance of single 4-element ASF stage improves from >25dB to >40dB suppression over full FoV (Figure 5.7e and 5.7f). This initial calibration is used as constant varactor biasing voltages in all the measurement (Section 5.4).

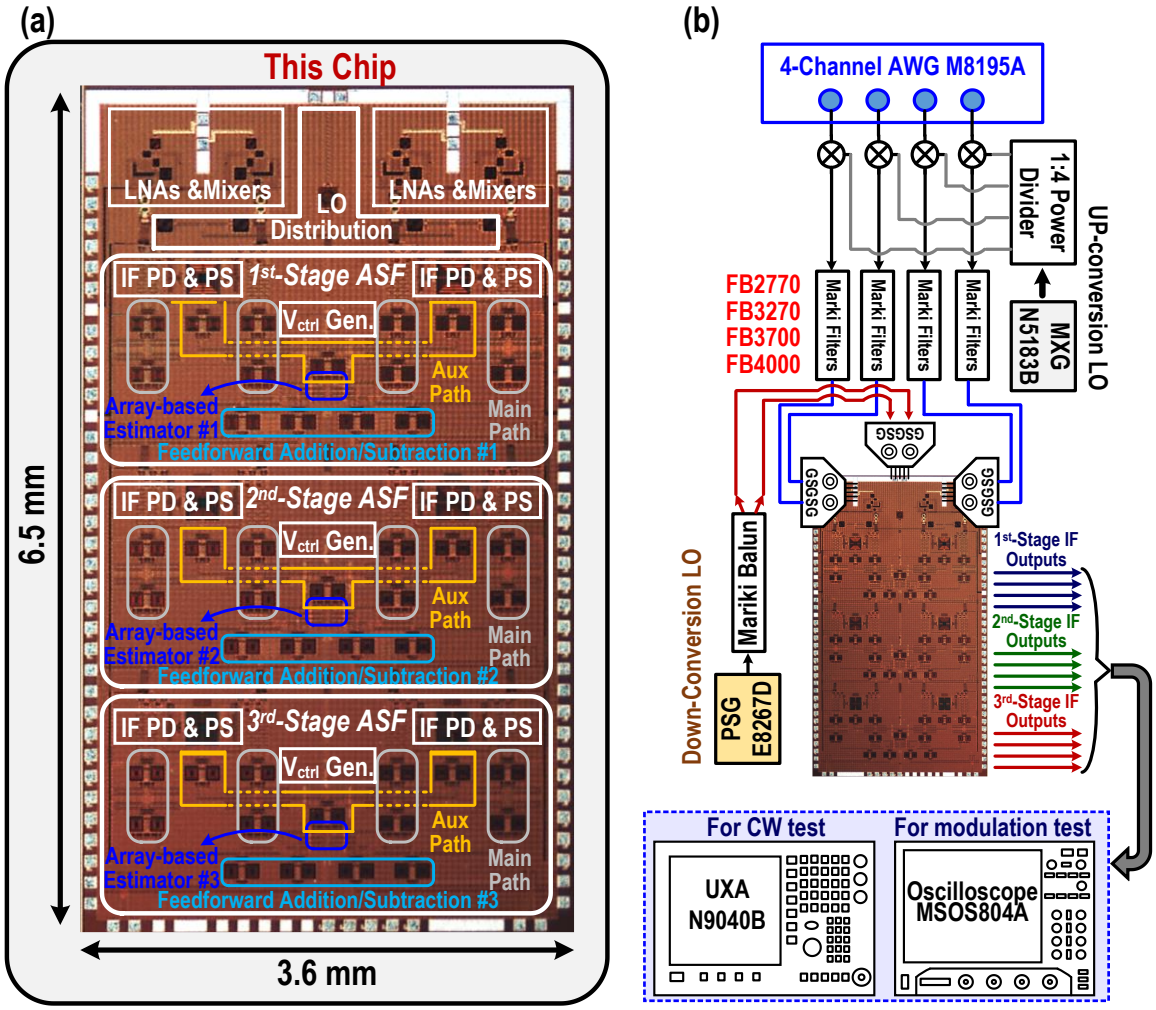

Figure 5.8 – (a) Chip micrograph and (b) its scalability for a large-scale phased array.

5.4 Experimental Results

A proof-of-concept mm-Wave 4-input-4-output MIMO RX array with 3-stage ASFs is implemented in 45nm CMOS SOI process with a total chip size of 3.6mm×6.5mm

(Figure 5.8a) [64]. The measurement setup is shown in Figure 5.8b. Multiple continuous-wave or modulated IF signals with programmable phases/amplitudes are concurrently generated by Keysignt AWG M8195A and then up-converted to mm-Wave 5G carrier as 4-channel MIMO RX array inputs with concurrent multi-signals/blockers incidence. All autonomous spatial notching or beamforming measurements are achieved only by on-chip ASFs with no external beamforming controls.

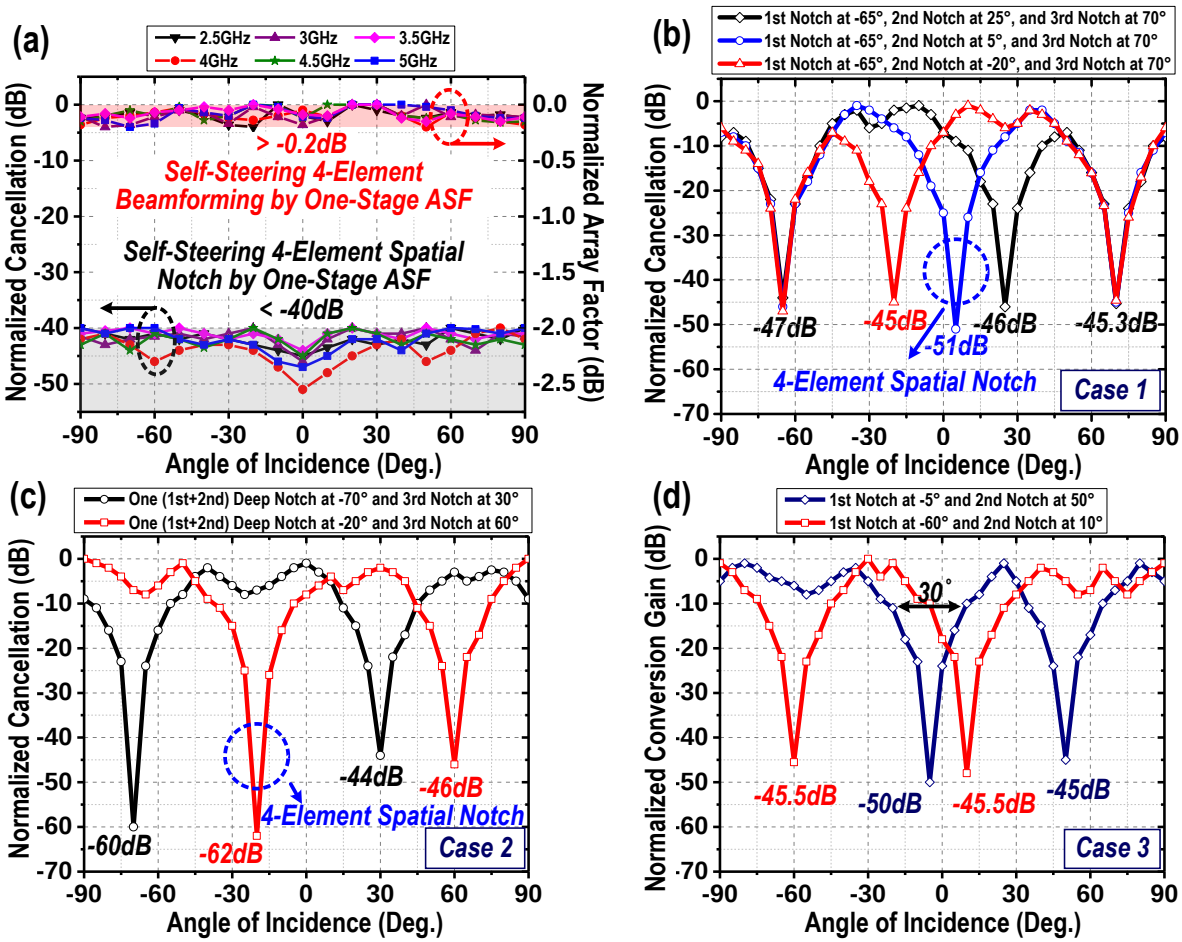

Figure 5.9 – (a) Measured single stage ASF performance over full FoV, including autonomous blocker rejection and desired signal beamforming. Measured 3-stage ASF performance in (b) case I, (c) case II, and (d) case III.

5.4.1 Continuous-Wave (CW) Measurements

The CW performances of single IF ASF stage are first characterized (Figure 5.9a). Over the full-FoV and a 2.5-5 GHz wide bandwidth, each ASF achieves a 40-51 dB spatial notch for blocker rejection (using subtractor) or a flat normalized array factor >-0.2dB for desired signal beamforming (using combiner) over full-FoV. Wideband coverage and full-FoV IF-domain ASFs support array-based high-order co-channel blockers spatial rejection (or beamforming on the desired in-band signals) without prior knowledge of carrier frequency, AoA, and modulation schemes of the incident signals or blockers. The proposed architecture can achieve instinctual management of multiple unknown signals/blockers and address the challenges in future complex EM environment.

Next, the 4-element RX array chip with cascaded 3-stage ASFs is characterized for its various operation scenarios. In case I, when both the 1st-, 2nd-, and 3rd- stage ASF use subtractors at their outputs, it creates three independent spatial notches to autonomously and sequentially suppress three unknown in-band blockers with > 40dB suppression and maximum 51dB cancellation (Figure 5.9b). In case II, if one excessively strong blocker and one moderate blocker are concurrently injected to the RX (case 2), the first two ASFs will both autonomously track the strongest blocker and suppress it twice with a total 62dB deep spatial notch, and the 3rd ASF can reject the other blocker with a 46dB notch (Figure 5.9c). The measurement in Figure 5.9d is operated in case III, when two blockers and one desired signal are simultaneously received, the 1st- and the 2nd-stage ASF are configured as the subtractors and the 3rd-stage ASF is configured as a combiner. Since the 3rd-stage ASF is for autonomous beamforming over the full FoV, its desired performance should exhibit a flat array factor over the full FoV with no spatial-domain peaks, meaning that the

ASF can track and beam-form towards incoming desired signal from any incident direction. This is different from static (non-autonomous) array, whose array factor will show one spatial-domain peak. The two similar-power blockers are sequentially suppressed by two independent spatial notches with max 50dB rejection over full FoV (Figure 5.9d). Moreover, when the desired signal is close to the spatial notch with a small signal/blocker incidence difference, the conversion gain of the desired signal is degraded due to the attenuated desired signal strength. Compared to the fixed 2-element spatial filters in [48], the proposed ASFs achieve 4-element spatial filters with sharpened selectivity that can be further improved for larger array sizes. The measurement shows our proposed system successfully relaxes the dynamic range requirement of following ADCs and enables the digital beamforming.

Additionally, the discrimination of the ASF for concurrently received multi-tones is measured. When two spatial co-channel tones are concurrently received, if the two tones have ≥1dB power difference, the power-aware PD can accurately distinguish the stronger one and achieve ≥28dB suppression (Figure 5.10a). The response time of each DSP-free array-based high-order ASF is measured using a real-time oscilloscope. Over the full FoV, the measured response time is < 1.75μs (Figure 5.10b, 5.10c), enabling fast beamforming and dynamic spatial notching for low-latency MIMOs.

The RX also achieves wideband operation from 27 to 41GHz with 36dB peak conversion gain (CG) and 15dB tuning controls to support 5G multi-band MIMOs and future complex EM environments (Figure 5.11a). The equivalent single-element double-sideband noise figure ($NF_{DSB,eq}$) [74] with the 3-stage ASF on is also measured with 4.3-6.3dB over 27-41 GHz (Figure 5.11b). The entire linearity of the RX is then measured

while exposed to blockers. With ASF off, the Pin1dB of the RX is degraded to -34/-27.3dBm under 35/25dB CG. When the 1st ASF stage is on, the measured in-band blocker-Pin1dB achieves 15/17dB improvement for 35/25dB CG (Figure 5.11c) and the measured in-band OIP3 of a desired signal performs 18/24dB enhancement for in-notch incidence at 35/25dB CG (Figure 5.11d).

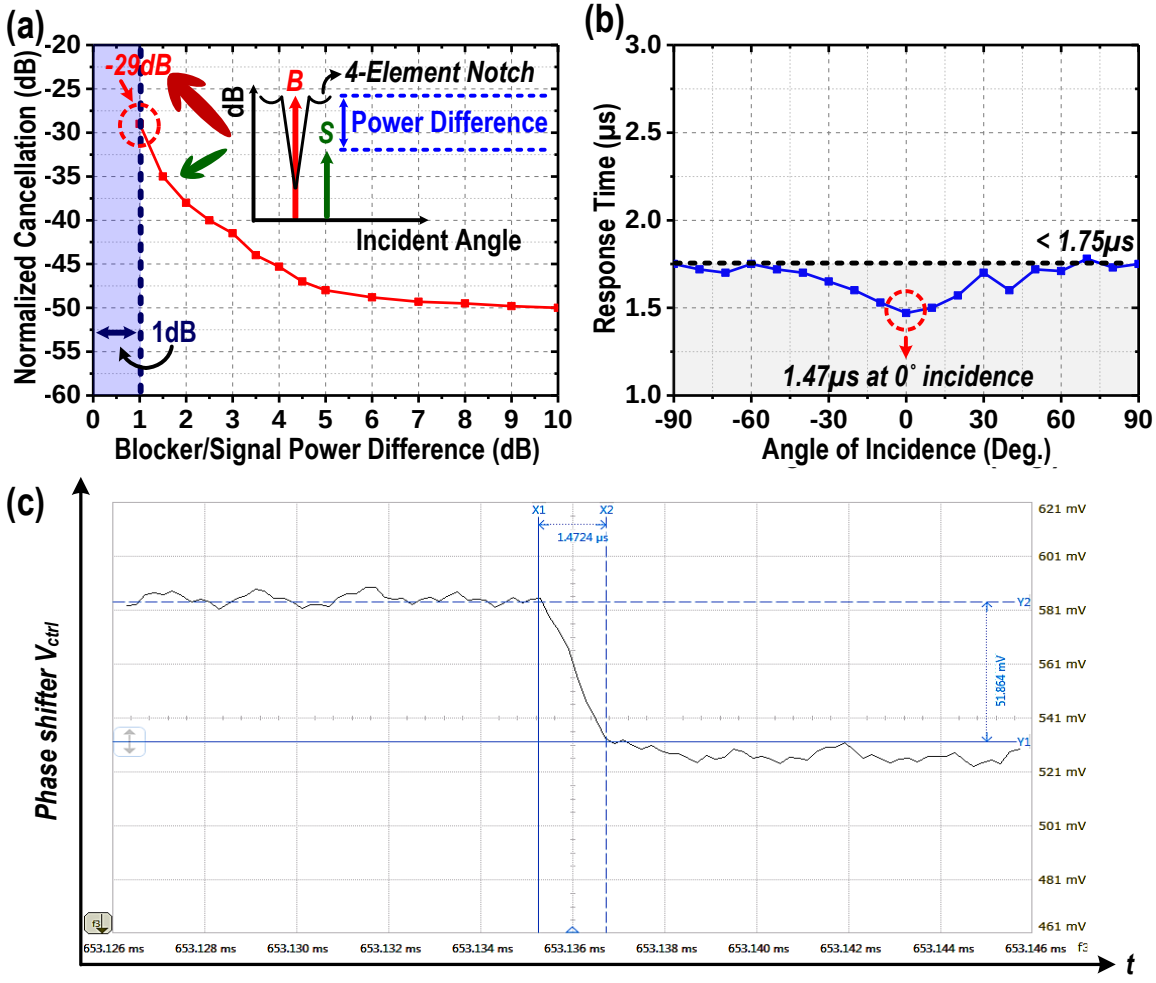

Figure 5.10 – (a) Measured ASF autonomous discrimination of concurrently received multi-tones. (b) Measured ASF response time over full-FoV. (c) Measured closed-loop response time of the SSA-BF using a real-time oscilloscope.

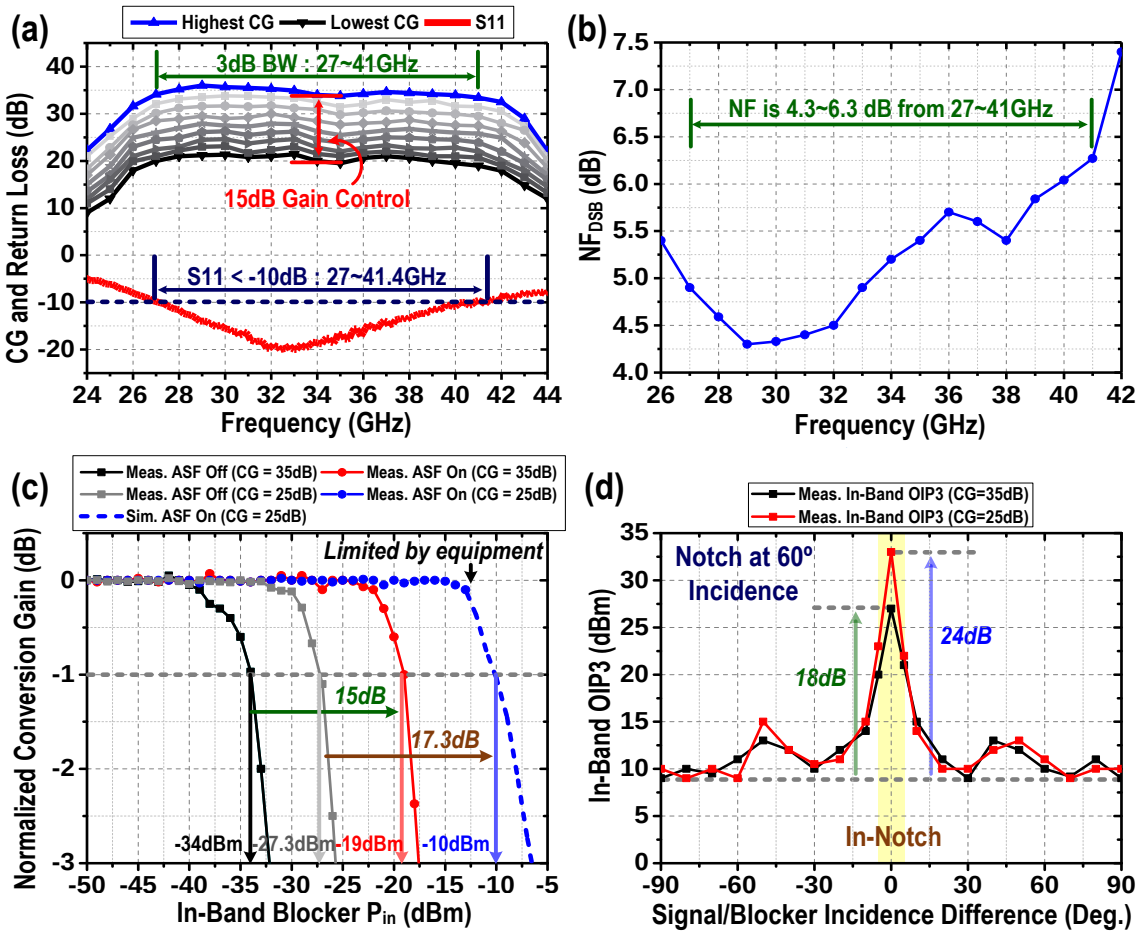

Figure 5.11 – (a) Measured wideband RX CG, S11. (b) Measured RX NF with 3-stage ASF on. (c) Measured in-band blocker Pin1dB with the 1st-stage ASF on/off. (d) Measured in-band OIP3 versus signal/blocker incidence difference.

5.4.2 Modulation Measurement

We also test the RX array under multiple (2~3) wideband modulated co-channel blockers and desired signal without any digital beamforming (case III). All the blockers/signals are independently modulated, and the blockers have various power levels (3-8dBc) to mimic practical MIMO scenarios (Figure 5.12). Multiple moderate co-channel blockers (-35~-40dBm) and a desired signal (-43 dBm) are injected and both are wideband modulated with the same modulation scheme and data rate. The blockers and the desired

signal and are first characterized with 100MSym/s 256QAM, and 200MSym/s / 500MSym/s 64QAM. They are co-channel with a signal /blocker frequency separation offset f_{offset} = 50MHz and 100M/200MHz, respectively, i.e. at least 50% frequency overlap. When the 3-stage ASF are off, the down-conversion spectra show that the blockers highly overwhelm the desired signal and the desired signal cannot be distinguished and demodulated. After enabling the 1st- and 2nd-stage ASF for array-based high-order notching to the blockers, the desired signal is autonomously beamformed at the 3rd-stage ASF and successfully demodulated for 0.8Gbit/s 256QAM with -32.7dB EVM and 3Gbit/s 64QAM with -28.64dB EVM. When the desired signal is close to the spatial notch with a small signal/blocker incidence difference, the EVM performance of the demodulated desired signal is degraded due to the attenuated desired signal strength (Figure 5.12). With a 4-element array, a clear ASF spatial signal selection is measured.

Table 5.1 compares the proposed mm-Wave MIMO RX array with the state-of-the-art designs. Compared to watt-level ADC for wideband modulations signal/blocker processing, the proposed architecture serves as a "smart" spatial filter bank with < 85mW/channel power consumption to relax dynamic requirement and enable the subsequent digital beamforming. The detailed DC power breakdown is also listed in Table 5.1, showing gradually larger DC power of the 3 cascaded ASF stages due to higher linearity requirements of the later ASF stages. By exploiting the unique N-input-N-output cascaded multistage array-based high-order ASF MIMO architecture, the RX array demonstrates a full-FoV operation with low-latency μs response time per ASF stage and achieves state-of-the-art wideband modulated multi-Gb/s 64-/256-QAM array-based high-order blocker rejection and signal BF.

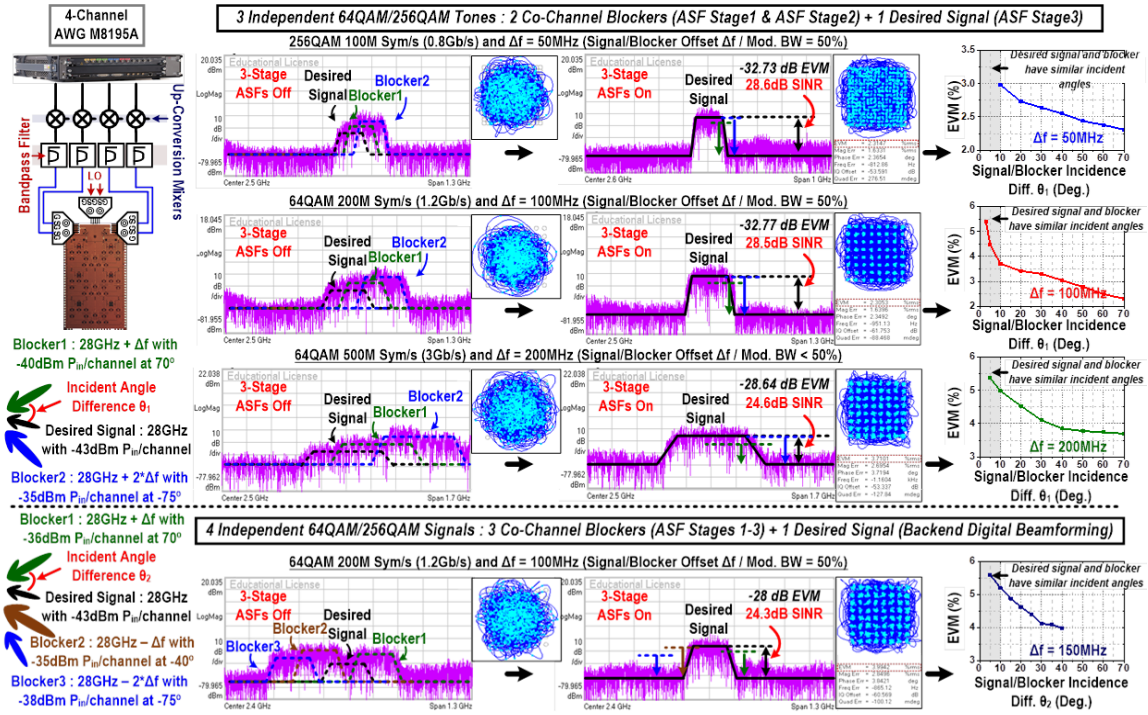

Figure 5.12 – Measured constellations and spectra of the RX with 3-stage array-based ASFs demonstrate autonomous rejection of multiple (2-3) blockers and desired signal beamforming (as case III). When the blockers and desired signal have the same broadband modulation scheme and data-rate, the 3-stage ASF shows successful demodulation of the desired signal after autonomous spatial suppression of multi-blockers.

Table 5.1 – Comparison with State-of-the-Art Spatial Notch Array RX and Mm-Wave 5G BF Array RX

	Mm-Wave 5G Beamforming RX Array						RF Spatial Notch RX Array
	This Work	M. Huang TMTT'18	W. Roh Commun. Mag.'14	B. Sadhu JSSC'17	J. Dunworth ISSCC'18	J. Pang ISSCC'19	L. Zhang JSSC'17
Functionality	MIMO Array-based ASF	MIMO SSA	MIMO	MISO	MISO	MISO	MIMO ASF
Technology	45nm CMOS SOI	130nm SiGe BiCMOS	NR	130nm SiGe BiCMOS	28nm LPRF CMOS	65nm CMOS	65nm CMOS
Frequency (GHz)	27 – 41	22 – 30	28	28	25 – 30.5	26.5 – 29.5	0.1 – 3.1
# of Inputs / Outputs	4 / 4	8 / 2	32 / NR	32 / 2	24 / 2	8 / 2	4 / 4
Conversion Gain	36dB / element	33dB / element	NR	34dB / element	34dB / 4 element	11dB / element	43dB / element
$NF_{DSB,eq}$ (dB)	4.3 – 6.3	4.2 – 6.3	NR	6[4]	4.4 – 4.8[4]	4.2	3.4 – 5.8
Beamforming	4-Element High-Order Array-based Frontend Closed Loop ASFs	2-Element Closed Loop with SSA Front-End BFs	Open Loop + Backend DSP	Open Loop + Backend DSP	Open Loop + Backend DSP	Open Loop + Backend DSP	Open Loop + Backend DSP
Blocker Rejection	4-Element High-Order Array-based Frontend Closed Loop ASFs	2-Element Closed Loop with SSA Front-End BFs	Open Loop + Backend DSP	Open Loop + Backend DSP	Open Loop + Backend DSP	Open Loop + Backend DSP	Open Loop + Backend DSP
Spatial Order of Notch	4-element (Scalable)	2-element (Fixed)	N/A	N/A	N/A	N/A	4-element
Spatial Suppression 1- / 2- / 3 Notches (dB)	62 / 50 / 51	54 / 41 / No	N/A	N/A	N/A	N/A	56 / 48.6 / 41.8
>10dB Cancellation Spatial Notch Width (Deg.) Spatial Selectivity	27˚ – 32˚	48˚ – 58˚	N/A	N/A	N/A	N/A	~30˚
Blocker Modulation Scheme	3Gb/s 64-QAM and 0.8Gb/s 256-QAM	3Gb/s 64-QAM and 0.8Gb/s 256-QAM	N/A	N/A	N/A	N/A	CW
Blocker/Signal Frequency Offset (Δf) / Modulation BW	< 50%	< 100%	N/A	N/A	N/A	N/A	>400%
# of Modulated Blockers Concurrently Received	1 or 2 or 3 (Scalable)	1 (Fixed)	N/A	N/A	N/A	N/A	2
Signal Modulation Scheme/ Polarization	3Gb/s 64-QAM and 0.8Gb/s 256-QAM	3Gb/s 64-QAM and 0.8Gb/s 256-QAM	*2.1Gb/s 16QAM	*5.16Gb/s 256QAM	*2.4Gb/s 64QAM	*6.4Gb/s 256-QAM	*2Mb/s QPSK
Signal EVM after Blocker Suppression	1.2Gb/s 64-QAM : 2.3%[1] 3Gb/s 64-QAM : 3.7%[1]	0.6Gb/s 64-QAM : 3.2%[2] 3Gb/s 64-QAM : 4.7%[2]	N/A	N/A	N/A	N/A	2Mb/s QPSK: 20.5%[3]
	0.8Gb/s 256-QAM : 2.3%[1]	0.8Gb/s 256-QAM : 2.7%[2]					
Response Time	1.47 µs	< 1 µs	45 ms	*NR*	*NR*	*NR*	*NR*
Power Consumption / RX Element (mW)	70-85 : LNA/Mixer + 3 ASFs 55-65 : LNA/Mixer + 2 ASFs	70	NR	206	42.5	112	28.5 – 36.75
Area (mm^2)	23.4	21.6	NR	165.9[4]	29[4]	12[4]	2.25

NR: Not reported. * Far-field measurement.
The modulation test is based on
[1.] 2 independent blockers + 1 desired signal and Δf / Modulation BW = 50%.
[2.] 1 blocker + 1 desired signal and Δf / Modulation BW = 50%.
[3.] 2 independent blockers + 1 desired signal and Δf / Modulation BW = 400%.
[4.] It includes its T/R switch and transmitter design.

DC Power Distribution of This Work →

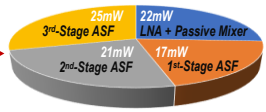

CHAPTER 6. A MM-WAVE ULTRA-COMPACT CMOS RECEIVER FRONT-END WITH CALIBRATION-FREE INSTANTANEOUS FULL-BAND IMAGE REJECTION FOR MULTIBAND 5G MASSIVE MIMO

This Chapter presents an extremely broadband 24.5-43.5GHz receiver (RX) achieving 32-56dB instantaneous full-band image rejection, which supports multiple major mm-Wave 5G bands at 24.5/28/37/39/43 GHz. A compact transformer-based I/Q network (0.14mm2) is proposed to generate high-precision LO I/Q signals at mm-Wave and provide built-in load impedance up-transformation for passive voltage amplification, boosting the LO swing for a higher RX conversion gain. The high-quality differential I/Q generation is measured with phase/amplitude variation < ±1.8˚/ ±0.15dB over an instantaneous wide bandwidth of 25-50GHz without any calibration or switching/tunable elements. The RX is measured with a peak 35.2 dB conversion gain and 18dB gain tuning to accommodate complex EM environments. The RX modulation tests successfully demonstrate receiving 18Gb/s 64-QAM and 14.4Gb/s 256-QAM signals. In addition, the RX is tested with concurrent injection of a desired signal and an image, while the image uses the same wideband modulation scheme and data rate as the desired signal. The RX successfully rejects wideband images and receives desired signals of 12Gb/s 64-QAM with -27.6dB EVM and 8Gb/s 256-QAM with -33.47dB EVM. To the best of our knowledge, this Chapter presents the first CMOS receiver frontend that covers 24.5-43.5GHz mm-Wave 5G bands and supports instantaneous full-band image rejection with no calibration,

switching/tuning elements, or external controls, enabling future wideband low-latency 5G MIMOs.

6.1 Introduction

Next-generation wireless networks require high-capacity access nodes for extremely broadband mobile links over multiple non-contiguous mm-Wave bands. For instance, 5G new radio (NR) systems [38]-[66],[113]-[115] necessitate remote radio units and user equipment to operate with multiple mm-Wave bands (e.g., at 24.5/28/37/39/43 GHz) to support multi-standard communication and international roaming. Moreover, massive multiple-input multiple-output (MIMO) and phased array architectures are extensively utilized to improve mm-Wave link performance and spatial diversity via beamforming and null-steering interference. Due to formfactor and cost requirements, to support future multi-band multi-standard communications, mm-Wave MIMO/phased arrays also demand wideband (>50% fractional bandwidth) frontends, posing challenges for multi-band transceiver frontend designs for 5G NR applications. In practice, these multi-band multi-standard 5G MIMO systems are expected to concurrently handle multiple beams/streams [39][62], i.e., multiple Gb/s 64-/256-QAM modulated signals, demanding high receiver (RX) linearity performance over wide bandwidth. High-linearity tunable-gain RXs are also necessary to avoid decorrelations among the MIMO/phased-array elements and mitigate intermodulation distortions during concurrent multi-beams/streams receiving. In addition, such extreme multi-band operations require judicious RX frequency planning to avoid image jamming, which favours built-in instantaneously wideband image rejection [49][103]-[109].

In order to create wideband I/Q signals for Image Rejection (IR) architectures, high-order RC-CR Poly-Phase Filters (PPFs) are popular for RF frequency operations. However, RC-CR PPFs at mm-Wave exhibit large signal attenuation, highly capacitive input loading, limited driving capability, and vulnerability to mm-Wave trace routings and output load variations [103][107][109][110]. Thus, their use in wideband mm-Wave LO-paths often demands more LO power to compensate for its signal loss and causes power penalty in LO drivers. Although narrow-band yet reconfigurable mm-Wave IR RXs are proposed to cover a larger bandwidth operation [62], they are inherently unable to support concurrent receiving of multiple wideband signals [103]. Recently, a 71-86 GHz RX is reported to largely reduce fractional bandwidth requirement of LO generation via bidirectional sliding-intermediate frequency (IF) Weaver architecture with only a single-stage polyphase filter, rejecting wideband Gb/s 64-/256-QAM modulated imaging signals [103]. However, multi-bit capacitor tuning banks are required for the LO RC-CR PPF to extend its operation bandwidth and to achieve wideband Image Rejection Ratio (IRR). Extensive open-loop calibrations are needed to ensure sufficient signal-to-noise ratio (SNR) and IRR, increasing reconfiguration latency and system complexity for 5G links.

To address these challenges, this Chapter presents a 24.5-43.5GHz compact RX frontend in 45nm CMOS SOI that achieves calibration-free full-band instantaneously wideband IR and supports multi-Gb/s 64-/256-QAM modulation [54]. It is composed of a mm-Wave wideband LNA, low-loss wideband transformer-based I/Q network for quadrature LO generation, differential I/Q double-balanced mixers, IF amplifiers, and a 2-stage RC-CR PPF at IF-frequency (Figure 6.1). The RX frontend is also co-designed with a T/R switch to support a complete 5G MIMO transceiver frontend. Serial-to-Parallel-

Interface (SPI) controls the RX tunable conversion gain to handle various concurrent receiving scenarios in 5G MIMOs. This Chapter is organized as follows. Section 6.2 presents the proposed system architecture. Detailed operation principles and circuit implementation are shown in Section 6.3. Section 6.4 demonstrates the measurement results and a performance comparison with reported IR RX arrays and I/Q generation.

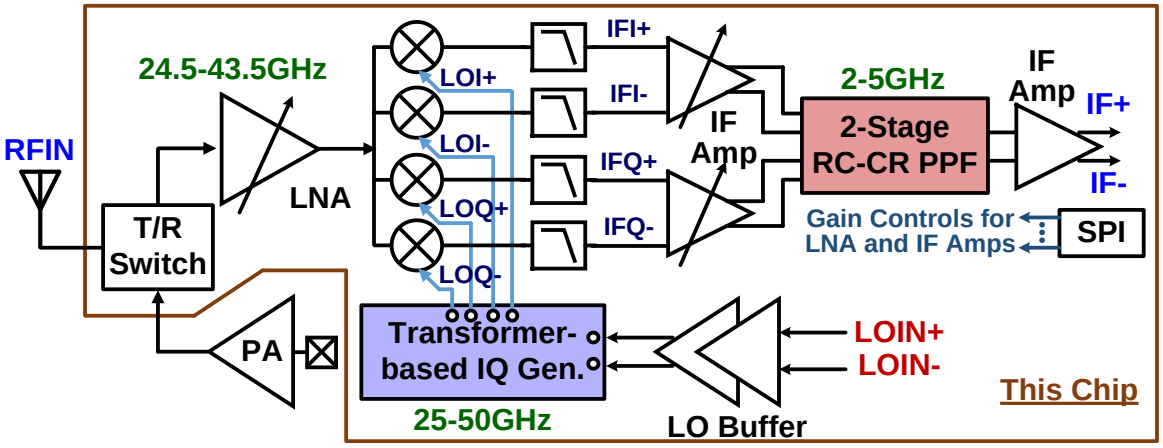

Figure 6.1 – Block diagram of the 24.5-43.5GHz RX with 32-56dB full-band instantaneous wideband image rejection.

6.2 System Architecture

The proposed wideband MIMO RX frontend with calibration-free instantaneously broadband IR architecture is shown in Figure 6.1. The RX frontend consists of T/R switch, mm-Wave broadband tunable low noise amplifiers (LNAs), and active mixers to achieve low noise figure and tunable gain to support complex EM environment scenario. The Hartley IR RX architecture with LO I/Q generation and IF I/Q combining is chosen since the active mixer conversion gain is less sensitive to LO driving amplitude mismatch [111]. High-precision transformer I/Q network achieves 20-50GHz mm-Wave LO generation, and an IF 2-stage 2-5GHz RC-CR PPF is used for IR I/Q combining. There is no tuning or

switching elements for the wideband IRR operation. SPI is used only for the LNA and IF amplifiers gain controls to adjust the RX dynamic range.

The overall RX IRR is given by the amplitude mismatch ε and phase mismatch Δθ between the I/Q paths [112] and

$$\text{IRR} = \frac{(1+\varepsilon)^2 + 2(1+\varepsilon)\cos(\Delta\theta) + 1}{(1+\varepsilon)^2 + 2(1+\varepsilon)\cos(\Delta\theta) + 1} \approx \frac{4}{\varepsilon^2 + \Delta\theta^2}, \quad (6.1)$$

assuming small ε and Δθ. In order to achieve RX IRR > 30 dB, the I/Q generation typically requires the phase and amplitude mismatch to be < ±3˚and < ±0.5 dB, respectively [103]. A high-precision mm-Wave I/Q generation is proposed as a cascaded 2-stage transformer-based poly-phase network to suppress amplitude/phase mismatches [48] with a compact size (0.14mm^2). Unlike RC-CR PPF, the transformer-based I/Q generation network is resilient to the output capacitive/resistive loading effects, and it serves a large impedance transformation with a positive voltage gain to boost the LO drive, particularly suitable for mm-Wave applications.

A proof-of-concept IR RX chip is implemented in a 45nm CMOS SOI process. Without any calibration, switching/tuning elements, or external controls, a 32-56dB full-frequency instantaneously wideband IR is demonstrated, and the RX frontend achieves an extremely broadband 24.5-43.5GHz operation, supporting multi-Gb/s 64-QAM/256-QAM and covering multiple major 5G bands at 24.5/28/37/39/43 GHz via only one RX frontend. The proposed RX has a compact size of 0.55mm×1.4mm which is much smaller than $\lambda_{air}/2$ (3.45mm× 3.45mm) of the highest operation frequency 43.5GHz, and can be readily scaled up into a large antenna array, enabling future high-capacity multi-standard 5G networks.

6.3 Operation Principle and Circuit Implementation

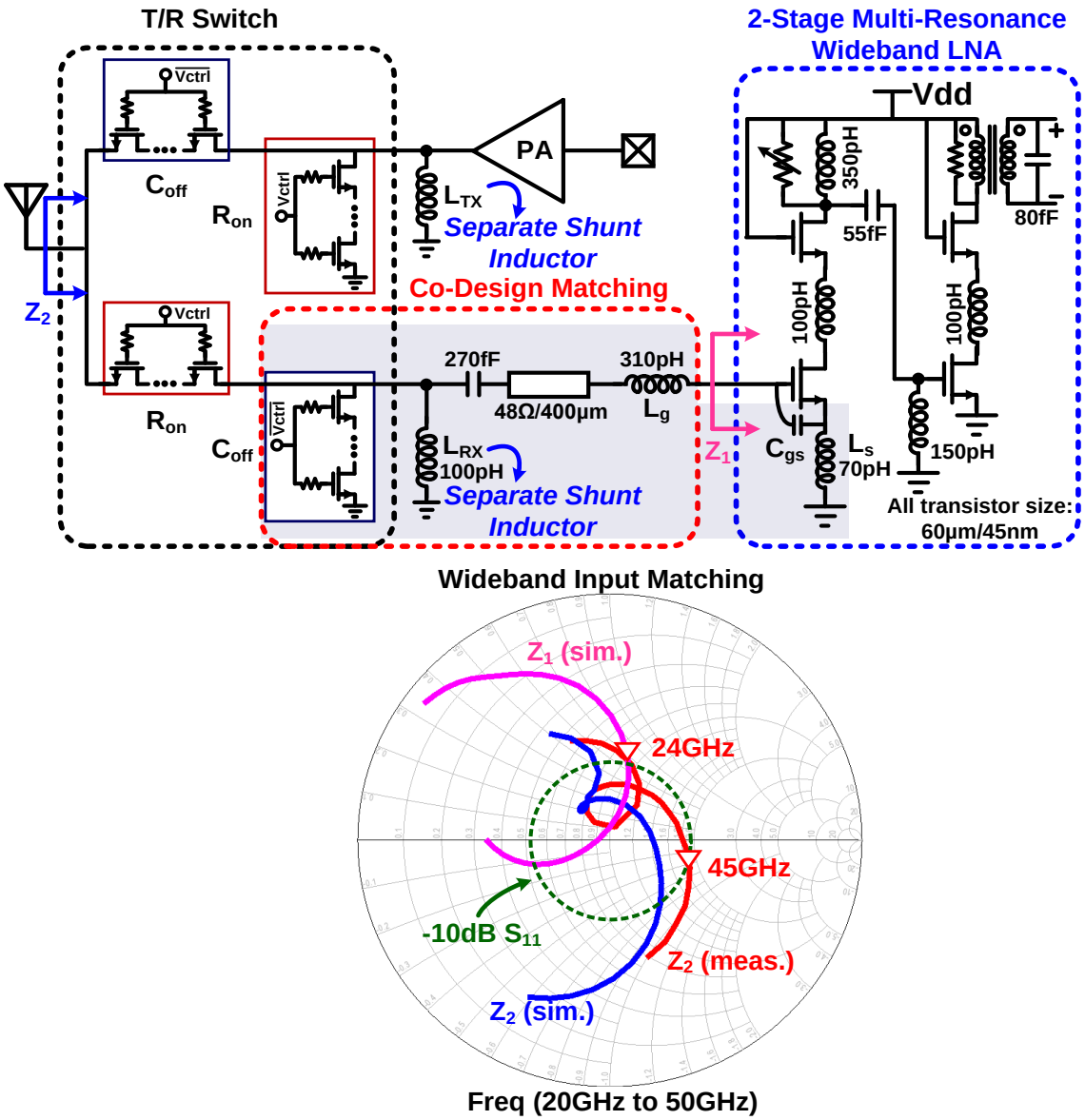

Figure 6.2 – Schematic of the 2-stage multi-resonance LNA with T/R switch co-design and simulated/measured S_{11}.

6.3.1 Mm-Wave Wideband RX Frontend

At the RX frontend, a two-stage LNA with dual resonant loads is designed to provide broadband performance (Figure 6.2). Separate shunt inductors are applied at the TX/RX

inputs to optimize TX output power and RX sensitivity. Input shunt inductor LRX in RX is applied to mitigate the loading effect of the parasitic capacitors from the T/R switch and the off-state PA. The LRX is further co-designed with gate inductor Lg, source-degenerative inductor Ls, and parasitic capacitor Cgs of the first-stage LNA to create a high-order wideband input matching network (Figure 6.2), converting the one-resonance Z1 of the LNA input to a multi-resonance Z2 in front of the T/R switch. The proposed RX frontend is measured with a broadband input matching S11 from 24 to 45 GHz. Tunable load of the first-stage LNA is controlled by SPI to achieve different gain settings for practical receiving scenarios. An output transformer balun absorbs the loading effect from following the differential I/Q double-balanced mixers and serves as a balanced differential signal generation.

6.3.2 Calibration-Free Ultra-Wideband LO I/Q Generation

For the LO driving in differential I/Q double-balanced mixer, the mm-Wave transformer-based I/Q network is designed to convert one differential LO input to two balanced well-matched differential I/Q LO outputs with compact size and low loss over an extremely wide bandwidth [48]. The proposed transformer-based I/Q network is designed based on a 2-stage cascaded self-similar 90 degree hybrid coupler as a one-inductor-footprint I/Q transformer and 3D EM HFSS model is shown in Figure 6.3[66]. The phase/amplitude mismatch is highly suppressed by cascading multiple stages of transformer-based 90 degree hybrid coupler units [48][66][77] and a proof-of-concept 2-stage transformer-based I/Q is proposed to achieve high-accuracy I/Q generation over 20-50GHz. Simulated one-stage and two-stage transformer-based differential I/Q networks are then compared in Figure 6.3. With nominal 50Ω load terminations at the two

differential I/Q LO outputs of both I/Q networks, the two-stage transformer-based I/Q design achieves nominal IRR > 35dB over 20-50GHz, which is much better than a single-stage transformer I/Q network that does not support sufficient IRR over the wide 20-50GHz bandwidth (Figure 6.3). Next, to verify the design robustness, the proposed transformer-based I/Q generation network is simulated under ±30% load variation. The peak IRR frequency of the single-stage design varies significantly and it is still narrow band. However, the peak IRR frequency is stable at 35GHz and the two-stage design shows a robust IRR response across 20-50GHz. Over broadband 20-50GHz and load variation, the two-stage transformer-based I/Q network design substantially improves the I/Q generation accuracy with at least > 35.2 dB IRR, critical for wideband high-performance IR RX designs.

The detailed equivalent schematic of the two-stage transformer-based I/Q network is shown in Figure 6.4a. It can serve as a two-stage impedance transformation and the isolation terminations are loaded with 50Ω to ground to provide better power handling and I/Q amplitude balance (Figure 6.4b). Two test structures are implemented in 45nm CMOS SOI to evaluate the I/Q generation network performance, each with the differential I or Q outputs terminated using on-chip 50Ω to allow probing test on the other I or Q outputs (Figure 6.4b). With standard 50Ω probing, the measured I/Q amplitude imbalance is <±0.15dB and I/Q phase mismatch is <±1.8˚ over 25-50GHz (Figure 6.4c). In Figure 6.4c, the measured passive loss of the two-stage transformer-based I/Q network is only 2.1dB at 35GHz in additional to the 6dB inherent loss due to 1-to-4 power splitting from the differential input to the four single-end I+/I- and Q+/Q- outputs.

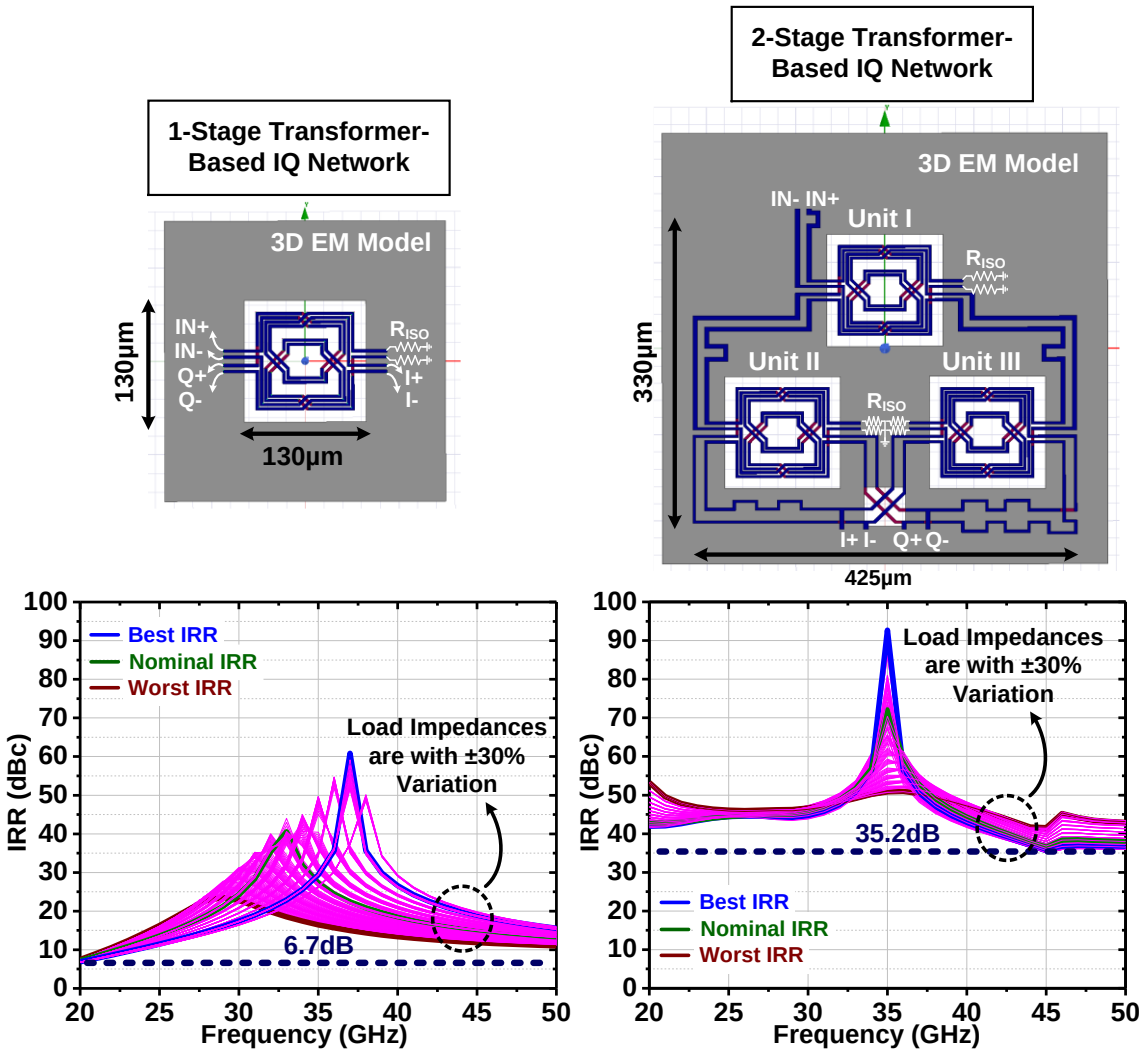

Figure 6.3 – Simulated IRR of the 1-/2-stage transformer-based I/Q network under +/- 30% impedance variation. The 2-stage transformer-based I/Q network achieves >35.2dB IRR over 20-50GHz, showing its superior bandwidth and robustness.

To drive the high impedance (~500 Ω) at the LO ports of the I/Q double balanced mixers, the transformer-based I/Q generation network is designed to accommodate large load impedance and still preserves high-precision I/Q generation. Moreover, the low-loss transformer-based I/Q generation network naturally realizes impedance up-scaling from its 50Ω input to 500Ω load at the I/Q mixer LO ports, which thus achieves passive voltage amplification of the LO waveforms to mitigate large LO power requirement at mm-Wave.

Simulated passive voltage gain of the proposed two-stage transformer I/Q generation network versus different loads (R_L) is shown in Figure 6.4d and Figure 6.4e. At 35GHz, the simulated passive voltage gain of the proposed I/Q network is largely improved from -8dB for standard 50Ω loads to -3.69dB of 10000Ω load, showing a +4.31dB gain enhancement (Figure 6.4e). For the actual mixer LO port loads of R_L~500 Ω, the achieved passive voltage gain is -4dB with 4dB enhancement. Note that considering the inherent 6dB 1-to-4 power splitting loss, the proposed transformer I/Q generation network actually achieves a passive voltage amplification gain of 2dB, which enhances the mixer conversion gain that is highly dependent on LO swing (Figure 6.4f).

With the built-in impedance transformation, simulation shows the input matching of the transformer I/Q generation network preserves S_{11} < -10dB from 25-50GHz, showing a strong isolation and tolerance to output loading effect (Figure 6.4g). Moreover, with RL of ~500Ω, 4.1dB LO swing enhancement is achieved compared to RL=50 scenario and the passive loss is 2.8-5dB with 1-3.2dB voltage gain over 25-50GHz. High-precision differential I/Q generation is still preserved with < ±0.09dB amplitude imbalance and < ±1.9˚ phase mismatch over 25-50GHz with no calibration or tuning/switching element. These results achieve a low-loss mm-Wave differential I/Q LO generation with a very compact size (0.14mm^2) and the state-of-the-art instantaneously wide bandwidth.

In addition, the capacitors in Figure 6.4a are realized by co-designing the coupling and parasitic capacitors in the transformer couplers and their connecting traces. These effective capacitors are defined by the lithograph of top metal layers and thus are well captured in the 3D EM simulations by HFSS. Compared to using physical capacitors,

absorbing them into the transformer-based I/Q generation network is more robust against device process variations.

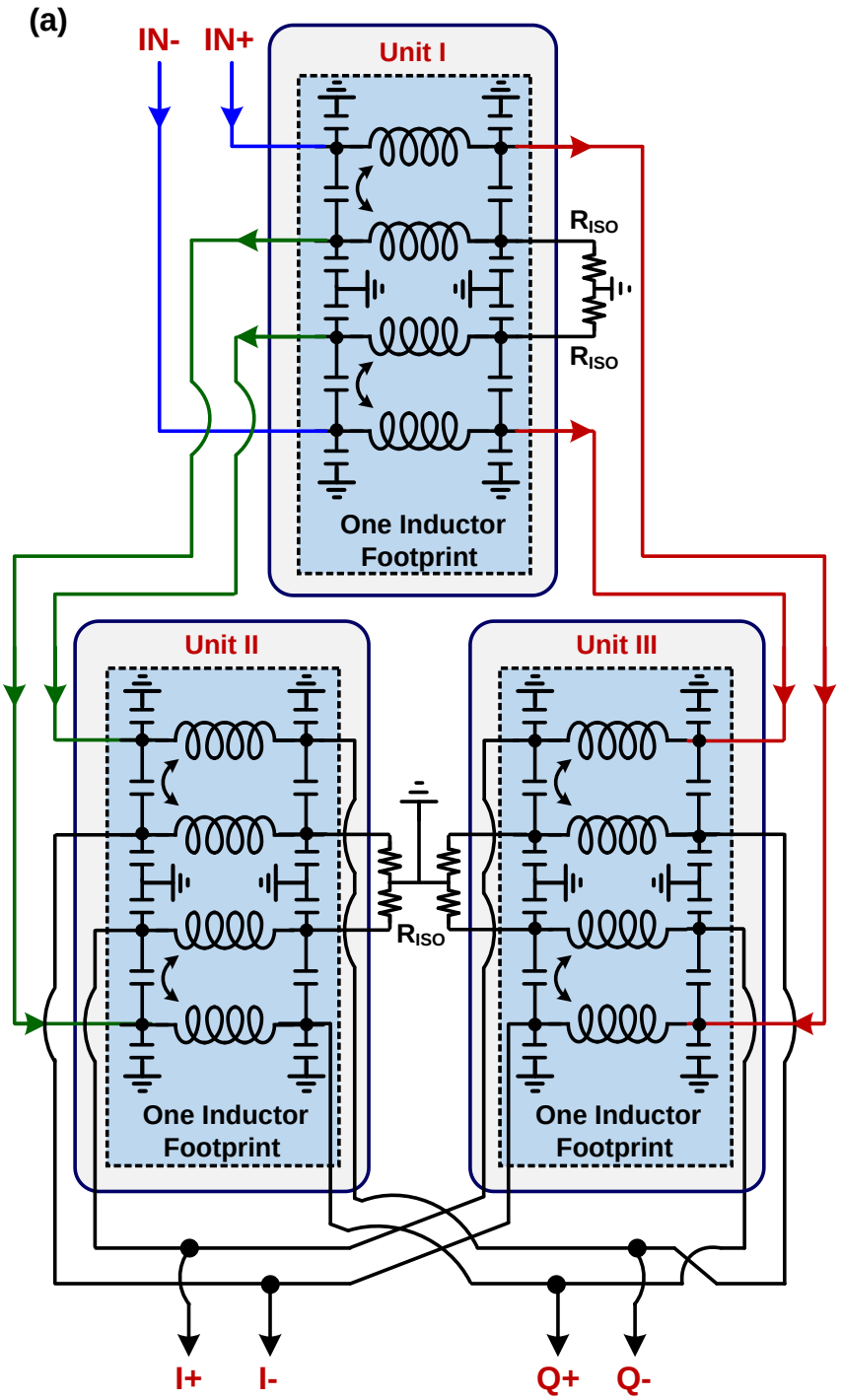

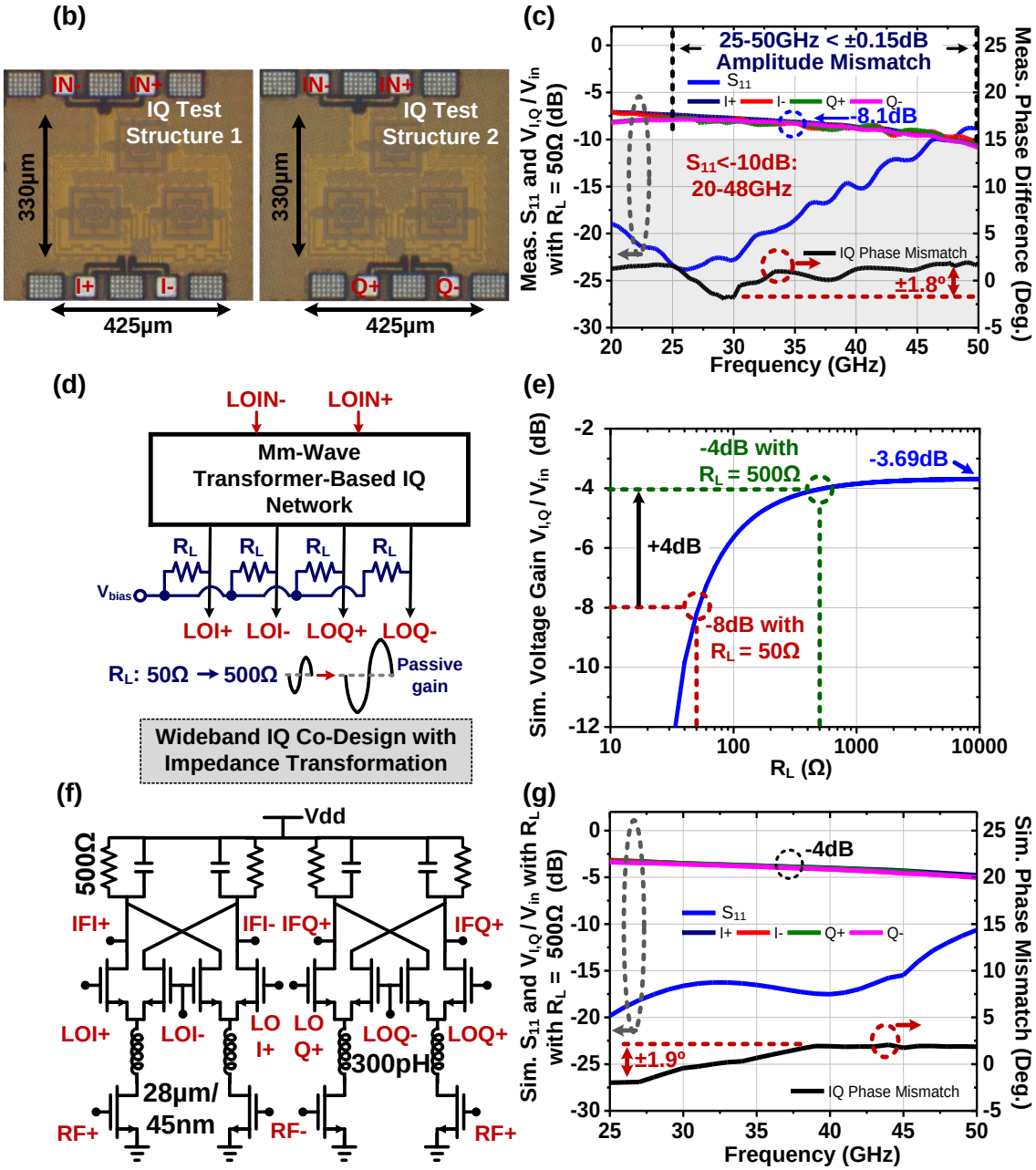

Figure 6.4 – (a) Schematic, (b)Two test structures with differential I or Q terminated with on-chip 50Ω, and (c) Measurement results of the wideband low-loss transformer-based IQ network. (d) Conceptual diagram and (e) simulation of the passive gain amplification. (f) Schematic of the IQ double balanced mixer. (g) Simulation results with R_L = 50Ω. R_L = 500Ω is used when integrating with mixer to provide passive voltage amplification.

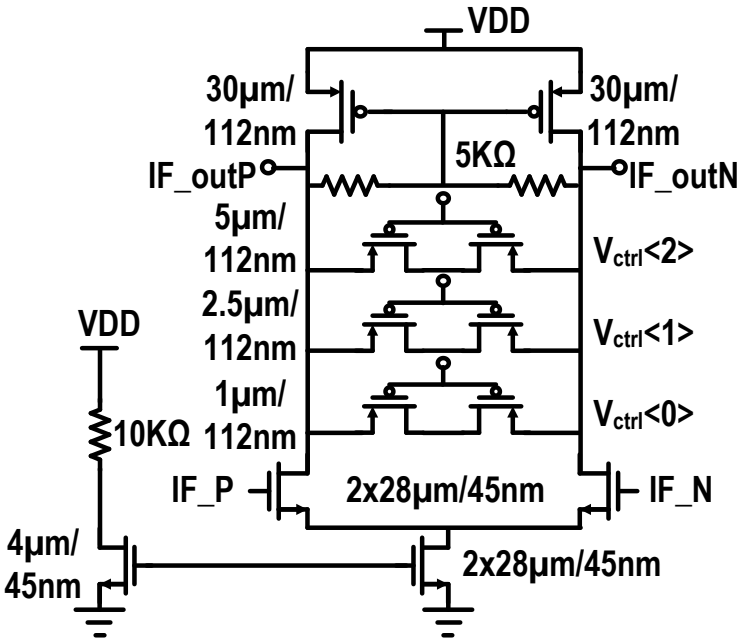

Figure 6.5 – Schematic of IF amplifier with variable gain controls.

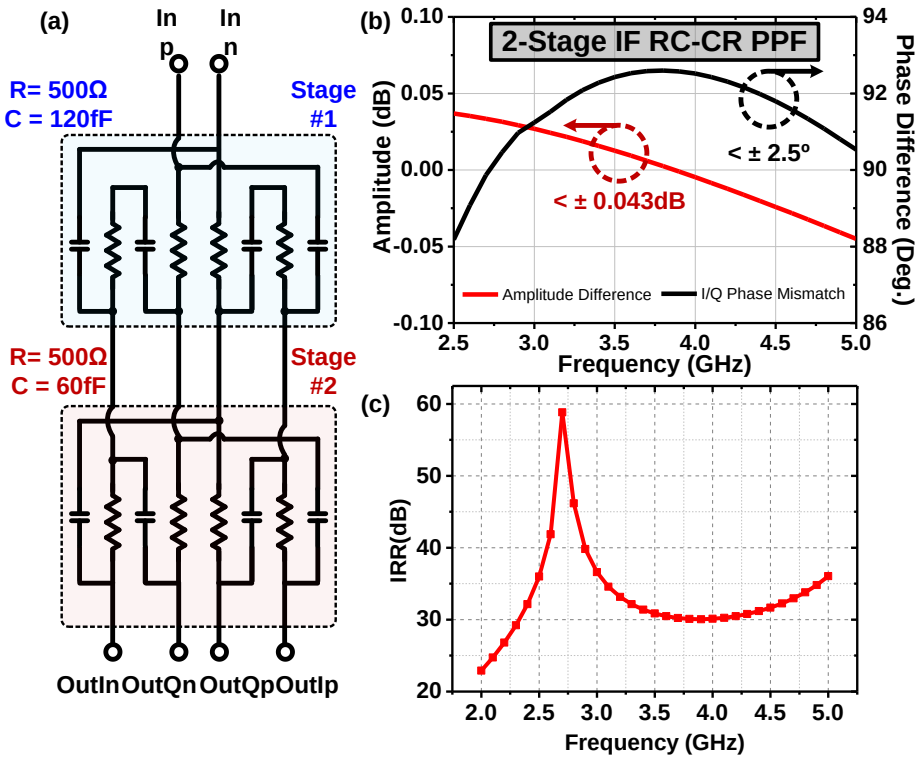

Figure 6.6 – (a)Schematic of the 2-stage RC-CR PPF. (b) Simulated amplitude mismatch, phase difference, and (c) IRR of the RC-CR PPF.

6.3.3 Variable-Gain IF Amplifier and IF I/Q Generation

After down conversion, the I/Q double balanced mixers are followed by the IF variable-gain amplifier (VGA) and IF RC-CR PPF. Figure 6.6 shows the schematic of the IF differential VGA consisting of a differential pair with 3-bit PMOS bank as resistive load to realize gain controls. Next, a two-stage RC-CR PPF is utilized to complete the IR at the IF frequency (Figure 6.6a). Simulated I/Q amplitude imbalance of the RC-CR PPF is $<\pm 0.043$dB and I/Q phase mismatch is $<\pm 2.5^{\circ}$ with an intrinsic IRR of 30-58.8dB over a wide IF bandwidth of 2.5-5GHz (Figure 6.6b and 6.6c). The simulated IF RC-CR PPF IRR is 30-59dB over 2.5-5GHz.

The measurements in Section 6.4 will demonstrate that the RX achieves multi-Gb/s 64-/256-QAM modulated and instantaneous IRR over the entire 24.5-43.5GHz without any I/Q calibration or tunable settings.

6.4 Measurement Results

A proof-of-concept broadband 24.5-43.5GHz compact IR RX with calibration-free full-frequency instantaneously wideband IR is implemented in 45nm CMOS SOI process with a total chip size of 0.55mm×1.4mm (Figure 6.7a) [54], which is compact and could be easily applied for a large-scale phased array/MIMOs. The measurement setup is shown in Figure 6.7b. Multiple continuous-wave or wideband modulated IF signals are concurrently generated by Keysight AWG M8195A and then up-converted to mm-Wave 5G carrier as multiple concurrent input signals, desired signals and image signals, to the RX. Multiple Marki bandpass filters are used to filter out the external up-conversion LO leakage signal. Keysight spectrum analyzer and oscilloscope captures continuous-wave

and demodulation results. All IR measurements are achieved only by the on-chip mm-Wave and IF I/Q generation with no external calibration/ tuning/switching controls.

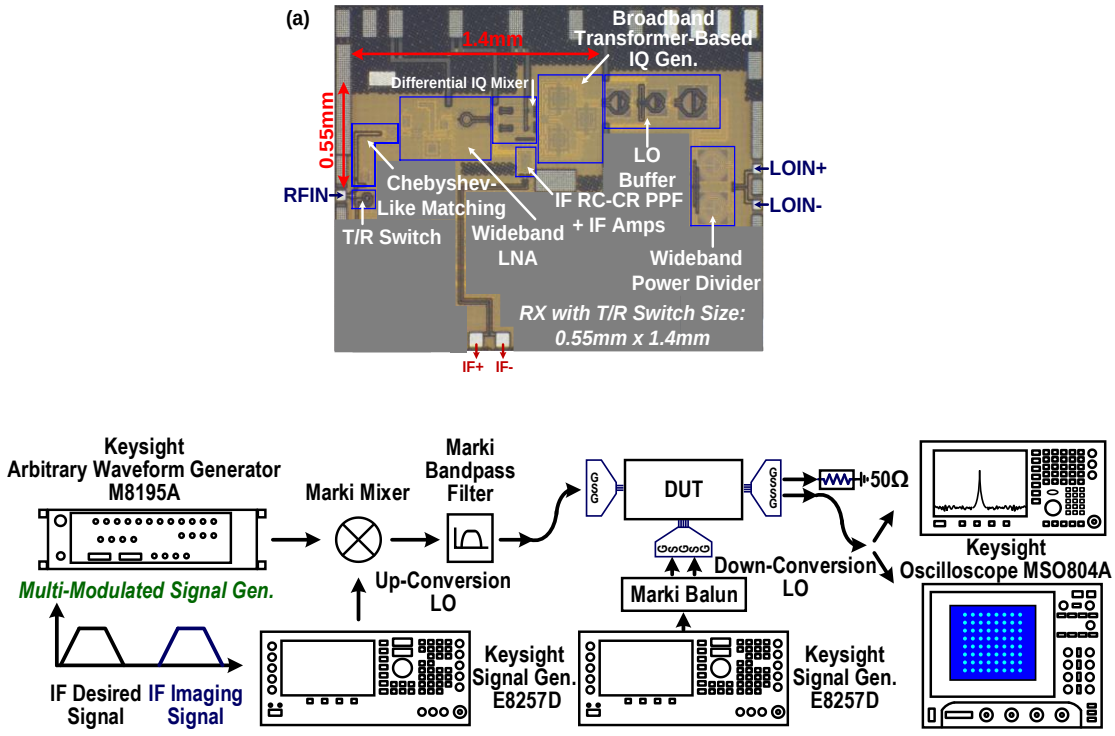

Figure 6.7 – Chip micrograph. (b) Measurement setup.

6.4.1 Continuous-Wave Measurements

The RX is first tested for its continuous-wave performance. Measured S_{11} < -10dB is achieved from 24.1 to 44.4GHz because of the wideband T/R switch matching co-design. The 3-dB conversion gain bandwidth is achieved from 24.5 to 43.5GHz with a state-of-the-art 56% fractional bandwidth, covering the major multiple 5G mm-Wave bands (24.5/28/ 37/39/43GHz) (Figure 6.8a). The RX is measured with a peak conversion gain 35.2dB with 18dB gain control, offering a wide dynamic range of RX linearity to facilitate concurrent multi-signal receiving scenario in the complex EM environment of future massive MIMOs. The down-converted IF signal shows a flat conversion gain with <1dB

variation up to 4.7GHz (Figure 6.8b), enabling a wideband multi-Giga Symbol/s demodulation.

Then, the noise figure is measured to be 3.2-6.1dB for RX-only test structure without the T/R switch. With extra signal loss 1.3~2.1 dB from the switch, the overall noise figure of the RX is degraded to 5.3-7.4dB over 24.5-43.5GHz (Figure 6.8c). Figure 6.8d presents the measured input IIP3 and IP1dB of the RX with 18dB gain tunability. It achieves +0.5dB/-17.3dBm IIP3 and -8.25/-27.25dBm IP1dB under the lowest/highest gain setting, i.e. 17/35dB RX conversion gain at 28GHz, respectively (Figure 6.8e). The RX linearity is also measured for the major 5G bands, showing 16.5-20.5dB IP1dB improvement with the 18dB gain tuning (2dB/step) for high-linearity MIMO (Figure 6.8f).

Next, to test IR, a continuous-wave desired signal and an image tone are together sent to the RX (Figure 6.9a). For the desired input signal over the major 5G bands, a state-of-the-art wideband 30-56dB IRR is achieved over wideband IF frequency 3-5GHz, showing that the proposed RX supports wideband modulated multi-Giga Symbol/s image signal rejection and provides enough SNR for potential 64-/256-QAM demodulation. With a fixed IF at 3.5GHz (Figure 6.9a), the RX demonstrates an instantaneously full-frequency 23-44GHz 32-56dB IRR. Again, no calibration or tuning/switching element is used in these continuous-wave IRR tests.

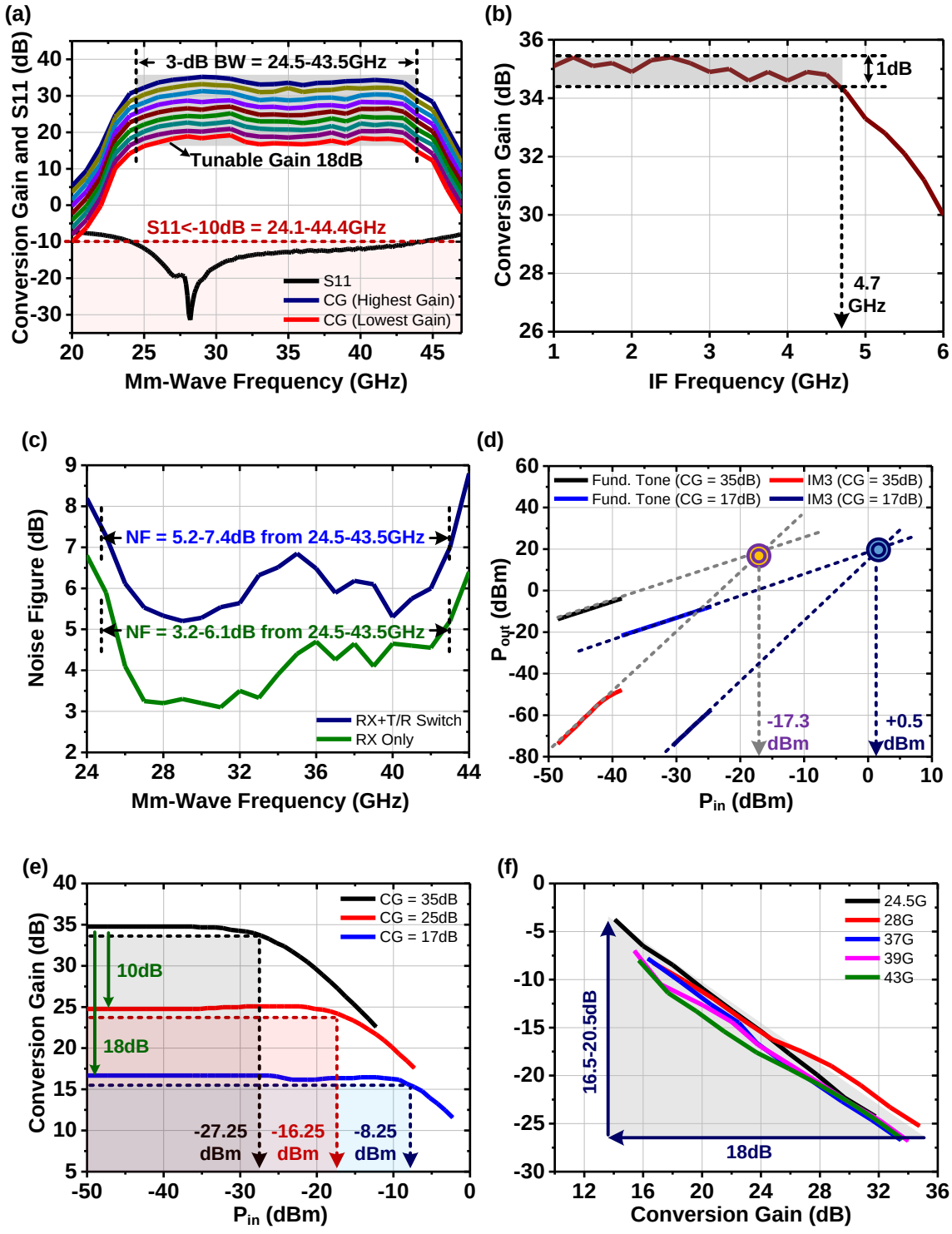

Figure 6.8 – (a) Measured input matching and (b) tunable conversion gain (CG) versus mm-Wave/IF frequency. (c) Measured noise figure (NF) with/without T/R switch, (d) IIP3, and (e)-(f) IP1dB under various gain settings.

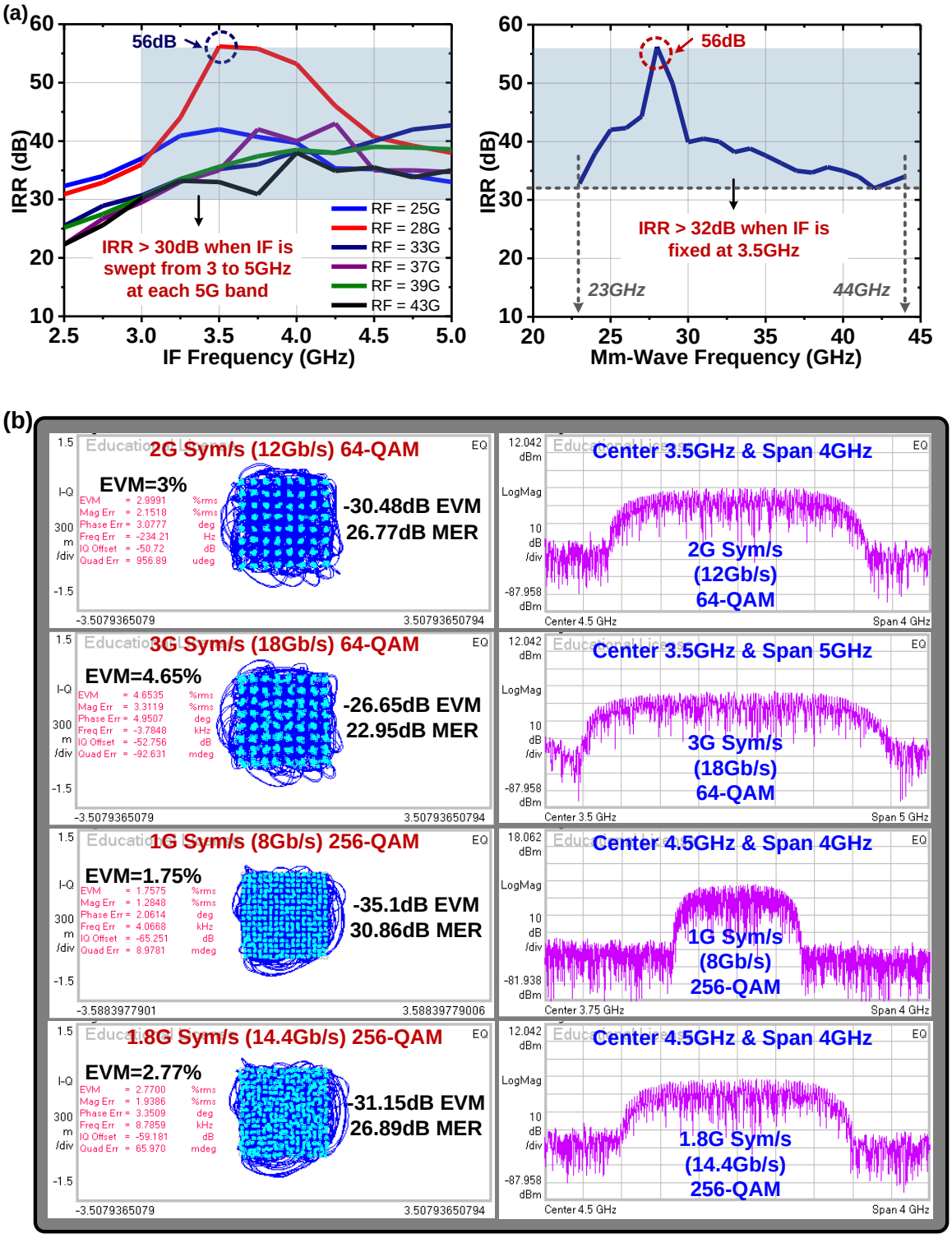

Figure 6.9 – (a)Measured IRR versus IF/mm-Wave frequency. (b)Measured constellations and spectra for wideband modulated 64-/256-QAM desired signals.

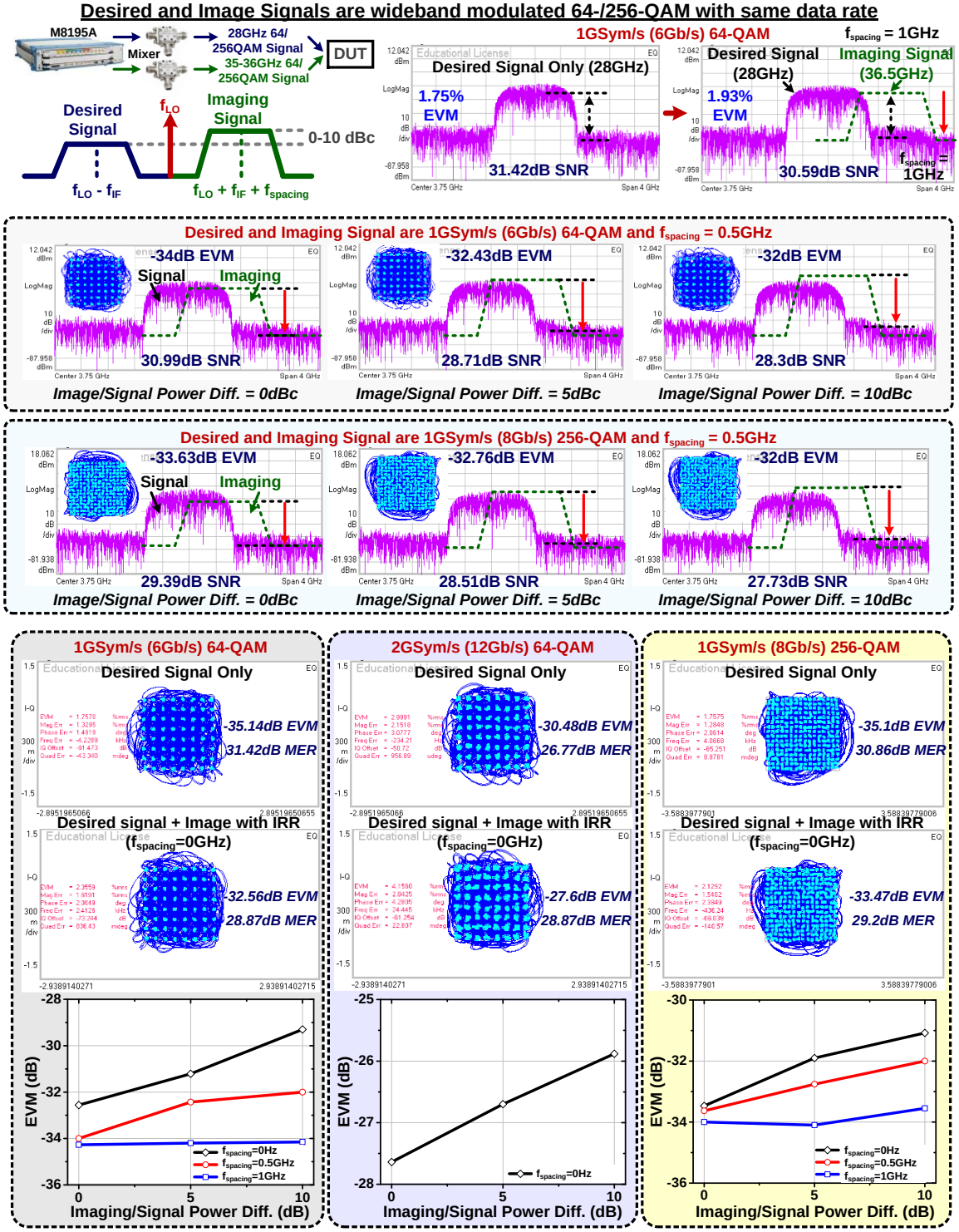

Figure 6.10 – Measured constellations and spectra with the concurrent wideband modulated 64-/256-QAM image signals at different power levels. Wideband modulated 64-/256-QAM image rejection is demonstrated and the desired signal is successfully demodulated even with 10dB larger image signal.

6.4.2 Modulation Measurements

Next, the RX is tested with wideband modulated 64-/256-QAM signals. For only the desired signal, it supports a state-of-the-art 12/18Gb/s 64QAM with -30.48/-26.65dB EVM as well as 8/14.4Gb/s 256QAM with -35.1/-31.15dB EVM (Figure 6.9b), supporting future enhanced mobile broadband 5G MIMO.

To evaluate imaging rejection during wideband modulation operation, one mm-Wave wideband modulated desired signal is at frequency f_{LO} - f_{IF} and its image signal is at f_{LO} + f_{IF} + $f_{spacing}$, which are sent simultaneously to the RX with the same input power level, modulation scheme, and data rate (Figure 6.10). The $f_{spacing}$ is set as signal/image frequency separation offset only for IF spectrum illustration purpose. First, as $f_{spacing}$ = 1GHz, the RX is tested with desired signal at 28GHz, LO at 31.75GHz, and image signal at 36.5GHz. After down-conversion, the spectrum shows a clear wideband modulated IR with at least > 30dB suppression and the residual image signal is close to noise floor, and the desired signal is successfully demodulated for 6Gb/s 64QAM with -34.3dB EVM. Compared to wideband modulated desired signal only, the SNR of the desired signal only degrades slightly from 31.42dB to 30.59dB.

The RX is next measured with concurrent wideband modulated 64-/256-QAM image signals at different power levels and $f_{spacing}$. It shows EVM degradation on the demodulated desired signal due to lower SNR and larger spectra overlap (Figure 6.10). It is also tested with an extreme case $f_{spacing}$ = 0Hz, i.e., the wideband modulated image tone and desired signal are completely overlapped after down-conversion (Figure 6.10), the desired signal shows a clear constellation and is successfully demodulated for 6/12Gb/s 64QAM with -

32.56/-27.6dB EVM and 8Gb/s 256QAM with -33.47dB EVM, which is degraded from 6/12Gb/s 64QAM with -35.14/-30.48dB EVM and 8Gb/s 256QAM with -35.1dB EVM for desired signal only respectively. High SNR after demodulation is achieved and the RX demonstrates a first-ever broadband multi-Gb/s 256QAM IR, enabling future enhanced data-rate 5G NR.

Also, the RX is tested under various input power of the wideband modulated image signal. When $f_{spacing}$ is 0.5GHz and gradually larger image signal power level 0~10dBc, the desired signal is demodulated with the degraded EVM from -34dB (0dBc), -32.43dB(5dBc), to -32dB (10dBc) in 6Gb/s 64QAM and from -33.63dB (0dBc), -32.76dB(5dBc), to -32dB (10dBc) in 8Gb/s 256QAM. When $f_{spacing}$ is 0Hz, the desired signal can still be successfully demodulated for 6/12Gb/s 64QAM with -29.3/-25.88dB EVM and 8Gb/s 256QAM with -31.1dB EVM with 10dB larger image signal, demonstrating a state-of-the-art mm-Wave instantaneously wideband GHz IR. Again, no calibration or tuning/switching element is used in these wideband modulation IRR tests.

Table 6.1 – Comparison with State-of-the-Art Mm-Wave RX and I/Q LO Generation

	Mm-Wave Full Receiver					*Mm-Wave LO Generation / IQ Mixer*				
	This Work	S. Mondal ISSCC'18		N. Ebrahimi JSSC'18	J.-Y. Hsieh TMTT'16	F. Piri JSSC'18	B. Welp TMTT'18	M. Frounchi TMTT'18	D. Zhao JSSC'15	W.-H. Lin, TMTT'13
BW (GHz)	**24.5-43.5 / 25-50[a]**	27-29.75	35-38.75	71-86	60	28-44	12.5-23[c]	41-74	62.5-85.5	64-84
Fractional BW (%)	**56 / 66.7[a]**	9.7	10.2	19.1	N/A	44	59.2	57.4	31	27
Conversion Gain (dB)	**35.2**	33	26.5	0	20	N/A	N/A	5.5	<10[d]	0[d]
Gain Control Tuning (dB)	**18**	N/A		6	5	N/A	N/A	N/A	N/A	N/A
IRR (dB)	**32-56**	35		30	33.9	40-44	>26[c]	>29	30-47	40
External Controls for IRR	**No**	No		Yes	No	No	Yes	No	Yes	No
Frequency Spacing for Signal and Image	**0Hz**	60MHz		2GHz	N/A	N/A	N/A	N/A	N/A	N/A
Signal Modulation Data Rate (EVM) After Image Rejection	**12Gb/s 64-QAM (-27.6dB)** **8Gb/s 256-QAM (-33.5dB)**	Continuous Wave		9Gb/s 64-QAM (-28.3dB)	Continuous Wave	Continuous Wave	Continuous Wave	Continuous Wave	Continuous Wave	Continuous Wave
Signal Only Modulation Data Rate (EVM)	**18Gb/s 64-QAM (-26.7dB)** **14.4Gb/s 256-QAM (-31.2dB)**	Continuous Wave		N/A	Continuous Wave	Continuous Wave	Continuous Wave	Continuous Wave	4.5Gb/s 64-QAM (-24dB)[d]	0.04Gb/s 256-QAM (-34dB)
IP_{1dB} (dBm)	**-7 to -25.5**	-23 to -30		N/A	-25.2 to -22.5	N/A	N/A	N/A	N/A	N/A
NF (dB)	**3.2-6.1 / 5.3-7.4[b]**	5.7-8.5		>14	8.9-10.8	N/A	N/A	N/A	N/A	N/A
Power Consumption (mW)	**60**	52.5		150	46	39	242	31.8	12	40.8
Core Area / Element (mm^2)	**0.14[a] / 0.52 / 0.77[b]**	1.1[c]		2.09[c]	0.82	0.2	0.087	1.94	0.03	0.861
Process	**45nm CMOS SOI**	65nm CMOS		90nm SiGe	GaAs pHEMT	55nm CMOS	130nm SiGe BiCMOS	130nm SiGe BiCMOS	40nm CMOS	65nm CMOS

[a] Transformer-based IQ network. [b] With T/R switch. [c] Estimated value from the figure. [d] TX design.

CHAPTER 7. CONCLUSION

7.1 Research Summary

In this dissertation, we presented and discussed our innovative approaches towards the development of multiple new system architectures for various emerging applications at mm-wave, such as extreme mobile broadband data-rate link, energy efficient sensing, next-generation (5G/6G beyond) ultra-reliable low-latency network, augmented reality or virtual reality, massive machine-type or vehicle-to-vehicle communications as well as defense uses for fast-moving drone radar/sensing and emergency services. To support next-generation mm-Wave wireless systems with extreme mobile broadband data throughput, energy-efficient massive machine-type communication, and ultra-reliable low-latency network, we have presented several innovative system architectures to overcome many inherent challenges and achieve state-of-the-art performance for emerging wideband and low-latency applications.

In Chapter 2, we present an all-passive negative feedback network to serve as a broadband and wide FoV self-steering beam-former with zero DC power consumption for a phased-array receiver. A 4-element proof-of-concept design at 5GHz is demonstrated and achieves large array factor improvement over wide bandwidth and FoV even at μW-level RF inputs. In addition, it responds instantaneously to the input RF beam and operates continuously without any duty cycle operation and there is no need for energy storage element compared with energy harvesting based systems. Thus, the receiver can capture the incoming information with no down-time and the all-passive approach ensures no signal re-emission by the BF. The electromagnetically “quiet” nature is particularly useful

for many military and high-security applications. Most importantly, the proposed SSA BF forms a nonlinear negative feedback that can provide a large loop-gain even when receiving an end-fire signal (±90° incidence). This significantly expands the SSA FoV and cannot be realized using linear negative feedback loops. The nonlinear closed-loop exhibits DLL-like operation and this frequency agnostic nature ensures its broadband operation and utility in practical array applications. The proposed all-passive beamformer operates at zero DC power and outperforms reported state-of-the-art active designs.

Chapter 3 demonstrates a broadband scalable full-FoV self-steering array beamformer (SSA-BF) mm-Wave fiber-wireless integrated network over 25 km fiber link. The SSA-BF achieves calibration- and digital signal process (DSP)-free beamforming with passive delay-locked-loop (DLL) phase domain negative feedback loops to cover 2-GHz wide bandwidth and zero DC power consumption. Without any prior information (angle-of-arrival AoA), a proof-of-concept mm-Wave fiber-wireless SSA-BF demonstrates that it can rapidly yet accurately align the desired signals with low-latency beam-tracking and exhibits long-term system stability. It achieves 20 x100-MHz carrier aggregation of orthogonal frequency division multiplexing (OFDM) with aggregating 10Gb/s for future high-speed and dynamic 5G fiber-wireless networks. With the wideband antenna array, it is also the first fiber-wireless system that achieves autonomous beamforming on unknown angle of arrival signals, 64-QAM multi-Gb/s wideband modulated signal beamforming, extreme wide FoV coverage for radio over fiber, and fast response time < 3ms, supporting future emerging mm-Wave 5G mobile fronthaul application.

In Chapter 4, we present an 8-element MIMO receiver array that is the first of its kind to support hybrid BF: autonomous mm-Wave/RF front-end BF + digital baseband BF. The

hybrid BF MIMO receiver array includes an on-chip 2-stage closed-loop mm-wave/RF front-end beamformers and off-chip baseband digital BF. The 2-stage closed-loop mm-wave/RF front-end beamformers alone support a variety of operation modes: (mode-I) autonomous beam-forming/tracking for an unknown in-band desired signal, (mode-II) autonomous rejection of one unknown in-band/co-channel blocker + autonomous beam-forming/tracking for an unknown in-band desired signal, (mode III-A) autonomous rejection of one unknown in-band/co-channel blocker with one deep spatial notch (54dB rejection), and (mode III-B) autonomous rejection of two unknown in-band/co-channel blockers with two notches (30~40dB rejection). It is the first RX array that achieves (1) autonomous rejection of unknown blockers and beam-forming on unknown desired signals, (2) 64-/256-QAM co-channel blocker rejection and desired signal beam-forming, both with multi-Gb/s wideband modulation, and (3) fast response time < 1μs per SSA BF stage, supporting low-latency applications in the future complicated EM environment.

Next, Chapter 5 shows a wideband 27-41GHz RX array for N-input-N-output MIMO systems, which employs scalable cascadable array-based high-order Autonomous Spatial Filters (ASFs) as a “smart” spatial filter bank for instinctual multi-blocker/signal management to assist digital BF. Mm-Wave wideband LNAs and passive mixers provide broadband frontend spectral filtering. The ASFs operate at IF, and each ASF employs an array-based phase-domain negative feedback for auto-beam-tracking and a feedforward path for spatial filtering. Identical ASF stages are cascaded to sequentially suppress multiple unknown spatially blockers or equalize multiple signals. An example 4-element broadband mm-Wave RX array frontend includes passive mixer spectral filter and three cascaded IF ASFs, which is the first of its kind to employ N-Input-N-Output autonomous

frontend spatial filters using scalable cascadable ASFs. This is also the first MIMO system that realizes “Iterative Source Localization” algorithmic computation completely in the frontend RF/analog domain. The MIMO RX array achieves (1) autonomous rejection of multiple unknown blockers and/or beamforming on unknown desired signals, (2) rejection of co-channel blockers and enhancing signal SINR both at multi-Gb/s 64-/256-QAM modulations, and (3) ultra-fast response time of < few μs per ASF stage. The proposed MIMO RX array seeks to address complex EM environments and dynamic, low-latency, and high-reliability applications, such as 5G massive machine type communications, autonomous driving, and AR/VR.

The last part of this dissertation, Chapter 6, we introduces a mm-Wave RX array with calibration-free instantaneously broadband Multi-Gb/s 64-/256-QAM IR. Compared to recently reported 5G mm-Wave full RXs and I/Q LO generation/ I/Q Mixer, measurement results show that the proposed RX covers the widest mm-Wave frontend bandwidth 24.5-43.5GHz (LO generation is from 25-50GHz) and state-of-the-art 12Gb/s 64QAM and 8Gb/s 256QAM IR for multi-band 5G communication. The RX also achieves a compact size, low noise figure 3.2-6.1dB (5.3-7.4dB with T/R switch), and superior linearity -7/-25.5dB IP1dB at lowest/highest gain. Most importantly, with low-loss wideband transformer-based mm-Wave I/Q network, this is the first demonstration of instantaneously wideband GHz IR with no calibration, switching/tuning elements, or external controls, enabling instantaneously wideband low-latency 5G MIMOs in complex EM environments.

7.2 Research Publications

7.2.1 Journal Publications

[J-1] **M. Huang** and H. Wang, "A Mm-Wave Wideband MIMO RX with Instinctual Array-Based Blocker/Signal Management for Ultra-Low-Latency Communication," accepted and to appear in *IEEE J. of Solid-State Circuits*, 2019.

[J-2] S. Li, T. Chi, T. Huang, **M. Huang**, D. Jung, and H. Wang, "A Buffer-Less Wideband Frequency Doubler in 45nm CMOS-SOI with Transistor Multi-Port Waveform Shaping Achieving 25% Drain Efficiency and 46-89GHz Instantaneous Bandwidth," *IEEE Solid-State Circuits Lett.*, May, 2019

[J-2] **M. Huang**, T. Chi, F. Wang, T. Li, and H. Wang, "Hybrid Beamformer Array with Full-FoV Dynamic and Autonomous Unknown Blockers Rejection and Signals Tracking for Low-Latency 5G/Mm-Wave Communication," *IEEE Trans. Microw. Theory. Tech*, Apr. 2019. – **IEEE TMTT Special Issue on "5G Hardware and System Technologies".**

[J-3] T. Li, **M. Huang**, and H. Wang, "Millimeter-Wave Continuous-Mode Power Amplifier for 5G MIMO Applications," *IEEE Trans. Microw. Theory. Tech*, Apr. 2019. – **IEEE TMTT Special Issue on "5G Hardware and System Technologies"**

[J-5] **M. Huang**, T. Chi, F. Wang, and H. Wang, "An All-Passive Negative Feedback Network for Broadband and Wide Field-of-View Self-Steering Beam-Forming with Zero DC Power Consumption," *IEEE J. of Solid-State Circuits*, vol. 52, no. 5, pp. 1260 - 1273, May 2017. (invited)

[J-6] **M. Huang**, T. Chi, S. Li, T. Huang, and H. Wang, "A 24.5-43.5GHz Ultra-Compact CMOS Receiver Front-End with Calibration-Free Instantaneous Full-Band Image Rejection for Multiband 5G Massive MIMO," *IEEE J. of Solid-State Circuits*

[J-7] **M. Huang,** Y. Chen, P. Peng, H. Wang, and G.-K. Chang, "A Full Field-of-View Self-Steering Beamformer for 5G Mm-Wave Fiber-Wireless Mobile Fronthaul," *IEEE Journal of Lightwave Technology*

7.2.2 Conference Publications

[C-1] S. Li, **M. Huang**, D. Jung, T. Huang, and H. Wang, "A 28GHz Current-Mode Inverse-Outphasing Transmitter Achieving 40%/31% PA Efficiency at Psat/6dB PBO and Supporting 15Gbit/s 64QAM for 5G Communication," *accepted and to appear in IEEE International Solid-State Circuits Conference (ISSCC) Dig. Tech. Papers*, Feb. 2020.

[C-2] N. S. Mannem, **M. Huang**, T. Huang, S. Li, and H. Wang, "A Reconfigurable Series/Parallel Quadrature Coupler Doherty PA in CMOS-SOI with VSWR Resilient Linearity and Back-Off PAE for 5G MIMO Arrays," *accepted and to appear in IEEE International Solid-State Circuits Conference (ISSCC) Dig. Tech. Papers*, Feb. 2020.

[C-3] S. Li, T. Chi, D. Jung, T. Huang, **M. Huang**, and H. Wang, "An E-Band High-Linearity Antenna-LNA Frontend with 4.8dB NF and 2.2dBm IIP3 Exploiting Multi-Feed On-Antenna Noise-Canceling and Gm-Boosting," accepted and to appear in *IEEE International Solid-State Circuits Conference (ISSCC) Dig. Tech. Papers*, Feb. 2020.

[C-4] **M. Huang**, T. Chi, F. Wang, S. Li, T. Huang, and H. Wang, "A 24.5-43.5GHz Compact RX with Calibration-Free 32-56dB Full- Frequency Instantaneously Wideband Image Rejection Supporting Multi-Gb/s 64-QAM/256-QAM for Multi-Band 5G Massive MIMO" *Proc. IEEE Radio Frequency Integrated Circuits (RFIC),* June. 2019. — **2019 RFIC Best Student Paper Award Finalist**

[C-5] **M. Huang**, T. Huang, M. Swaminathan, and H. Wang, "Ultra-Compact Concurrent Multi-Directional Beamforming Receiving Network for High-Efficiency Wireless Power Transfer" *Proc. IEEE International Microwave Symposium (IMS)*, June. 2019.

[C-6] S.Lee, **M. Huang**, Y. Youn, and H. Wang, "A 15 – 55 GHz Low-Loss Ultra-Compact Folded Inductor-Based Multi-Section Wilkinson Power Divider for Multi-Band 5G Applications" *Proc. IEEE International Microwave Symposium (IMS)*, June. 2019.

[C-7] T. Yang, **M. Huang**, Y. Chen, P, Peng, H. Wang and G. Chang, "A 4-channel Beamformer for 9-Gb/s MMW 5G Fixed-wireless Access over 25-km SMF with Bit-loading OFDM," *Proc. Optical Fiber Communication Conference (OFC)*, March. 2019.

[C-8] **M. Huang** and H. Wang, "A 27-41GHz MIMO Receiver with N-Input-N-Output Using Scalable Cascadable Autonomous Array-Based High-Order Spatial Filters for Instinctual Full-FoV Multi-Blocker/Signal Management," *IEEE International Solid-State Circuits Conference (ISSCC) Dig. Tech. Papers*, Feb. 2019.

[C-9] E. Garay, **M. Huang**, and H. Wang, "A Cascaded Self-Similar Rat-Race Hybrid Coupler Architecture and its Compact Fully Integrated Ka-band Implementation," *Proc. IEEE International Microwave Symposium (IMS)*, Jun. 2018.

[C-10] **M. Huang** and H. Wang, "Scalable Wideband Hybrid Beam-Forming MIMO Receiver Array with Multi-Stage Closed-Loop Beam-Formers for Full-FoV Dynamic and Autonomous Unknown Blocker Rejection and Signal Tracking," *Proc. the Government Microcircuit Applications and Critical Technology Conference (GOMACTech)*, Mar. 2018.

[C-11] **M. Huang**, T. Chi, F. Wang, T. Li, and H. Wang, "A 23-30GHz Hybrid Beam-Forming MIMO Receiver Array with Closed-Loop Multi-Stage Front-End Beam-Formers for Full-FoV Dynamic and Autonomous Unknown Signal Tracking and Blocker

Rejection," *IEEE International Solid-State Circuits Conference (ISSCC) Dig. Tech. Papers*, Feb. 2018.

[C-12] T. Li, **M. Huang**, and H. Wang, "A Continuous-Mode Harmonically-Tuned 19-29.5GHz Ultra-Linear PA Supporting 18Gbit/s at 18.4% Modulation PAE and 43.5% Peak PAE," *IEEE International Solid-State Circuits Conference (ISSCC) Dig. Tech. Papers*, Feb. 2018.

[C-13] H. Wang, S. Hu, T. Chi, F. Wang, S. Li, **M. Huang**, and J. Park, "Towards Energy-Efficient 5G Mm-Wave Links: Exploiting Broadband Mm-Wave Doherty Power Amplifier and Multi-Feed Antenna with Direct On-Antenna Power Combining (Invited)," *Proc. IEEE Bipolar/BiCMOS Circuits and Technology Meeting (BCTM)*, Sep. 2017.

[C-14] T. Chi, H. Wang, **M. Huang**, F. Dai, and H. Wang, "A Bidirectional Lens-Free Digital-Bits-In/-Out 0.57mm2 Terahertz Nano-Radio in CMOS with 49.3mW Peak Power Consumption Supporting 50cm Internet-of-Things Communication," *Proc. IEEE Custom Integrated Circuits Conference (CICC)*, May 2017. — **2017 IEEE CICC Best Conference Paper Award (Top 1 paper among all the paper categories in CICC 2017)**

[C-15] T. Chi, **M. Huang**, S. Li, H. Wang, "A Packaged 90-to-300GHz Transmitter and 115-to-325GHz Coherent Receiver in CMOS for Full-Band Continuous-Wave Mm-Wave Hyperspectral Imaging," *IEEE International Solid-State Circuits Conference (ISSCC) Dig. Tech. Papers*, Feb. 2017.

[C-16] T. Chi, F. Wang, S. Li, **M. Huang**, J. Park, and H. Wang, "A 60GHz On-Chip Linear Radiator with Single-Element 27.9dBm Psat and 33.1dBm Peak EIRP Using Multi-

Feed Antenna for Direct On-Antenna Power Combining," *IEEE International Solid-State Circuits Conference (ISSCC) Dig. Tech. Papers*, Feb. 2017

[C-17] **M. Huang** and H. Wang, "An All-Passive Negative Feedback Network for Broadband and Full Field-of-View Self-Steering Beam-Forming with Zero DC Power Consumption," *Proc. the Government Microcircuit Applications and Critical Technology Conference (GOMACTech)*, Mar. 2017.

[C-18] E. Garay, **M. Huang**, and H. Wang, "A Cascaded Rat-Race Hybrid Coupler Architecture and its Compact Ka-band Implementation," *Proc. the Government Microcircuit Applications and Critical Technology Conference (GOMACTech)*, Mar. 2017.

[C-19] **M. Huang**, T. Chi, and H. Wang, "A 5GHz All-Passive Negative Feedback Network for RF Front-End Self-Steering Beam-Forming with Zero DC Power Consumption," *Proc. IEEE Radio Frequency Integrated Circuits (RFIC)*, May 2016. — **2016 RFIC Best Student Paper Award (2nd Place)**

[C-20] **M. Huang** and H. Wang, "An Ultra-Compact Folded Inductor Based Mm-Wave Rat-Race Coupler in CMOS," *Proc. IEEE International Microwave Symposium (IMS)*, May 2016.

[C-21] Y. Wang, E. Hardy, T. Chi, **M. Huang**, H. Wang, A. Brown, T. Barker, and W. A. Lam, "Electrical-Wound Dressing Demonstrates That Low-Voltages Augment Hemostasis and Clot Formation," *BMES Annual Meeting*, Oct. 2015.

7.2.3 Research Awards

[A-1] 2019 Marconi Society Paul Baran Young Scholar Award

— The Paul Baran Young Scholar Award recognizes young scientists and engineers who are under 28 years old and have demonstrated exceptional capabilities and potentials. The Young Scholars are selected worldwide with only 3 awardees in 2019. I am honored to be the first Georgia Tech Ph.D. student and the first Taiwanese to receive this prestigious award.

[A-2] 2019 IEEE Solid-State Circuits Society Predoctoral Achievement Award

[A-3] 2018 IEEE Microwave Theory and Techniques Society Graduate Fellowship

[A-4] 2017 IEEE Custom Integrated Circuits Conference (CICC) Best Conference Paper Award (co-recipient, 1st place)

[A-5] 2017 ISSCC Analog Devices Inc. Outstanding Student Designer Award

[A-6] 2017 Georgia Tech Power Deliver for Electronic Systems IAB Best Poster Awards (1st place)

[A-7] 2016 IEEE Radio Frequency Integrated Circuits (RFIC) Best Student Paper Award (2nd place)

[A-6] 2016 Georgia Tech Power Deliver for Electronic Systems IAB Best Poster Awards (1st place)

[A-8] 2015 Georgia Tech Power Delivery for Electronics Systems Best Poster Award

REFERENCES

[1] H. Wang, *et al.*, "A tunable concurrent 6-to-18GHz phased-array system in CMOS", in *Proc. IEEE International Microwave Symposium (IMS)*, pp. 387-390, June 2008.

[2] X. Guan, H. Hashemi, and A. Hajimiri, "A fully integrated 24-GHz eight-element phased-array receiver in silicon," *IEEE J. Solid-State Circuits*, vol. 39, no. 12, pp. 2311–2320, Dec. 2004.

[3] T. Yu, and G. M. Rebeiz, "22–24 GHz 4-element CMOS phased array with on-chip coupling characterization," *IEEE J. Solid-State Circuits*, vol. 43, no. 9, pp. 2134–2143, Sep. 2008.

[4] L. D. DiDomenico and G. M. Rebeiz, "Digital communications using self-phased arrays," IEEE Trans. Microw. Theory Tech., vol. 49, no. 4, pp. 677–684, Apr. 2001.

[5] G. Shiroma, R. Miyamoto, and W. Shiroma, "A full-duplex dual-frequency self-steering array using phase detection and phase shifting," *IEEE Trans. Microw. Theory Techn.*, vol. 54, no. 1, pp. 128–134, Jan. 2006.

[6] J. M. Akagi, A. Zamora, M. K. Watanabe, and W. A. Shiroma, "A self-steering array using power detection and phase shifting," in *Proc. IEEE International Microwave Symposium (IMS)*, pp. 1325–1328, June 2008.

[7] A. K. Gupta and J. F. Buckwalter, "A self-steering receiver array using jointly coupled oscillators and phased-locked loops," *IEEE Trans. Microw. Theory Techn.*, vol. 62, no. 3, pp. 631–644, Mar. 2014.

[8] L. Wu, A. Li, and H. C. Luong, "A 4-path 42.8-to-49.5 GHz LO generation with automatic phase tuning for 60 GHz phased-array receivers," *IEEE J. Solid-State Circuits*, vol. 48, no. 10, pp. 2309–2322, Oct. 2013.

[9] Y. T. Lo and J. F. Kiang, "Comparison of injection-locked and coupled oscillator arrays for beamforming," *IEEE Trans. Microw. Theory Techn.*, vol. 63, no. 4, pp. 1353-1360, Apr. 2015.

[10] S.-H. Yan and T.-H. Chu, "A beam-steering antenna array using injection locked coupled oscillators with self-tuning of oscillator free-running frequencies," *IEEE*

Trans. Antennas Propag., vol. 56, no. 9, pp. 2920–2928, Sep. 2008.

[11] M. Tabesh, *et. al*, A 65nm CMOS 4-Element Sub-34mW/Element 60GHz Phased-Array Transceiver, *in IEEE Int. Solid-State Circuits Conf. (ISSCC) Dig. Tech. Papers*, pp. 166-167, Feb. 2011.

[12] R. Miyamoto and T. Itoh, "Retrodirective arrays for wireless communications," *IEEE Microw. Mag.*, vol. 3, no. 1, pp. 71–79, Mar. 2002.

[13] S. Lim, K. M. K. H. Leong, and T. Itoh, "Adaptive power controllable retrodirective array system for wireless sensor server applications," *IEEE Trans. Microw. Theory Techn.*, vol. 53, no. 11, pp. 3735–3743, Dec. 2005.

[14] Y. Li and V. Jandhyala, "Design of retrodirective antenna arrays for short-range wireless power transmission," *IEEE Trans. Antennas Propag.*, vol. 60, no. 1, pp. 206–211, 2012.

[15] A. Massa, G. Oliveri, F. Viani, and P. Rocca, "Array designs for long-distance wireless power transmission: State-of-the-art and innovative solutions," *Proc. IEEE.*, vol. 101, no. 6, pp. 1464–1481, June 2013.

[16] M. Huang, T. Chi, and H. Wang, "A 5GHz all-passive negative feedback network for RF front-end self-steering beam-forming with zero DC power consumption," in *Proc. IEEE RF Integrated Circuits Symposium (RFIC),* May 2016.

[17] J. Rabaey *et. al*., "PicoRadios for wireless sensor networks: the next challenge in ultra-low-power design," in *IEEE Int. Solid-State Circuits Conf. (ISSCC) Dig. Tech. Papers*, pp. 200-201, July 2002.

[18] Y. Zhang *et. al*., "A batteryless 19 μW MICS/ISM-band energy harvesting body sensor node SoC for ExG applications," *IEEE J. Solid State Circuits*, vol. 48, no. 1, pp. 199–213, Jan. 2013.

[19] D. Yoon *et al.,* "A 5.5 nW 32.768 kHz DLL-assisted XO for real-time clocks in wireless sensing applications," in *IEEE Int. Solid-State Circuits Conf. (ISSCC) Dig. Tech. Papers*, pp. 366–367, Feb. 2012.

[20] R. E. Barnett, J. Liu, and S. Lazar, "A RF to DC voltage conversion model for multi-stage rectifiers in UHF RFID transponders," *IEEE J. Solid-State Circuits*, vol. 44, no.

2, pp. 354–370, Feb. 2009.

[21] M. Huang and H. Wang, "An ultra-compact folded inductor-based mm-Wave rat-race coupler in CMOS," *IEEE International Microwave Symposium (IMS)*, May 2016.

[22] M. Huang, T. Huang, M. Swaminathan, and H. Wang, "Ultra-compact concurrent multi-directional beamforming receiving network for full-FoV high-efficiency wireless power transfer," *IEEE International Microwave Symposium (IMS)*, June 2019.

[23] B. S. Leibowitz, B. E. Boser, and K. S. J. Pister, "A 256-element CMOS imaging receiver for free-space optical communication," *IEEE J. Solid-State Circuits*, vol. 40, no. 9, pp. 1948–1956, Sep. 2005.

[24] R. Ebelt *et. al.,* "Cooperative indoor localization using 24-GHz CMOS radar transceivers," *IEEE Trans. Microw. Theory Techn.*, vol. 62, no. 9, pp. 2193–2203, Sep. 2014.

[25] S. S. Ahmed, A. Schiessl, and L.-P. Schmidt, "A novel fully electronic active real-time imager based on a planar multistatic sparse array," *IEEE Trans. Microw. Theory Techn.*, vol. 59, no. 12, pp. 3567–3576, Dec. 2011.

[26] G. K. Chang, *et al.,* "Grand Challenges of Fiber Wireless Convergence for 5G Mobile Data Communications," *in Proc. Optoelectronics and Communications Conference (OECC)*, 2018.

[27] A. Ghosh, "5G New Radio (NR): physical layer overview and performance," *in IEEE Communication Theory Workshop,* May 2018, pp. 1–38.

[28] A.M. Trinidad, *et al.,* "Optical Beamformer for K-band Smart Antenna Systems," *in Proc. Optical Fiber Communication Conference,* 2018.

[29] H. Lu, *et al.,* "mmWave Beamforming using Photonic Signal Processing for Future 5G Mobile Systems," *in Proc. Optical Fiber Communication Conference (OFC),* 2018.

[30] K.Furuya, *et al.,* "60 GHz-Band Photonic-Integrated Array-Antenna and Module for Radio-over-Fiber-Based Beam Forming," *IEICE Trans. Commun.*, vol. E100-B, no. 10, pp. 1717-1725, 2017.

[31] N.M. Tessema and A. M. J. Koonen, *et al.,* "A Photonic-Assisted Beamformer for K-band RF Antenna Arrays," in *Proc. International Topical Meeting on Microwave Photonics (MWP),* 2017.

[32] Chris G. H. Roeloffzen, *et al.,* "Integrated Optical Beamformers," *in Proc. Optical Fiber Communication Conference (OFC),* 2015.

[33] G.-K. Chang and Y.-W. Chen, "Key Fiber Wireless Integrated Radio Access Technologies for 5G and Beyond," *in Proc. Optoelectronics and Communications Conference (OECC),* 2019.

[34] T. Mengual, *et al.,* "Optical Beamforming Network with Multibeam Capability based on a Spatial Light Modulator," *in Proc. Optical Fiber Communication Conference (OFC),* 2008.

[35] G.-K. Chang and P.-C. Peng, "Grand challenges of fiber wireless convergence for 5G mobile data communications," *in Proc. Optoelectronics and Communications Conference (OECC),* 2018.

[36] M. M. Sisto, *et al.,* "Optical Phase and Amplitude Control for Beamforming with Cascades of Gires-Tournois Bragg Grating Filters," *in Proc. Optical Fiber Communication Conference (OFC),* 2010.

[37] Vanessa C. Duarte, *et al.,* "Integrated Photonic True-Time Delay Beamformer for a Ka-band Phased Array Antenna Receiver," *in Proc. Optical Fiber Communication Conference (OFC),* 2018.

[38] W. Roh, *et al.,* "Millimeter-Wave beamforming as an enabling technology for 5G cellular communications: theoretical feasibility and prototype results," *IEEE Commun. Mag.,* vol. 52, no. 2, pp. 106–113, Feb. 2014.

[39] B. Sadhu, *et al.,* "A 28-GHz 32-element TRX phased-array IC with concurrent dual-polarized operation and orthogonal phase and gain control for 5G communications," *IEEE J. of Solid-State Circuits,* vol. 52, no. 12, pp. 3373–3391, Dec 2017.

[40] M. Huang, T. Chi, F. Wang, T. Li, and H. Wang, "A 23-30GHz hybrid beam-forming MIMO receiver array with closed-loop multi-stage front-end beam-formers for full-FoV dynamic and autonomous unknown signal tracking and blocker rejection," *IEEE International Solid-State Circuits Conference (ISSCC),* pp. 68-70, Feb. 2018.

[41] H.-T. Kim *et al.,* "A 28-GHz CMOS direct conversion transceiver with packaged 2 × 4 antenna array for 5G cellular system," *IEEE J. Solid– State Circuits, vol. 53, no. 5,* pp. 1245–1259, May 2018.

[42] J. Pang, *et al.,* "A 28GHz CMOS phased-array beamformer utilizing neutralized bi-directional technique supporting dual-polarized MIMO for 5G NR," *IEEE International Solid-State Circuits Conference (ISSCC),* pp. 344-346, Feb. 2019.

[43] T. Chi, *et al.,* "A 60GHz on-chip linear radiator with single-element 27.9 dBm Psat and 33.1dBm peak EIRP using multifeed antenna for direct on-antenna power combining," *IEEE International Solid-State Circuits Conference (ISSCC),* pp. 296-297, Feb. 2017.

[44] K. Dasgupta, *et al.,* "A 60-GHz Transceiver and Baseband with Polarization MIMO in 28-nm CMOS," *IEEE J. of Solid-State Circuits,* vol. 53, no. 12, pp. 3613 - 3627, Dec. 2018.

[45] B.Rupakula and Gabriel M. Rebeiz, "Third-Order Intermodulation Effects and System Sensitivity Degradation in Receive-Mode 5G Phased Arrays in the Presence of Multiple Interferers", *IEEE Trans. Microw. Theory Techn.,* vol. 66, no. 12, pp. 5780-5795, 2018.

[46] T. Li, M. Huang, H. Wang., "A continuous-mode harmonically tuned 19- to-29.5GHz ultra-linear PA supporting 18Gb/s at 18.4% modulation PAE and 43.5% peak PAE," *IEEE International Solid-State Circuits Conference (ISSCC),* pp. 410-412, Feb. 2018.

[47] J. D. Dunworth, *et al.,* "A 28 GHz bulk-CMOS dual-polarization phased array transceiver with 24 channels for 5G user and basestation equipment," *IEEE International Solid-State Circuits Conference (ISSCC),* pp. 70–72, Feb. 2018.

[48] M. Huang, T. Chi, F. Wang, T. Li, and H. Wang, "A full-FoV autonomous hybrid beamformer array with unknown blockers rejection and signals tracking for low-latency 5G mm-Wave links," *IEEE Trans. Microw. Theory Techn.,* Apr. 2019.

[49] S. Mondal and J. Paramesh, "A Reconfigurable 28-/37-GHz MMSE-adaptive hybrid-beamforming receiver for carrier aggregation and multi-standard MIMO communication," *IEEE J. Solid–State Circuits,* vol. 54, no. 5, pp. 1391–1406, Jan. 2019.

[50] K. Kibaroglu, M. Sayginer, and G. M. Rebeiz, "A low-cost scalable 32- element 28-

GHz phased array transceiver for 5G communication links based on a 2 × 2 beamformer flip-chip unit cell," *IEEE J. Solid–State Circuits*, vol. 53, no. 5, pp. 1260–1274, May 2018.

[51] H. Wang, *et al.,* "Towards Energy-Efficient 5G Mm-Wave Links: Exploiting Broadband Mm-Wave Doherty Power Amplifier and Multi-Feed Antenna with Direct On-Antenna Power Combining," *Proc. IEEE Bipolar/BiCMOS Circuits and Technology Meeting*, Sep. 2017.

[52] J. Pang, *et al.,* "A 28-GHz CMOS phased-array transceiver based on LO phase-shifting architecture with gain invariant phase tuning for 5G new radio," *IEEE J. Solid–State Circuits*, vol. 54, no. 5, pp. 1228–1242, Mar. 2019.

[53] S. Li, *et al.,* "A Buffer-Less Wideband Frequency Doubler in 45nm CMOS-SOI with Transistor Multi-Port Waveform Shaping Achieving 25% Drain Efficiency and 46-89GHz Instantaneous Bandwidth," *IEEE Solid-State Circuits Lett.*, vol. 2, no. 4, pp. 25 - 28, Apr. 2019.

[54] M. Huang, *et al.,* "A 24.5-43.5GHz Compact RX with Calibration-Free 32-56dB Full-Frequency Instantaneously Wideband Image Rejection Supporting Multi-Gb/s 64-QAM/256-QAM for Multi-Band 5G Massive MIMO," *IEEE RF Integrated Circuits Symposium (RFIC)*, June. 2019.

[55] U. Kodak and G. M. Rebeiz, "A 5G 28-GHz Common-Leg T/R Front-End in 45-nm CMOS SOI with 3.7-dB NF and− 30-dBc EVM with 64-QAM/500-MBaud Modulation," *IEEE Trans. Microw. Theory Techn.*, vol. 67, no. 1, pp. 318-331, Oct. 2018.

[56] M. Huang, *et al.,* "A 24.5-43.5GHz Ultra-Compact CMOS Receiver Front-End with Calibration-Free Instantaneous Full-Band Image Rejection for Multiband 5G Massive MIMO," *IEEE J. Solid–State Circuits*, 2020.

[57] Yu Tang, *et al.,* "A 4-channel beamformer for 9-Gb/s MMW 5G fixed wireless access over 25-km SMF with bit-loading OFDM," *IEEE Optical Fiber Communication Conference (OFC)*, Mar. 2019.

[58] M. Huang, *et al.,* "A Full Field-of-View Self-Steering Beamformer for 5G Mm-Wave Fiber-Wireless Mobile Fronthaul," *IEEE Journal of Lightwave Technology (JLT)*, 2020.

[59] T. Li, M. Huang, H. Wang., “Millimeter-Wave Continuous-Mode Power Amplifier for 5G MIMO Applications,” *IEEE Trans. Microw. Theory Techn.*, Apr. 2019.

[60] Y. Wang, *et al.*, “A 60-GHz 3.0-Gb/s Spectrum Efficient BPOOK Transceiver for Low-Power Short-Range Wireless in 65-nm CMOS,” *IEEE J. Solid-State Circuits*, vol. 54, no. 5, pp. 1363-1374, Jan. 2019.

[61] F. Wang, T. Li, and H. Wang, "A Highly Linear Super-Resolution Mixed-Signal Doherty Power Amplifier for High-Efficiency Multi-Gbit/s Mm-Wave 5G Communication," *IEEE International Solid-State Circuits Conference (ISSCC)*, pp. 88-90, Feb. 2019.

[62] S. Mondal, R. Singh, and J. Paramesh, “A reconfigurable bidirectional 28/37/39GHz front-end supporting MIMO-TDD, carrier aggregation TDD and FDD/full-duplex with self-interference cancellation in digital and fully connected hybrid beamformers,” *IEEE International Solid-State Circuits Conference (ISSCC)*, pp. 346-348, Feb. 2019.

[63] T. Chi, M. Huang, S. Li, H. Wang, “A packaged 90-to-300GHz transmitter and 115-to-325GHz coherent receiver in CMOS for full-band continuous-wave mm-wave hyperspectral imaging,” *IEEE International Solid-State Circuits Conference (ISSCC)*, pp. 304–305, Feb. 2017.

[64] M. Huang and H. Wang, “A 27-41GHz MIMO Receiver with N-Input-N-Output Using Scalable Cascadable Autonomous Array-Based High-Order Spatial Filters for Instinctual Full-FoV Multi-Blocker/Signal Management,” *IEEE International Solid-State Circuits Conference (ISSCC)*, pp. 346-348, Feb. 2019.

[65] S. Han, C.-L. I, Z. Xu, and C. Rowell, “Large-scale antenna systems with hybrid analog and digital beamforming for millimeter wave 5G”, *IEEE Commun. Mag.*, vol. 53, no. 1, pp. 186–194, Jan. 2015.

[66] M. Huang and H. Wang, “A Mm-Wave Wideband MIMO RX with Instinctual Array-Based Blocker/Signal Management for Ultra-Low-Latency Communication,” *IEEE J. Solid-State Circuits*, 2019.

[67] M. Huang, T. Chi, F. Wang, and H. Wang, “An all-passive negative feedback network for broadband and wide field-of-view self-steering beam-forming with Zero DC power consumption,” *IEEE J. of Solid-State Circuits*, vol. 52, no. 5, pp. 1260 - 1273, May 2017.

[68] S. Lee, M. Huang, Y. Youn, and H. Wang, “A 15 – 55 GHz low-loss ultra-compact folded inductor-based multi-section wilkinson power divider for multi-band 5G applications,” *IEEE International Microwave Symposium (IMS)*, June 2019.

[69] E. Garay, M. Huang, H. Wang, "A cascaded self-similar rat-race hybrid coupler architecture and its compact fully integrated Ka-band implementation," *IEEE International Microwave Symposium*, Jun. 2018.

[70] Y.-W. Chen, *et al.*, “RF power fading mitigation for an IMDD multicarrier LR-PON,” *Opt. Express*, vol. 24, no. 14, pp. 19311-19321, 2016.

[71] Y.-W. Chen, *et al.*, “A Reliable OFDM based MMW Mobile Fronthaul with DSP-aided Sub-band Spreading and Time-Confined Windowing,” Journal of Lightwave Technology, vol. 37, pp. 3236-3243, 2019.

[72] V. Venkateswaran, F. Pivit, and L. Guan, “Hybrid RF and digital beamformer for cellular networks: Algorithms, microwave architectures, and measurements,” *IEEE Trans. Microw. Theory Techn.*, vol. 64, pp. 2226–2243, Jul. 2016.

[73] M. Harter, J. Hildebrandt, A. Zirof, and T. Zwick, “Self-calibration of a 3-D-digital beamforming radar system for automotive applications with installation behind automotive covers,” *IEEE Trans. Microw. Theory Techn.*, vol. 64, no. 9, pp. 2994–3000, Sep. 2016.

[74] L. Zhang and H. Krishnaswamy, “Arbitrary analog/RF spatial filtering for digital MIMO receiver arrays,” *IEEE J. of Solid-State Circuits*, pp. 3392-3404, Dec. 2017.

[75] S. Jain, Y. Wang, and A. Natarajan, “A 10GHz CMOS RX frontend with spatial cancellation of co-channel interferers for MIMO/digital beamforming arrays,” *IEEE RF Integrated Circuits Symposium (RFIC)*, pp. 99-102, May 2016.

[76] A. Agrawal and A. Natarajan, “A concurrent dual-frequency/angle-of-incidence spatio-spectral notch filter using walsh function passive sequence mixers,” *IEEE International Microwave Symposium (IMS)*, June 2017.

[77] J. Park and H. Wang, “A transformer-based poly-phase network for ultra-broadband quadrature signal generation,” *IEEE Trans. Microw. Theory. Tech*, vol. 63, no. 12, pp. 4444 - 4457, Dec. 2015.

[78] H. Nosaka, *et al.*, "Vector modulator-based PS with 810° control range for 43-Gbps optical transceivers," *IEEE European Microwave Conference*, Oct. 2009.

[79] H. Wang and A. Hajimiri, "A wideband CMOS linear digital phase rotator," *IEEE Custom Integrated Circuits Conference (CICC)*, pp. 671–674, 2007.

[80] T. Li., J. Park, and H. Wang, "A 2-24GHz 360-degree full-span differential vector modulator phase rotator with transformer-based poly-phase quadrature network," *IEEE Custom Integrated Circuits Conference (CICC)*, 2015.

[81] J.C. Chen, K. Yao, and R.E. Hudson, "Source localization and beamforming," *IEEE Signal Processing Magazine*, vol. 19, no. 2, pp. 30-39, Aug. 2002.

[82] E. Masazade, R. Niu, P. K. Varshney, and M. Keskinoz, "Energy Aware Iterative Source Localization for Wireless Sensor Networks," *IEEE Trans. Signal Processing*, June 2010.

[83] W. Mantzel, J. Romberg and K. Sabra, "Round-robin multiple source localization," *IEEE J. Acoust. Soc. Am.*, Jan. 2014.

[84] I. F. Akyildiz, W. Su, Y. Sankarasubramaniam, and E. Cayirci, "A survey on sensor networks," *IEEE Commun. Mag.*, vol. 40, no. 8, pp. 102–114, Aug. 2002.

[85] A. Vempaty, T. Lang, and P. Varshney, "Distributed inference with byzantine data: state-of-the-art review on data falsification attacks," *IEEE Signal Processing Magazine*, Vol. 30, Issue 5, pp.65-75, 2013.

[86] E. Masazade, R. Niu, and P. K. Varshney, "Dynamic bit allocation for object tracking in wireless sensor networks," *IEEE Trans. Signal Processing*, vol. 60, no. 10, pp. 5048–5063, Oct. 2012.

[87] A. Vempaty, O. Ozdemir, and K. Agrawal, *et al.*, "Localization in wireless sensor networks: Byzantines and mitigation techniques", *IEEE Trans. Signal Processing*, vol. 61, no. 6, pp. 1495–1508, Mar. 2013.

[88] S. Liu, M. Fardad, E. Masazade, and P. K. Varshney, "Optimal Periodic Sensor Scheduling in Networks of Dynamical Systems", *IEEE Trans. Signal Processing*, vol. 62, no. 12, pp. 3055–3068, Apr. 2014.

[89] I. Nevat, G. W. Peters, and I. B. Collings, “Random Field Reconstruction With Quantization in Wireless Sensor Networks”, *IEEE Trans. Signal Processing*, vol. 61, no. 23, pp. 6020 - 6033, Sep. 2013.

[90] N. Cao, S. Choi, E. Masazade, and P. K. Varshney “Sensor Selection for Target Tracking in Wireless Sensor Networks with Uncertainty”, *IEEE Trans. Signal Processing*, vol. 64, no. 20, pp. 5191 - 5204, Jul. 2016.

[91] I. Nevat, G. W. Peters, F. Septier, and T. Matsui, “Estimation of Spatially Correlated Random Fields in Heterogeneous Wireless Sensor Networks”, *IEEE Trans. Signal Processing*, vol. 63, no. 10, pp. 2597 - 2609, Mar. 2015.

[92] N. Cao, S. Brahma, and P. K. Varshney, “Target Tracking via Crowdsourcing: A Mechanism Design Approach”, *IEEE Trans. Signal Processing*, vol. 63, no. 6, pp. 1464 - 1476, Jan. 2015.

[93] A. E. Assaf, S. Zaidi, S. Affes, and N. Kandil, “Low-Cost Localization for Multihop Heterogeneous Wireless Sensor Networks”, *IEEE Transactions on Wireless Communications*, vol. 15, no. 1, pp. 472 - 484, Sep. 2016.

[94] J. Chen, W. Dai, Y. Shen, V. K. N. Lau, and M. Z. Win, “Power Management for Cooperative Localization: A Game Theoretical Approach”, *IEEE Trans. Signal Processing*, vol. 64, no. 24, pp. 6517 - 6532, Aug. 2016.

[95] L. Lu, H. Zhang, and H.-C. Wu, “Novel Energy-Based Localization Technique for Multiple Sources”, *IEEE Systems Journal*, vol. 8, no. 1, pp. 142 - 150, June 2013.

[96] X. Yang, R. Niu, E. Masazade, and P. K. Varshney, “Novel Energy-Based Localization Technique for Multiple Sources”, *IEEE Systems Journal*, vol. 8, no. 1, pp. 142 - 150, June 2013.

[97] G. Wang and K. C. Ho, “Convex Relaxation Methods for Unified Near-Field and Far-Field TDOA-Based Localization”, *IEEE Transactions on Wireless Communications*, vol. 18, no. 4, pp. 2346 - 2360, Mar. 2019.

[98] S. Zaidi, A. E. Assaf, S. Affes, and N. Kandil, “Accurate Range-Free Localization in Multi-Hop Wireless Sensor Networks”, *IEEE Transactions on Communications*, vol. 64, no. 9, pp. 3886 - 3900, Jul. 2016.

[99] Y. Wang and K. C. Ho, "Unified Near-Field and Far-Field Localization for AOA and Hybrid AOA-TDOA Positionings", *IEEE Transactions on Wireless Communications*, vol. 17, no. 2, pp. 1242 - 1254, Dec. 2017.

[100] N. Iliev and I. Paprotny, "Review and Comparison of Spatial Localization Methods for Low-Power Wireless Sensor Networks", *IEEE Sensors Journal*, vol. 15, no. 10, pp. 5971 - 5987, June 2015.

[101] S. G. Mallat and Z. Zhang, "Matching Pursuits with Time-Frequency Dictionaries," *IEEE Trans. Signal Processing*, Dec. 1993.

[102] L. Zhou, C. Wang, Z. Chen, and P. Heydari, "A W-band CMOS receiver chipset for millimeter-wave radiometer systems," *IEEE J. of Solid-State Circuits*, vol. 46, no. 2, pp. 378 - 391, Feb. 2011.

[103] N. Ebrahimi and J. F. Buckwalter, "A High-Fractional-Bandwidth, Millimeter-Wave Bidirectional Image-Selection Architecture with Narrowband LO Tuning Requirements," *IEEE J. Solid–State Circuits*, vol. 53, no. 8, pp. 2164–2176, Aug 2018.

[104] J. -Y. Hsieh, T. Wang, and S. S. Lu, "A 90-nm CMOS V-band lowpower image-reject receiver front-end with high-speed auto-wake-up and gain controls," *IEEE Trans. Microw. Theory Techn.*, vol. 64, no. 2, pp. 541–549, Jan. 2016.

[105] W.-H. Lin, H.-Y. Yang, J.-H. Tsai, T.-W. Huang, H. Wang, "1024-QAM high image rejection E -band sub-harmonic IQ modulator and transmitter in 65-nm CMOS Process," *IEEE Trans. Microw. Theory Techn.*, vol. 61, no. 11, pp. 3974-3985, Nov. 2013.

[106] M. Frounchi, A. Alizadeh, C. T. Coen, and J. D. Cressler, "A low-loss broadband quadrature signal generation network for high image rejection at millimeter-wave frequencies," *IEEE Trans. Microw. Theory Techn.*, vol. 66, no. 12, pp. 5336–5346, Dec. 2018.

[107] F. Piri, M. Bassi, N. R. Lacaita, A. Mazzanti, and F. Svelto, "A PVT-Tolerant >40-dB IRR, 44% Fractional-Bandwidth Ultra-Wideband mm-Wave Quadrature LO Generator for 5G Networks in 55-nm CMOS," *IEEE J. Solid–State Circuits*, vol. 53, no. 12, pp. 3576 - 3586, Dec 2018.

[108] B. Welp, A. Meusling, K. Aufinger, and N. Pohl, "A Mixed-Mode Beamforming Radar Transmitter MMIC Utilizing Novel Ultrawideband IQ-Generation Techniques

in SiGe BiCMOS *IEEE Trans. Microw. Theory Techn.*, vol. 66, no. 6, pp. 2604–2617, Jun. 2018.

[109] D. Zhao and P. Reynaert, “A 40 nm CMOS E-band transmitter with compact and symmetrical layout floor-plans,” *IEEE J. Solid–State Circuits*, vol. 50, no. 11, pp. 2560–2571, Nov. 2015.

[110] Q. Ma, H. Chung, and G. M. Rebeiz, “A 35–105 GHz High Image-Rejection-Ratio IQ Receiver with Integrated LO Doubler and > 40 dB IRR”, in *Proc. IEEE International Microwave Symposium (IMS)*, June 2018.

[111] J. Pang, et al., “A 28-GHz CMOS phased-array transceiver based on LO phase-shifting architecture with gain invariant phase tuning for 5G new radio,” *IEEE J. Solid–State Circuits*, vol. 54, no. 5, pp. 1228–1242, Mar. 2019.

[112] B. Razavi, RF Microelectronics, 2nd ed. Upper Saddle River, NJ, USA: Prentice-Hall, 2012.

[113] S. Li, M. Huang, D. Jung, T. Huang, and H. Wang, "A 28GHz Current-Mode Inverse-Outphasing Transmitter Achieving 40%/31% PA Efficiency at Psat/6dB PBO and Supporting 15Gbit/s 64QAM for 5G Communication," *accepted and to appear in IEEE International Solid-State Circuits Conference (ISSCC) Dig. Tech. Papers*, Feb. 2020.

[114] N. S. Mannem, M. Huang, T. Huang, S. Li, and H. Wang, "A Reconfigurable Series/Parallel Quadrature Coupler Doherty PA in CMOS-SOI with VSWR Resilient Linearity and Back-Off PAE for 5G MIMO Arrays," *accepted and to appear in IEEE International Solid-State Circuits Conference (ISSCC) Dig. Tech. Papers*, Feb. 2020.

[115] S. Li, T. Chi, D. Jung, T. Huang, M. Huang, and H. Wang, "An E-Band High-Linearity Antenna-LNA Frontend with 4.8dB NF and 2.2dBm IIP3 Exploiting Multi-Feed On-Antenna Noise-Canceling and Gm-Boosting," accepted and to appear in *IEEE International Solid-State Circuits Conference (ISSCC) Dig. Tech. Papers*, Feb. 2020.